The Study on Hybrid Multi-Infeed HVDC System Connecting with Offshore Wind Farm

Liu, Yan

Publication date:
2013

Document Version
Publisher's PDF, also known as Version of record

DEPARTMENT OF ENERGY TECHNOLOGY
AALBORG UNIVERSITY

The study on Hybrid Multi-Infeed HVDC System Connecting with Offshore Wind Farm

YAN LIU

The study on Hybrid Multi-Infeed HVDC System Connecting with Offshore Wind Farm

by

Yan Liu

Dissertation submitted to the Faculty of Engineering and Science at Aalborg University

in partial fulfillment of the requirements for the degree of

Doctor of Philosophy in Energy Technology

DEPARTMENT OF ENERGY TECHNOLOGY
AALBORG UNIVERSITY
AALBORG, DENMARK
FEBRUARY 2013

The study on hybrid multi-infeed HVDC system connecting with offshore wind farm

Printed in Denmark by Uniprint

February 2013
ISBN: 978-87-92846-30-3

AALBORG UNIVERSITY
Department of Energy Technology
Pontoppidanstraede 101
DK-9220 Aalborg East
Denmark

Telephone: 0045 2136 9642
Fax: 0045 9815 1411
Web address: http://www.et.aau.dk

The study on Hybrid Multi-Infeed HVDC System Connecting with Offshore Wind Farm

PhD Student: Yan Liu

Supervisors: Prof. Zhe Chen

Publication List

[1] Y. Liu and Z. Chen, "Stability analysis of multi-infeed HVDC system applying VSC-HVDC," in Proc. of IEEE PES General Meeting 2010, pp. 1-7.

[2] Y. Liu and Z. Chen, "Transient Voltage Stability Analysis and Improvement of A Network with different HVDC Systems," in Proc. of IEEE PES General Meeting 2011, pp. 1-8.

[3] Y. Liu and Z. Chen, "Short Circuit Ratio analysis of multi-infeed HVDC system with a VSC-HVDC link," in Proc. of IEEE IECON 2011- 37th Annual Conference on IEEE Industrial Electronics Society, pp. 949-954.

[4] Y. Liu and Z. Chen, "Power Control Method on VSC-HVDC in a Hybrid Multi-infeed HVDC system," in Proc. of IEEE PES General Meeting 2012, pp. 1-8.

[5] Y. Liu, X. Wang and Z. Chen, "Cooperative Control of VSC-HVDC Connected Offshore Wind Farm with Low-Voltage Ride-Through Capability," in Proc. of IEEE POWERCON 2012, pp. 1-8.

[6] Y. Liu and Z. Chen, "Voltage Sensitivity Based Reactive Power Control on VSC-HVDC in A Wind Farm Connected Hybrid Multi-Infeed HVDC System," in Proc. of IEEE POWERTECH 2013, in review.

[7] Y. Liu and Z. Chen, "A Flexible Power Control Method of VSC-HVDC Link for the Enhancement of Effective Short-Circuit Ratio in a Hybrid Multi-Infeed HVDC System," IEEE Trans. Power System, accepted for publication.

This present report combined with the above listed scientific papers has been submitted for assessment in partial fulfilment of the PhD degree. The scientific papers are not included in this version due to copyright issues. Detailed publication information is provided above and the interested reader is referred to the original published papers. As part of the assessment, co-author statements have been made available to the assessment committee and are also available at the Faculty of Engineering and Science, Aalborg University.

Preface

This thesis is submitted to the Institute of Energy Technology, Aalborg University, Denmark in partial fulfillment of the requirements for Doctor of Philosophy in Electrical Engineering. The research has been supported in part by the Department of Energy Technology, Aalborg University and the China Scholarship Council (CSC).

The Ph.D. project has been supervised by Professor Zhe Chen from Institute of Energy Technology at Aalborg University. I would like to express my sincere gratitude to Prof. Chen for his professional support, guidance and encouragement during the entire project period.

Acknowledgments are also given to the Department of Energy Technology, Aalborg University and China Scholarship Council for their financially support to the project.

I would like to thank to all my colleagues from the Institute of Energy Technology in Aalborg University for their consistent help and support. Especially, I want to thank Dr. Sanjay Chaudhary for supplying me many useful materials about my research and for the discussions about the software adopted in my project. Also I want to express my thanks to all of my fellows in the research group led by Professor Chen for their friendship and encouragement.

Thanks also to all the visiting guests in Aalborg University during my research period, especially Professor Haishun Sun from Huazhong University of Science and Technology, China, for supporting me with his professional knowledge and patient guidance.

Last but not the least, I would like to express my profound thanks to my parents in China for their deep, penetrating love, affective warmth and understanding. And many thanks to my beloved husband, Xiongfei Wang, for his continuous encouragement and detailed technical support on my project.

Yan Liu
February, 2013
Aalborg

Abstract

Over the last decade, the High Voltage Direct Current (HVDC) technology has been widely applied for the long-distance, bulk power delivery in modern power systems. With the increasing use of Line-Commutated Converter based HVDC (LCC-HVDC) links, two or more HVDC links tend to feed into an AC system with the short electrical distance. And consequently, a so-called Multi-Infeed Direct Current (MIDC) transmission system is formed. On the other hand, as the fast growing of wind power in electrical grids, the Voltage Source Converter based HVDC (VSC-HVDC) links have becoming a favorable choice for connecting the large offshore wind farms, thanks to their flexibility on controlling active and reactive power. Hence, together with the existing LCC-HVDC links, a new power system structure, also named as the Hybrid Multi-Infeed HVDC system, can be envisioned, where both the LCC- and VSC-HVDC links terminate into the same AC grid.

In contrast to the traditional MIDC systems with only LCC-HVDC links, the flexible power control of VSC-HVDC links bring more possibilities for the stability enhancement of the HMIDC system. Accordingly, there is a need to explore the operation and control aspects of the HMIDC system. Hence, this thesis aims to develop advanced control strategies for the HMIDC system connecting with an offshore wind farm, in order to achieve the maximum use of VSC-HVDC link for enhancing the AC system stability.

In light of the main objective, two research tasks are divided in this project: 1) Modeling the HMIDC system connecting with an offshore wind farm, and investigating the main factors that affect the system stability under the different disturbances. 2) On the basis of the stability analysis, developing the appropriate control strategies for the studied HMIDC system in order to enhance the stability and power quality of the system.

The research work starts with establishing a basic HMIDC system model based on the power system of western Denmark, where the LCC-HVDC link and the VSC-HVDC link feed into one AC grid via two buses, respectively, and are interconnected through a tie-line. Under the built HMIDC system model, the influences of system parameters and the power control methods of the VSC-HVDC link on the system voltage stability are evaluated. In light of this, a new calculation method for the Effective Short Circuit Ratio (ESCR) is formulated for the HMIDC system, which provides a

quantitative tool for assessing the contributions of the system parameters and the VSC-HVDC link to the system voltage stability.

From the ESCR analysis, it is found that the power control strategies of the VSC-HVDC have an important effect on the system voltage stability. Hence, a flexible power control method of the VSC-HVDC link is proposed. The approach employs an adaptive current limiter to dynamically adjust the active current reference based on the output of the AC voltage controller, such that the maximum use of reactive power support capability of the VSC-HVDC link can be achieved.

Following the stability analysis of the basic HMIDC system, the research work moves forward to the control of the HMIDC system comprising the offshore wind farm at the sending end of the VSC-HVDC link. In this case, the Low Voltage Ride Through (LVRT) ability of the VSC-HVDC connected wind farm is one of the most important operation requirement. It is demanded that the wind turbines remain connected and actively contribute to the system stability during and after the onshore grid fault, otherwise the loss of the large power transmission will result in serious stability problem. To meet this requirement, a cooperative control of the VSC-HVDC system and a variable speed Squirrel Cage Induction Generator (SCIG)-based offshore wind farm is proposed. In the approach, an active power-frequency droop control is developed to achieve an autonomous reduction of the generated active powers from wind turbines, which thus furnish the VSC-HVDC connected wind farm with a fast and reliable LVRT ability.

The voltage fluctuation caused by the intermittent wind power is another important challenge to the system stability. As in the case of the LCC-HVDC links, their stable operations are highly dependent on the AC side voltage, and thus any voltage fluctuation at the infeed bus of the LCC-HVDC link may cause voltage instability of the HMIDC system. To address such a challenge, a voltage sensitivity-based reactive power control scheme for the VSC-HVDC link is developed, where a reactive power increment derived from the sensitivity factors is introduced into the power control loop in order to regulate the voltage of the target bus in the HMIDC system.

In this thesis, the HMIDC system models are built in the EMTDC/PSCAD environment. All of the proposed control strategies are evaluated via a series of simulation case studies. Simulation results have shown that the HMIDC system stability can be effectively improved by the proposed approaches.

Table of Contents

Chapter 1

Introduction

1.1 Background and Motivation

1.1.1 Hybrid Multi-Infeed HVDC (HMIDC) system

The High Voltage Direct Current (HVDC) technology has been widely applied for long-distance, bulk power delivery in modern power systems throughout the world. From 1970 when the silicon semi-conductor thyristor first came into use in HVDC applications [1], the HVDC technology has been developed rapidly in the last half-century. Compare to the traditional AC transmission, the HVDC systems are often preferred for the long distance, large amount power delivery. There are many reasons to apply HVDC links for the power transmission:

- **Lower Transmission loss:** under the same power rating, the power loss of DC line is much lower than the corresponding AC transmission lines, which was the original motivation of the DC technology development.
- **Lower cost of the transmission line:** The cost of power lines is much lower for DC links than AC lines when transmitting comparable amount of power, for example, the single polar HVDC system requires only one power line whereas three power lines are needed for the AC transmission. The total costs of the HVDC link and the AC transmission are shown in Fig.1.1.
- **Asynchronous interconnections:** The DC link decoupled the two AC systems connected at the two terminals of the DC link, which means the two grids are not synchronous. In that way the disturbance on frequency of one power system will not directly influence to the grid at the other side of the HVDC link.
- **The power carrying capability:** The power transfer in AC lines is dependent on the angle difference between the voltage phasors at the two ends. The maximum power

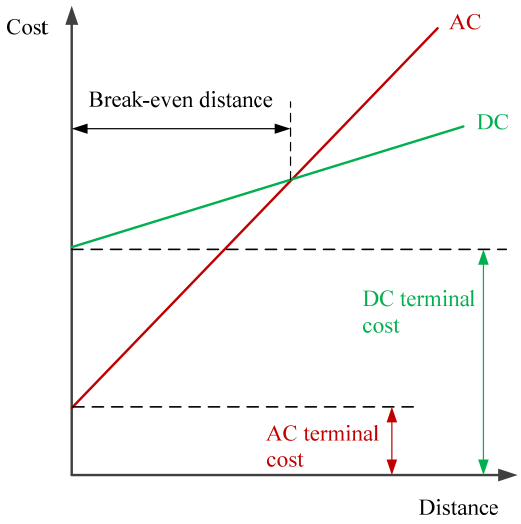

Fig.1.1 Variation of the cost of AC and DC transmission with the line length

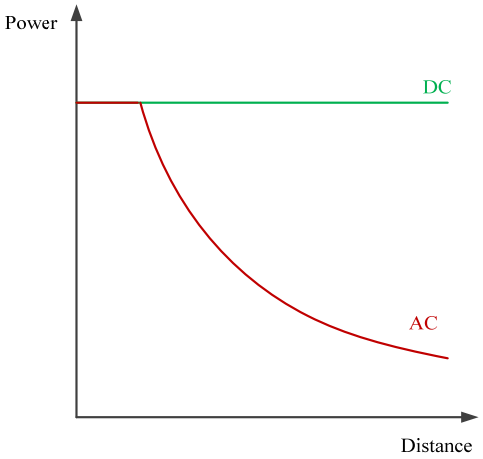

Fig.1.2. Power transfer capability versus the distance

transfer of an AC line is limited by the system stability, whereas the power transmission of a DC line is unaffected. The power carrying capabilities of an AC and a DC line are respectively presented in Fig. 1.2.

- **Power flow control:** The power flow on the HVDC links can be easily controlled through the power electronic converters. Hence compared with the AC lines, the HVDC link can stabilize the transmission network and prevent cascading outages.

Nowadays, two different types of HVDC transmission topologies are widely accepted and adopted in the modern power systems, i.e. line-commutated converter based HVDC (LCC-HVDC) applying thyristors and voltage source converter based HVDC (VSC-HVDC) applying fully controlled semiconductor devices. The former is the "classic" HVDC technology while the VSC-HVDC technology was developed during the 1990s [2]. Table 1.1 shows the characteristics of those two kinds of HVDC links.

The LCC-HVDC links have been operated with high reliability and little maintenance for more than 30 years [3-5]. With the widely use of LCC-HVDC systems, two or more HVDC links tend to feed into an AC system with short electrical distance, and form a so-called Multi-Infeed Direct Current (MIDC) transmission system [6], [7]. There are mainly three types of MIDC system, i.e. the ring type, the chain type and the complex AC/DC system [8]. The simplified schematic diagrams of the three MIDC systems are shown in Fig. 1.3.

Table 1.1
Two types of the HVDC system

	LCC-HVDC	VSC-HVDC
Devices in converter	Thyristors	IGBTs or GTOs
Operation principle	Commutation rely on the external circuit	Self-commutation
Advantages	▪ Higher voltage level and power rating ▪ Lower losses ▪ Lower cost of converter	▪ Current direction can be changed ▪ Flexible control ability ▪ Voltage support to Ac system
Disadvantages	▪ current direction cannot be changed ▪ Reactive power consumption ▪ Risk of commutation failures	▪ Lower voltage level and power rating ▪ High loss ▪ Higher cost of converter

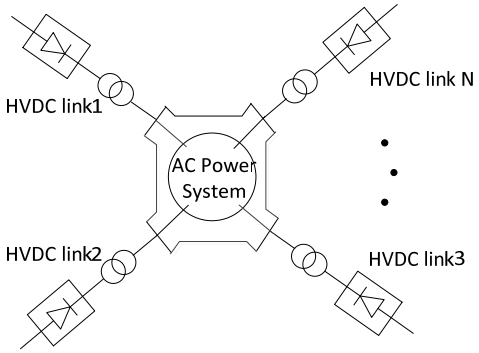

(a) Ring-type Multi-Infeed HVDC system configuration

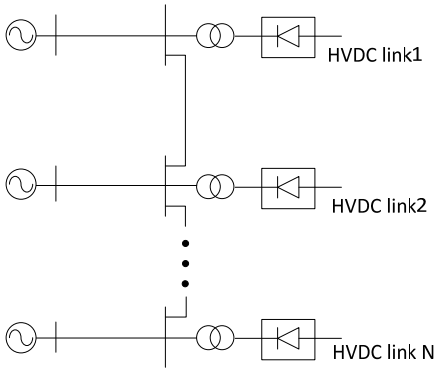

(b) Chain-type Multi-Infeed HVDC system configuration

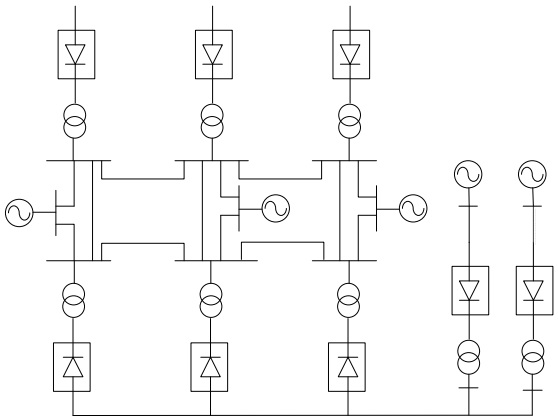

(c) A potentially complex Multi-Infeed HVDC system configuration

Fig.1.3. The types of Multi-Infeed HVDC system

In the ring type MIDC system, more than one HVDC links terminate into the same AC system from different infeed points and interconnected to each other consequently the HVDC systems are structured looks like a ring. The chain type MIDC system shows another kind of system structure which looks like a chain. The HVDC systems only connect with the nearby links, and there is no connection between the HVDC links far away. The MIDC system can also be found in the complex AC/DC hybrid systems, which are commonly existed in large electric networks, such as the North American Power system and China Southern Power Grid.

On the other hand, with increased utilization of renewable energy in recent years, the HVDC system has been adopted in more fields toward the generation and distribution sides [9], such as the offshore wind farms. Nowadays, the wind turbine system (WTS) started in the 1980s with a few tens of kW power production per unit has become large scale wind farm with multi-MW size wind turbines. The offshore wind power is getting more and more attention due to the much better wind conditions of offshore sites and large amount of potential offshore wind energy. Take the situation in Europe for example, the expected wind power generation of European Union is 230GW by 2020, in which 40GW coming from the offshore wind power plant [10]. To meet this target, large wind generation capacity from the offshore wind farms will be required. Fig. 1.4 depicts the cumulative number of wind turbines onshore and offshore in EU from 1991.

The offshore wind farms are normally located far away from the onshore infeed point, hence more attention has been paid to the work concerned with the connection of the offshore wind power to the onshore electricity networks. The HVDC transmission system would be a competitive solution for the offshore wind power integration. Thanks to the rapid development of power electronics devices, the cost of VSCs are reduced whereas the power capacity are increased, thus the VSC-HVDC link is becoming a more favorable choice for the offshore wind power integration with its advantages of reactive power supporting ability, reduced harmonics and good controllability. As a consequence, together with the existing LCC-HVDC links, a Hybrid Multi-Infeed HVDC (HMIDC) system that consists of the VSC-HVDC and LCC-HVDC links can be envisioned in the near future [11]. In comparison to the conventional MIDC systems with LCC-HVDC links introduced above, the flexible control of VSC-HVDC links brings more possibilities for the stability enhancement of the HMIDC system [12]-[14].

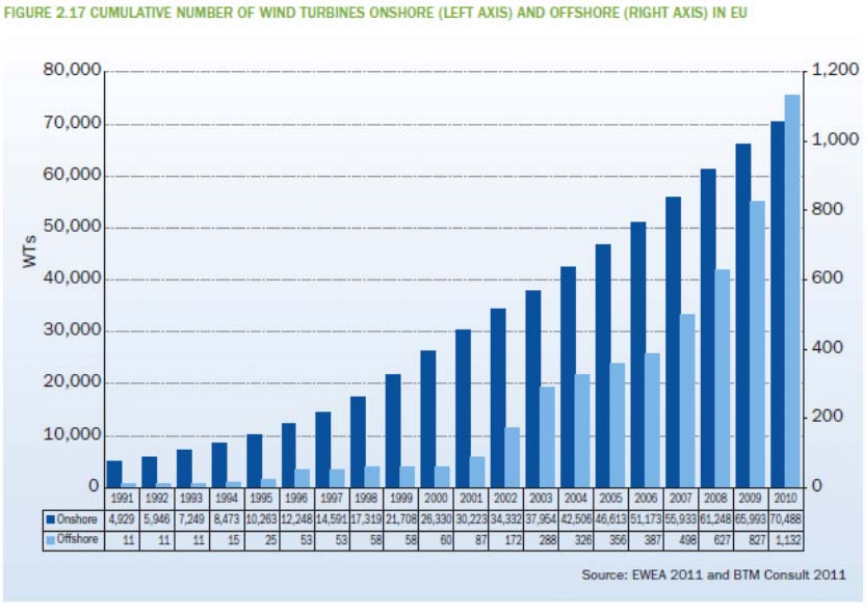

Fig. 1.4. Cumulative number of wind turbines onshore and offshore in EU from 1991[10]

1.1.2 The stability problems of HMIDC system connecting with offshore wind farm

In a MIDC system, the mutual interactions between the different HVDC links tend to bring a number of operation challenges, particularly when feeding into a weak AC grid [15]. It is known that the stable operation of the LCC-HVDC link is highly dependent on the grid voltage due to the susceptibility to commutation failure of LCCs, which means the infeed bus of LCC-HVDC link is a voltage sensitive bus in the AC system. As a consequence, the voltage dip in the infeed power system caused by grid faults may lead to larger voltage drop or even instability of the system. Therefore, the fast voltage recovery after grid faults would be very important for the stability of the HMIDC system.

On the other hand, considering the connected offshore wind farm, the variable nature of the wind speed will lead to the fluctuations in electrical variables, which consequently affect the power quality [16], [17] and bring the bus voltages variations [18]. Therefore, for a wind farm connected HMIDC system, the influence of wind power variation to the voltage at infeed buses of HVDC links plays an important role to the system voltage stability.

The Low Voltage Ride Through (LVRT) ability is another particular concern for the stability study of the HMIDC system. Since the large offshore wind farms have ratings like conventional power plants, the disconnection of a large amount of wind power during fault may result in serious stability problems, both on the system voltage and frequency. A number of grid connection codes requiring the LVRT capability have been imposed on wind power systems, which implies that the wind turbines and wind farms should be able to continuously connect to the network for a certain time period during grid faults and voltage sags [19]. Therefore, for the VSC-HVDC connected offshore wind farm, the requirement of LVRT capability offers a new challenge to the control strategies.

1.2 Research objective and approach

The research project related to this thesis concentrates on exploiting the performance of HMIDC system connecting with offshore wind farm under different external disturbances and analyzing the influences to the system stability by the VSC-HVDC link. Different from the MIDC system with only LCC-HVDC links, the reactive power support by the VSC-HVDC link in HMIDC system brings more possibilities to improve the system stability. Since the offshore wind farm is connected with the VSC-HVDC link, the cooperative control on the HVDC link and the wind farm converters are also expected for the stability improvement. Hence the main objective of this research is to develop advanced control strategies for the HMIDC system connecting with an offshore wind farm, in order to achieve the maximum use of VSC-HVDC link for enhancing the AC system stability.

1.2.1 Problem statement

Fig. 1.5 illustrates a simplified diagram of the HMIDC system, and the main research areas of this project are marked by the dashed box in the figure. It can be seen from the figure that the scope of the project is divided into two parts, one is the stability analysis of the AC system applying different HVDC links and the other is the development of the control strategies on VSC-HVDC and offshore wind farm. Hence, the aims of the project can be listed as the following statements:

- *How to model the realistic HMIDC system, in which all the influence to system stability by system parameters and HVDC links can be presented? How is the HMIDC system performing under grid faults and disturbances from wind farm? And how to assess the*

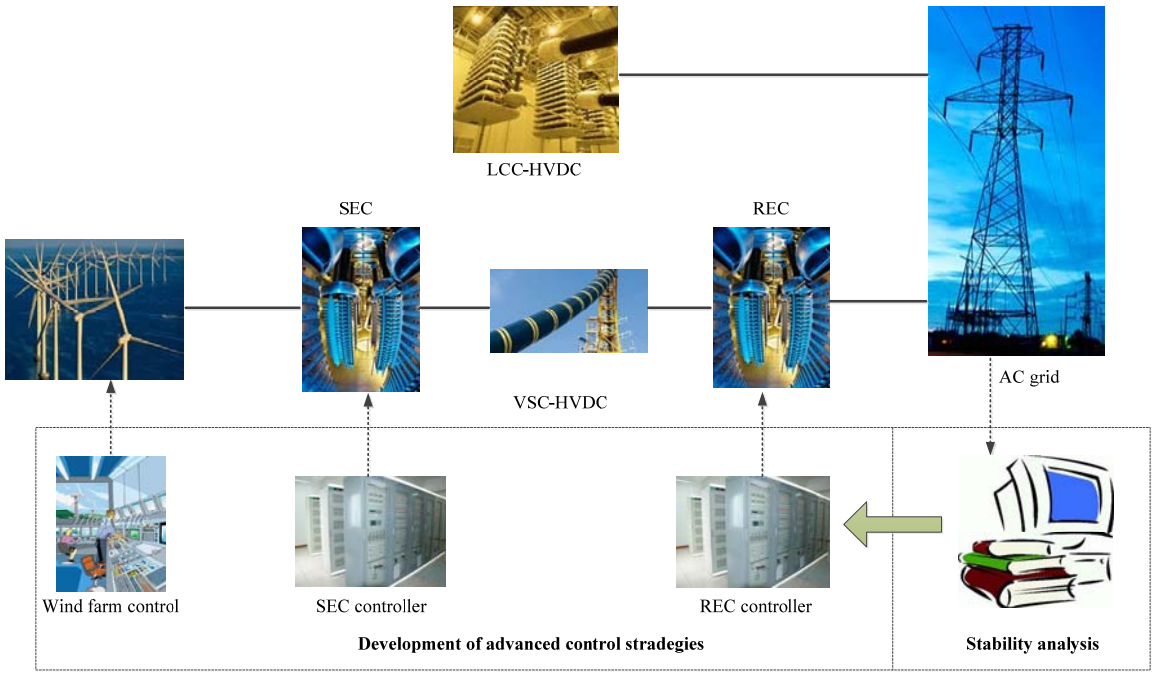

Fig. 1.5. Main research areas of the project

system stability quantitatively through a suitable indicator?

- *What are the limitations of the conventional control methods on VSC-HVDC link for its voltage support ability? How to overcome those limitations on VSC-HVDC link and enhance the stability of HMIDC system through VSC-HVDC link.*

On the basis of the above research problems, the main tasks of the project are explained as follows:

- **The HMIDC system modeling:** As the first step of stability study of a power system, the realistic system model should be developed. As explained before, the offshore wind farms become the new trend of wind power development in Europe. For example, by 2030, EWEA expects 400 GW of wind energy capacity to be operating in the EU, out of which 150GW will be offshore [10]. Considering the existing LCC-HVDC links in Danish power system, the HMIDC system model is established based on the future possible western Danish power grid with two different HVDC links.
- **System Effective Short Circuit Ratio (ESCR) calculation:** Under the built HMIDC system model, the influences of system parameters and the VSC-HVDC link on the

system voltage stability can be evaluated. In order to get a clearly understanding of the system strength, an index is needed for the system voltage stability assessment. For the power system applying HVDC links, the ESCR is normally used to indicate the system voltage stability, whereas the traditional way of calculating ESCR is not applicable in HMIDC system due to the influence of VSC-HVDC link. Thus a new calculation method for the ESCR is required for the HMIDC system, which can provides a quantitative tool for assessing the contributions of the system parameters and the VSC-HVDC link to the system voltage stability.

- **Flexible control schemes of VSC-HVDC link:** Through the different control strategies, the VSC-HVDC can be used to enhance the HMIDC system voltage stability. Therefore, the improved control methods on VSC-HVDC link are expected against different disturbances, for example, grid faults or wind power fluctuations, so that the maximum use of the reactive power support capability of the VSC-HVDC link can be achieve.
- **Cooperative control on VSC-HVDC and wind farm for Low Voltage Ride Through (LVRT) ability:** In the HMIDC system comprising offshore wind farm at the sending end of the VSC-HVDC link, the LVRT ability is one of the most important operation requirement. It is demanded that the wind turbines remain connected and actively contribute to the system stability during and after the onshore grid fault, otherwise the loss of the large power transmission will result in serious stability problem. To meet this requirement, it is needed to develop a cooperative control strategy of the VSC-HVDC system and the connected offshore wind farm.

1.2.2 Used tools

The Electromagnetic power transient software EMTDC®/PSCAD® is used as the simulation platform in this project. The EMTDC® stands for the Electromagnetic Transients including DC represents and solves differential equations for both electromagnetic and electromechanical systems in the time domain. It is firstly developed by Dr. Dennis Woodford in Manitoba at1976, and becomes the most widely adopted simulation software in the area of power system in world wide. The user interface of EMTDC® is named PSCAD®, which stands for the Power System Computer Aided Design. Through the PSCAD, users can built the system model and make the simulation through Fortran® in EMTDC conveniently.

As a powerful tool of the electromagnetic transient simulation, the EMTDC®/PSCAD® is very suitable for the simulation study of HVDC link and its control system [20], [21]. Moreover, the user defined models in PSCAD® allows the development of self-defined control components, which supplies a desired environment of controller study to the users

On the other hand, the MATLAB® is also applied for the numerical calculations in the project. Some of the variables in the developed control system need to be calculated by the MATLAB. The interface to MATLAB® in EMTDC®/PSCAD® achieves the convenient and reliable interconnection of the two simulation tools.

1.2.3 Limitations

Several limitations are considered in this project to simplify the analysis and design.

- For simplicity, the influence to system stability from the sending end grid of LCC-HVDC link is not considered in this research, and the sending end system is modeled as an infinite bus in the system model.
- During the stability analysis, only the symmetrical faults are considered and investigated in the studied system.
- The wind power influence to the system stability is investigated in this work, whereas the influence of the tower shadow and wind shear are ignored here since the power fluctuation caused by the wind speed variation is the main concern in this research.

1.3 Thesis outline

The thesis is organized into seven chapters, and the short descriptions are provided below for each chapter.

Chapter 1 Introduction

The background and motivation of the project is firstly explained in this chapter. After that, the research objectives and approaches are provided. According to the formulation of research problems,

the specific research tasks are confirmed in the project. Lastly, the tools used in this research are presented in this chapter, as well as the limitations of this project.

Chapter 2 Modeling of the HMIDC system

This chapter describes the layout and modeling of the HMIDC system. The operation and control of LCC-HVDC and VSC-HVDC systems are firstly introduced in this chapter. On the basis of that, the studied system is modeled according to the western Danish power system, where the LCC-HVDC link and the VSC-HVDC link feed into one AC grid via two buses, respectively, and are interconnected through a tie-line. The system parameters are given here and the system load flow under steady state is presented on the established model.

Chapter 3 Voltage stability analysis and the assessment index of HMIDC system

This chapter presents the system voltage performances under the grid fault situations. The influences to system voltage stability by the system parameters and VSC-HVDC link are evaluated in this chapter. In light of this, a new calculation method for the Effective Short Circuit Ratio (ESCR) is formulated for the HMIDC system, which provides a quantitative tool for assessing the contributions of the system parameters and the VSC-HVDC link to the system voltage stability.

Chapter 4 Flexible Power control method on VSC-HVDC link in the HMIDC system

This chapter proposes a flexible power control scheme on the VSC-HVDC link in HMIDC system in order to improve the system voltage stability. The approach employs an adaptive current limiter to dynamically adjust the active current reference based on the output of the AC voltage controller, such that the maximum use of reactive power support capability of the VSC-HVDC link can be achieved. The sending end fault is also considered in the control method development, and an operation mode switch is designed in the control system to keep a stable operation of the VSC-HVDC link during sending end disturbances. Simulation studies in different cases in EMTDC/PSCAD are carried out to verify the proposed control scheme.

Chapter 5 Cooperative control of VSC-HVDC Connected Offshore Wind Farm with LVRT Capability

In this chapter, the LVRT capability of VSC-HVDC connected offshore wind farm is the main concern in the HMIDC system. The variable speed Squirrel-Cage Induction Generator (SCIG) wind

farm is modeled in this chapter and connected with the VSC-HVDC system. In order to satisfy the grid connection codes for LVRT of the wind farm, this chapter proposes a cooperative control strategy for variable speed SCIG-based offshore wind farm connecting with VSC-HVDC system. And the effectiveness of the control method is confirmed by the simulation results.

Chapter 6 The voltage sensitivity based control method in HMIDC system connecting with offshore wind farm

This chapter proposes a voltage sensitivity based control method on the VSC-HVDC link to mitigate the system voltage fluctuation caused by the wind power variation. The control scheme provides variable reactive power references according to the active power delivered from the wind farm by HVDC link and the system voltage sensitivity factors, thus effectively reduce the voltage fluctuation in the studied system. The verification of the proposed control method is carried out using EMTDC/PSCAD interconnected with MATAB.

Chapter 7 Conclusion

This chapter summarizes the main works, contributions and results of this project, and provides the possible directions in the future research.

1.4 List of publications

1. Y. Liu and Z. Chen, “Stability analysis of multi-infeed HVDC system applying VSC-HVDC,” in *Proc. of IEEE PES General Meeting 2010*, pp. 1-7.
2. Y. Liu and Z. Chen, “Transient Voltage Stability Analysis and Improvement of A Network with different HVDC Systems,” in *Proc. of* IEEE *PES General Meeting 2011*, pp. 1-8.
3. Y. Liu and Z. Chen, “Short Circuit Ratio analysis of multi-infeed HVDC system with a VSC-HVDC link,” in *Proc. of IEEE IECON 2011- 37th Annual Conference on IEEE Industrial Electronics Society*, pp. 949-954.
4. Y. Liu and Z. Chen, “Power Control Method on VSC-HVDC in a Hybrid Multi-infeed HVDC system,” in *Proc. of IEEE PES General Meeting 2012*, pp. 1-8.
5. Y. Liu, X. Wang and Z. Chen, “Cooperative Control of VSC-HVDC Connected Offshore Wind Farm with Low-Voltage Ride-Through Capability,” in *Proc. of IEEE POWERCON 2012,* pp. 1-8.
6. Y. Liu and Z. Chen, “Voltage Sensitivity Based Reactive Power Control on VSC-HVDC in A Wind Farm Connected Hybrid Multi-Infeed HVDC System,” in *Proc. of IEEE POWERTECH 2013*, in review.
7. Y. Liu and Z. Chen, “A Flexible Power Control Method of VSC-HVDC Link for the Enhancement of Effective Short-Circuit Ratio in a Hybrid Multi-Infeed HVDC System,” *IEEE Trans. Power System*, accepted for publication.

Bibliography:

[1] S. Cole and R. Belmans, “Transmission of bulk power,” IEEE Ind. Electron. Mag., vol. 3, no. 3, pp. 19–24, Sep. 2009.

[2] G. Asplund, K. Eriksson, and K. Svensson, “DC transmission based on voltage source converters,” in Proc. CIGRE SC14 Colloq. South Africa, 1997, pp. 1-7.

[3] R. Li, S. Bozhko, and G. Asher, “Frequency control design for offshore wind farm grid with LCC-HVDC link connection,” IEEE Trans. Power Electron., vol. 23, no. 3, pp. 1085–1092, May 2008.

[4] N. M. Kirby, L. Xu, M. Luckett, and W. Siepman, “HVDC transmission for large offshore wind farms,” IEE Power Eng. J., vol. 16, no. 3, pp.135–141, Jun. 2002.

[5] J. Arrillaga, High Voltage Direct Current Transmission. London, U.K.: IET, 1998.

[6] L. X. Bui, V. K. Sood, and S. Laurin, “Dynamic interactions between HVDC systems connected to AC buses in close proximity,” IEEE Trans. Power Del., vol. 6, no. 1, pp. 223-230, Jan. 1991.

[7] I. T. Fernando, K. L. Kent. J. B. Davies, E. Rahimi, A. M. Gole, “Parameters for planning and evaluation of Multi-infeed HVdc schemes,” in Proc. CIGRE 2007 Osaka Symposium. 2007.

[8] S. Su, K. Ueda, K. Tanaka, K. Takenaka, G. Wu, "Study of coordinate Control method to Improve Stability on Multi -Infeed HVDC system, " in Proc. Power System Technology, 2006, pp. 1-6.

[9] J. W. Feltes, B. D. Gemmell, and D. Retzmann, “From smart grid to super grid: Solutions with HVDC and FACTS for grid access of renewable energy sources,” in Proc. IEEE Power and Energy Soc. General Meeting, Jul. 24–29, 2011, pp. 1–6.

[10] European Wind Energy Association, “Pure Power Wind Energy Targets for 2020and 2030,” 2009 update. Available on line: http://www.ewea.org.

[11] J.W. Feltes, B.D. Gemmell, and D. Retzmann, “From Smart Grid to Super Grid: Solutions with HVDC and FACTS for grid access of renewable energy sources,” in Proc. IEEE PES General Meeting, 2011, pp:1-6.

[12] C. Zhao, and Y. Sun, “Study on control strategies to improve the stability of MULTI-INFEED HVDC systems applying VSC-HVDC,” in Proc. IEEE Electrical and Computer Engineering Conf., 2006, pp.2253-2257.

[13] C. Guo, and C. Zhao. “Supply of an Entirely Passive AC Network through a Double-Infeed HVDC System,” IEEE Trans. Power Electron., vol. 25, no. 11, pp. 2835- 2841, Nov. 2010.

[14] Q. Zhong, Y. Zhang, L. Lin, et al, “Study of HVDC light for its enhancement of AC/DC

[15] J. Reeve and S. P. Lane-Smith, “Multi-infeed HVDC transient response and recovery strategies,” IEEE Trans. Power Del., vol. 8, no. 4, pp. 1995-2001, Oct. 1993.

[16] T. Sun, Z. Chen, and F. Blaabjerg, “Flicker study on variable speed wind turbines with doubly fed induction generators,” IEEE Trans. on Energy Conversion, vol. 20(4), 2005, pp. 896–905.

[17] Y. S. Kim and D. J. Won, “Mitigation of the flicker level of a DFIG using power factor angle control,” IEEE Trans. on Power Delivery, vol. 24(4), 2009, pp. 2457–2458.

[18] A. Larsson, “Flicker emission of wind turbines during continuous operation,” IEEE Trans. on Energy Conversion, vol. 17(1), 2002, pp. 114–118.

[19] M. Tsili, S. Papathanassiou, “A review of grid code technical requirements for wind farms,” IET Trans. Renewable Power Generation, vol. 3, no. 3, pp. 308-332, 2009.

[20] Pscad user’s guide. Canada: Manitoba HVDC Research Center, 2003.

[21] EMTDCuser’s guide. Canada:Manitoba HVDC Research Center, 2003.

Chapter 2

Modelling of Multi-infeed HVDC system

This chapter presents the modelling of studied HMIDC system based on western Danish power grid. The system layout is firstly given here, followed by the detailed explanations of different types of HVDC links. Lastly, the load flows of the HMIDC system under steady state and grid fault situations are described in this chapter.

2.1 Introduction

The modeling of studied system is the basis of a worthy research. In order to investigate the stability of the HMIDC system, a detailed system model is required firstly. Several HMIDC system models were developed in the previous literatures [1]-[3], whereas all of which have certain limits for the stability analysis. In [1], the VSC-HVDC and LCC-HVDC links feed into an AC grid represented by a voltage source in series with grid impedance, which neglect the dynamic interactions between the HMIDC system and the AC network as well as the impact of electric loads. Recently, the HMIDC system feeding a passive network constituted by the exponential static load and induction motor load was built in [2]. In such system, the load impact on the voltage stability was discussed, whereas the dynamic behavior of AC network was not involved. In [3], a HMIDC system including two LCC-HVDC links and one VSC-HVDC link was developed, where neither the AC grid dynamics nor the load effect were considered.

In view of that, a more realistic system model is required for the stability study of HMIDC system. Hence the studied HMIDC system is modeled based on the western Danish power system in this research, where both the AC system dynamics and electrical load influences are taken into account in the model established.

2.2 The HMIDC system modelled based on Danish power grid

2.2.1 The HMIDC system layout

Denmark is electrically divided into two parts—western Danish power system and eastern Danish power system. Fig.2.1 shows the geographic distribution of the western Danish power system [4]. The western Danish transmission system operates at 400 kV and 150kV, and connects to the Germany power system via 400 kV and 220kV ac lines at the South part [4]. Three LCC-HVDC links have been adopted in the western Danish power system, which connect it to the Nordel synchronous area at north part and to the eastern Danish power grid at east part. As shown in Fig.2.1, the western Danish power system is connected to the Norwegian system through "HVDC 1" and to the Sweden power grid through "HVDC 2". The "HVDC 3" connects the western and eastern Danish power system and was put in use at 2010.

A large amount of dispersed generation has been implemented into the western Danish power grid since the early 80s. And the wind power generation is increased rapidly and becoming a large part of the dispersed power production in Denmark. The development of the power balance in western Denmark can be found in [5]. A lot of the offshore wind energy around Denmark can be found at its western sea, hence a wind power plant can be envisioned in the future as shown in Fig. 2.1. As explained in the last chapter, the flexible control ability makes VSC-HVDC a competitive choice for the wind power integration. Thus the planned offshore wind farm is assumed connecting to the onshore power system through a VSC-HVDC link. As a consequence, a HMIDC system is formed in the marked area in Fig.2.1, and the simplified one-line diagram of this studied HMIDC system is illustrated in Fig. 2.2.

The LCC-HVDC link in Fig.2.3 represents the HVDC 1 in Fig.2.1, while the VSC-HVDC denotes the planned HVDC link (HVDC 4) in Fig.2.1. The transmission line between two infeed buses of the HVDC links is modeled as the tie line in Fig.2.2. The sending ends of the HVDC links are represented by the voltage sources S1 and S2 for the sake of simplicity.

2.2.2 The infeed AC system model

Considering the dynamic behavior of the infeed AC network, two interconnecting synchronous

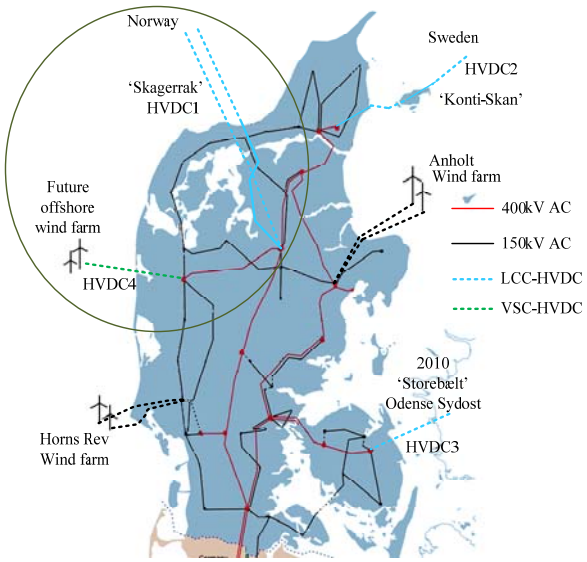

Fig. 2.1. Western Danish transmission grid.[6]

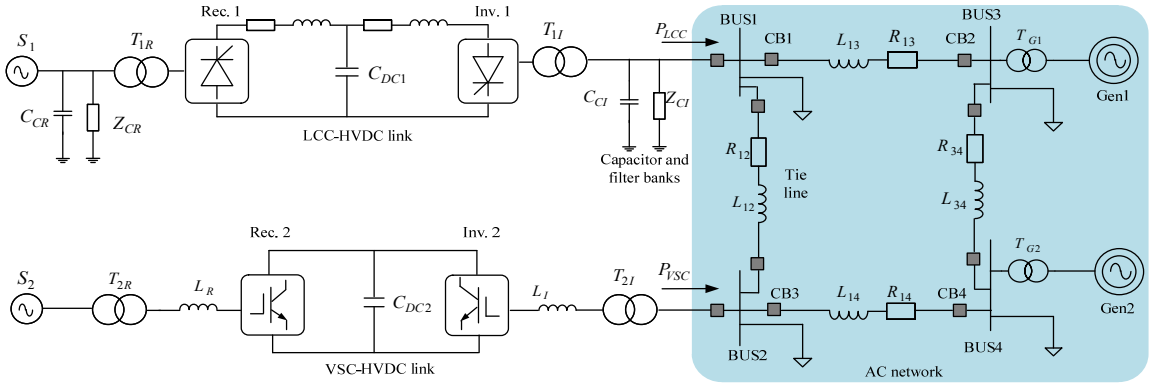

Fig. 2.2. Simplified one-line diagram of the built HMIDC system.

generators (Gen 1 and Gen 2), and the electrical loads in Fig.2.2 are modeled to constitute the infeed AC grid in Fig.2.1.

Fig.2.3 illustrates the block diagram of the excitation system model for the synchronous generators, which adopts the IEEE type Alternator Supplied Rectifier Excitation System No. 1 (AC1A) in [7]. The AC1A model uses an alternator with the non-controlled rectifier for producing the field current. The terminal voltage of the generator V_C is first compared with the reference voltage V_{REF}, and then

the voltage error is passed through a regulator, which generates the voltage V_R for the exciter in Fig. 2.3. The field voltage E_{FD} is thus regulated to keep the reference voltage V_{REF} of the generator. The sample parameters given in [7] are used in this system.

It is noted that for each generator, the ability of controlling the terminal voltage is limited by the capacity of generator and the reactive power margin. In the studied system, the power factor of each generator is kept higher than 0.8, i.e. the maximum reactive power support has been set as 60% of the capacity

Fig. 2.4 shows the diagrams of the steam turbine model and the associated speed-governing system adopted by the generators. The Generic Turbine Model (TUR 1) is adopted as the turbine systems, and the approximate nonlinear mechanical-hydraulic speed-governing (GOV 1) is used as the speed governors for the generators Gen 1 and Gen 2 [8].

The speed governing system consists of a speed regulator, speed relay and a servomotor. The main distinct component in this system is the speed governor, which uses the reciprocal of the primary frequency droop, K_G, to regulate a valve position that indicates the synchronous generator speed. The output of GOV 1 is passed to the TUR 1 model which is based on the approximate linear model of the Tandem Compound Double Reheat system. The typical parameters of the GOV 1 and TUR 1 given in [9] are used here.

The electrical load adopted in the model is the comprehensive load including the static loads and dynamic loads. The exponential load model is used to represent the static loads, which are given by [10],

$$P = P_0 \left(\frac{V}{V_0} \right)^{NP} \left(1 + K_{PF} \cdot dF \right) \tag{2.1}$$

$$Q = Q_0 \left(\frac{V}{V_0} \right)^{NQ} \left(1 + K_{QF} \cdot dF \right) \tag{2.2}$$

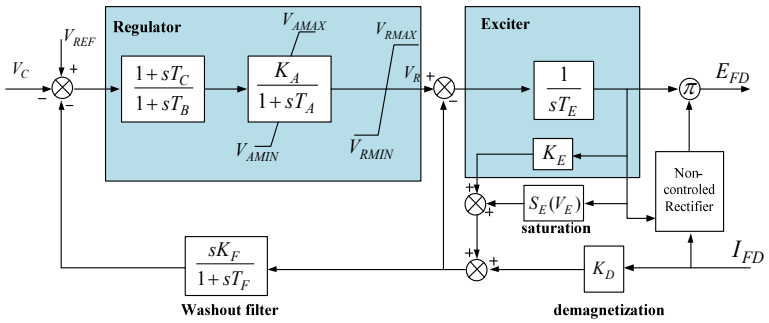

Fig. 2.3. Block diagram of the AC1A excitation system

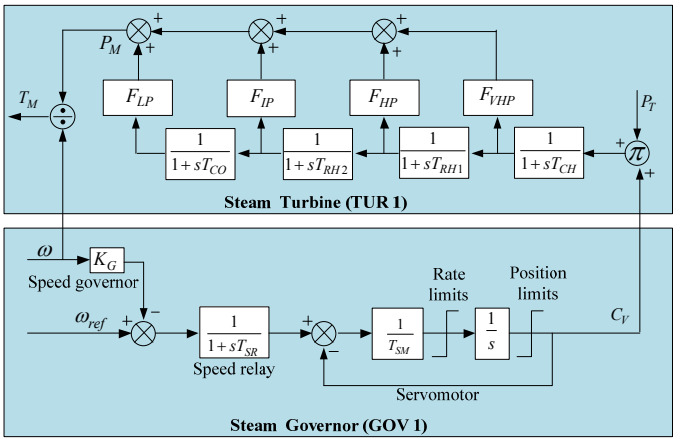

Fig. 2.4. Block diagram of the governor model and steam turbine.

where P and Q are the active and reactive power of the load when the bus voltage magnitude is V. P_0 and Q_0 are the load active and reactive power when the bus voltage is V_0(the rated voltage), and the system frequency, F, has no error. The NP, NQ, K_{PF} and K_{QF} represent the load characteristics to voltage and frequency, respectively, which can be typically chosen as NP=NQ= 2.0, K_{PF}=1, K_{QF}=-1.

The system voltage stability is heavily dependent on the load characteristics. It is known that the induction machine is sensitive to the variation of system voltage, which is a typical load for voltage stability analysis. Thus, induction motor loads are considered as the dynamic loads in the system.

2.3 Operation and control of LCC-HVDC system

2.3.1 Components of LCC-HVDC system

The LCC-HVDC link in the studied system adopts the widely accepted CIGRE benchmark model [11]. The classical monopolar LCC-HVDC system consists of the DC cables, line commutated converters, AC filters, transformers, and reactive power compensation equipment, e.g. shunt capacitor banks. In the CIGRE benchmark model, the power rating of the HVDC link is 1000MW with 500kV DC voltage, and the LCC is a 12-pulse bridge which modeled by two 6-pulse bridges connecting in series. The fixed capacitors and damped filters are used in this model as the reactive power compensators and AC filters. Fig. 2.5 shows the one-line diagram of the converter station in the CIGRE benchmark model of LCC-HVDC system.

2.3.2 Control method of LCC-HVDC system

The control system of HVDC link is normally divided into three layers, i.e. the power or current control layer (first layer), the pole control layer (second layer) and the valve control layer (third layer). In the first layer, the current order for the HVDC system is calculated based on the power reference comes from the dispatching centre. The power support function of the HVDC link, for example, fast power change or the frequency control, is implemented in this layer [12]. The firing angle for achieving the required power transmission is obtained in the second layer, including the constant current controller, constant extinction angle (γ) controller, current error controller and the voltage Dependent Current Order Limiter (VDCOL) [13]. The third layer focus on getting the triggering pulse and its synchronous signals so as to trigger the thyristors accurately.

For the control of LCC-HVDC link in the studied system, the first layer belongs to the system level and the third layer can be ignored under the assumption of ideal triggering, thus the main concern in the control system modelling is the second layer, i.e. the pole control.

Fig.2.6 shows the conventional control characteristics of a LCC-HVDC link including the Voltage Dependent Current Limit (VDCL). The green line in the figure gives the DC voltage at rectifier side (station 1) versus DC current and red curve shows the DC voltage at inverter side (station 2) versus

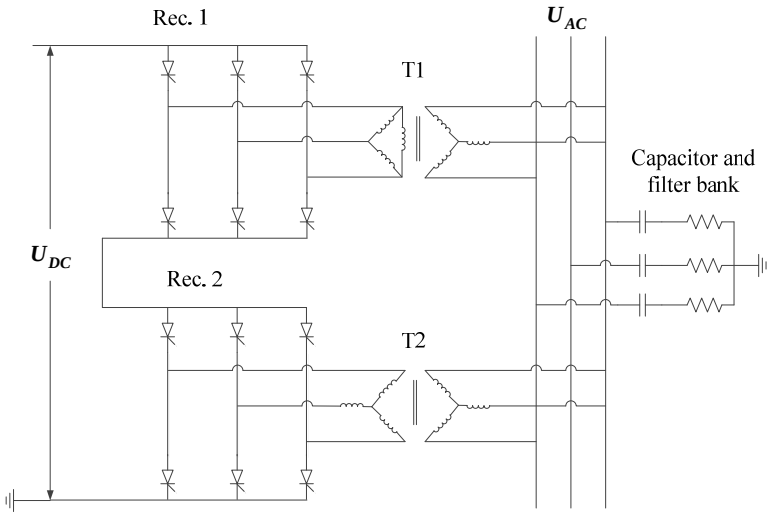

Fig.2.5 The converter station in the CIGRE benchmark model

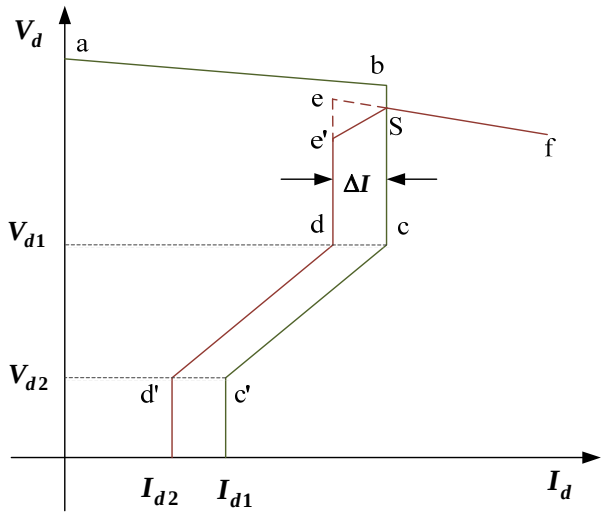

Fig.2.6. Converter controller characteristics

DC current. The different parts of each station characteristic can be summarized and shown in the Table 2.1.

TABLE 2.1
Control modes of the two stations

Station 1	Control type	Station 2	Control type
ab	Minimum α	ef	Minimum γ
bc	Constant current	ed	Constant current
cc’	VDCL	dd’	VDCL

The intersection of the two characteristics (point S in Figure 2.6) shows the steady state operation point of the HVDC link, at which the rectifier operates under the constant current control and the inverter operates under the constant (minimum) extinction angle control. There are several reasons below for which the current control is desirable to be adopted at the rectifier station under normal conditions.

- The increase of power in the link is achieved by reducing α (firing angle of the rectifier) which improves the power factor.
- The inverter can now be operated at minimum γ (extinction angle of inverter), thereby minimizing the reactive power consumption at inverter.
- The current during line faults are automatically limited with rectifier station in current control.

According to the control characteristics, the block diagram of the pole controller can be drawn in Fig. 2.7. Under steady state, because of the current difference order ΔI , the minimum extinction angle control loop is chosen in the inverter control system, and the constant current controller is applied at the rectifier.

Note that in order to avoid the possible instability of the control which will result in hunting between different operation modes [14], a small modification of the control characteristics is achieved in Fig. 2.6. That modification is the change of the slope between point ‘e’ and point ‘S’, i.e. applying segment ‘e′S’ instead of ‘eS’ in the red curve in Fig.2.6. The positive slope between I_{d1} and I_{d2} can eliminate the instability problem and achieved by the ramp compensation in Fig.2.7.

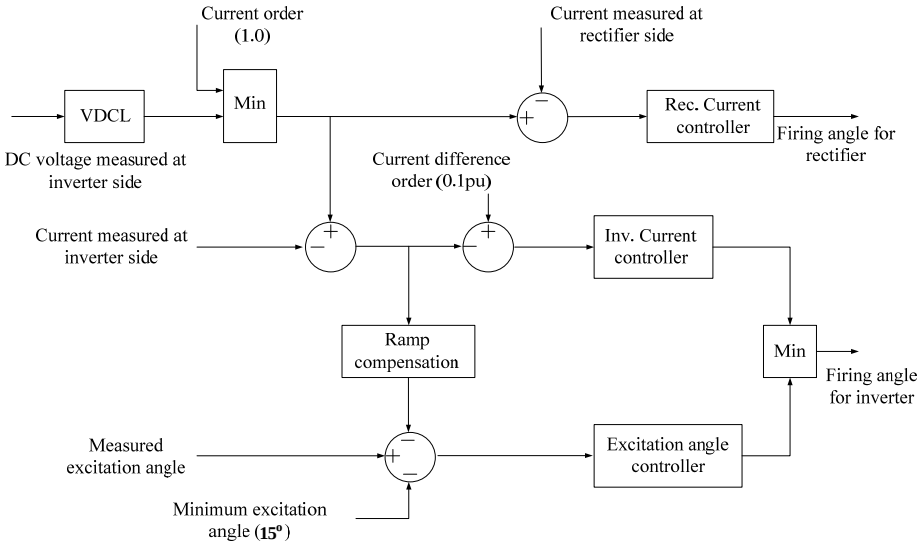

Fig.2.7. Block diagram of the pole controller

It is known that the low DC voltage in the LCC-HVDC link is mainly due to the faults in the AC side, which may result in persistent commutation failure. In such case, it is necessary to reduce the DC current in the link until the conditions that led to the reduced DC voltage are relieved. Thus the VDCL is applied in the control system to make the control characteristic shown as ‘cc’’ and ‘dd’’ during the low DC voltage situation. That means the DC current would be reduced from the steady stated value when the DC voltage drops down below a certain value, i.e. V_{dl} in this case.

2.4 Operation and control of VSC-HVDC system

2.4.1 Components of VSC-HVDC system

The VSC-HVDC system model in the HMIDC system consists of the transformers, the VSCs, the phase reactors, and the DC cables. The three-phase two-level bridges based on the IGBT power devices are adopted to represent the VSCs. Fig. 2.8 shows the three lines diagram of the VSC station in this HVDC link.

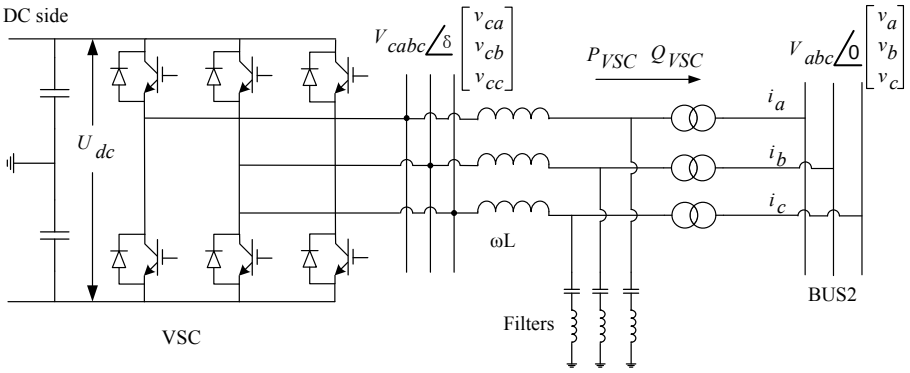

Fig.2.8. Three line diagram of the VSC station

In the figure, P_{VSC} and Q_{VSC} are the active and reactive power of VSC-HVDC link at grid side. i_a, i_b, i_c are three phase instantaneous current before AC bus. V_{cabc} is the rms value of line to line voltage at output of converter and v_{ca} , v_{cb}, v_{cc} are the instantaneous phase voltages there. In the same way, V_{abc} is the rms value of line to line voltage at AC bus and v_a, v_b, v_c are instantaneous phase voltages there. δ is the phase angle difference between V_{cabc} and V_{abc}. V_{dc} is the DC voltage.

As shown in Fig. 2.8, the two-level converter consists of six valves. It is capable of generating the two voltage levels $-0.5V_{dc}$ and $+0.5V_{dc}$. The two-level bridges also can be used in high power applications by series connection of the devices. In that way each valve can be built up by a number of series connected switches and their anti-parallel diodes.

High frequency harmonic components can be observed at the output bus voltage of the VSC, which is normally caused by the switching of the IGBTs. In order to prevent the harmonics injecting into the AC system, High-pass filter branches are installed parallel at the output side of the VSC after the phase reactors to absorb the high frequency harmonics, as shown in Fig. 2.8. Note that different from the LCC-HVDC system, the VSC-HVDC link can support the reactive power to the system, thus the amount of filters in Fig. 2.8 would be much smaller than that in Fig. 2.5 of the LCC-HVDC link.

At the DC side, the DC capacitors are designed as an energy buffer to reduce the DC voltage ripple. Two capacitor stacks are connected in series with the same size to model the DC capacitor,

and the parameters of the capacitors are determined by the DC voltage level and the power capacity of the converter in the HVDC link[15].

2.4.2 Control method of VSC-HVDC system

There are two main control strategies for VSC-HVDC link, which can be named as the AC voltage control and d-q current control. Since the control structure and principal are the same at both ends of the converters, only the receiving end VSC is considered in the control method explanation below.

2.4.2.1 AC voltage control

According to the power equations, the active and reactive power of the VSC-HVDC link in Fig.2.8 can be derived as

$$P_{VSC} = \frac{V_{cabc} V_{abc}}{X} \sin\delta \tag{2.3}$$

$$Q_{VSC} = \frac{V_{cabc} V_{abc} \cos\delta - V_{abc}^2}{X} \tag{2.4}$$

where, X is the equivalent reactance include the output inductance of VSC and the leakage inductance of the transformer. Normally, the phase angle difference between the grid voltage and VSC voltage, δ, is very small, hence it is reasonable to assume that $\sin\delta = \delta, \cos\delta = 1$. Then the (2.3) and (2.4) can be approximately presented by

$$P_{VSC} = \frac{V_{cabc} V_{abc}}{X} \delta \tag{2.5}$$

$$Q_{VSC} = \frac{V_{abc}\left(V_{cabc} - V_{abc}\right)}{X} \tag{2.6}$$

The AC voltage control method uses the proportional relationship between active power and phase angle difference in (2.5) to regulate the active power and directly regulate the bus voltage through the

voltage magnitude controller. Fig.2.9 depicts the block diagram of the voltage control method, which including three parts: DC voltage control, AC voltage magnitude control and PWM firing.

In this control scheme, the phase angle shift signal, 'sh', obtained through the DC voltage controller is used to achieve a reference DC voltage in the system. And the magnitude of the modulating wave, 'M', comes from the AC voltage controller is used to keep the bus voltage constant. These two control signals thus form the modulation wave V^*, as shown in Fig.2.9.

The control principle of the AC voltage control method is relatively simple. The disturbance of AC voltage can be feedback immediately and corrected quickly by the voltage loop since the magnitude of the voltage modulation wave is obtained directly from the detected AC voltage error. Hence the fast voltage regulation can be achieved under this control method. However, it is worthy to note that this control mode ignore the influence of phase difference to the reactive power and also the voltage magnitude to the real power.

2.4.2.2 D-q current control

The d-q current control strategy is based on the theory of synchronous rotating coordinate and has been used in most kinds of situations applying voltage source converters [16]. The basic idea behind the vector current control method is to align the *d*-axis of the reference frame to the grid voltage vector, such that the active power and reactive power can be independently controlled using the active and reactive current control loops [17].

As shown in Fig.2.8, the grid side AC voltage V_{abc} can be derived as

$$\begin{bmatrix} v_a \\ v_b \\ v_c \end{bmatrix} = L\frac{d}{dt}\begin{bmatrix} i_a \\ i_b \\ i_c \end{bmatrix} + \begin{bmatrix} v_{ca} \\ v_{cb} \\ v_{cc} \end{bmatrix} \tag{2.7}$$

where v_a, v_b and v_c denote the three-phase grid voltage, i_a, i_b and i_c are the three-phase output current. v_{ca}, v_{cb} and v_{cc} are the three-phase VSC output voltage. L denotes the grid-side inductance including the phase reactor and transformer leakage inductance. With the Park transformation, the VSC model

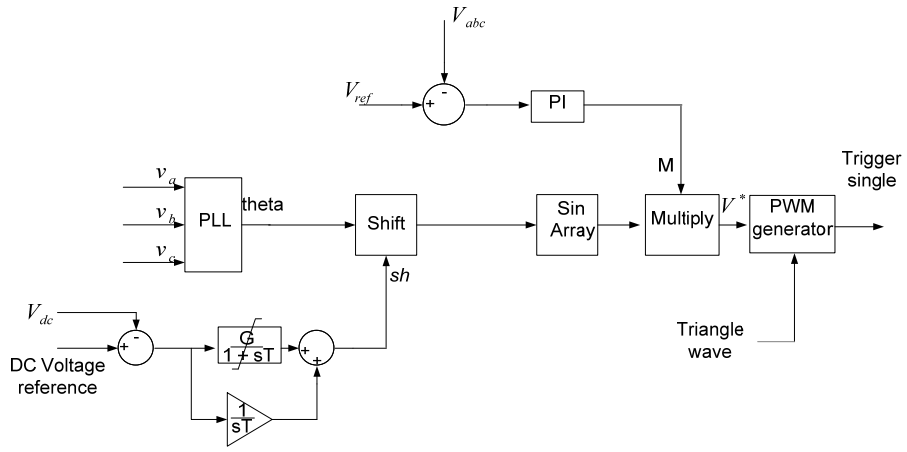

Fig.2.9 Block diagram of the AC voltage control method

is expressed in the *dq*- reference frame rotating at ω as:

$$V_d = L\frac{di_d}{dt} - \omega L i_q + V_{cd} \tag{2.8}$$

$$V_q = L\frac{di_q}{dt} + \omega L i_d + V_{cq} \tag{2.9}$$

Where V_d and V_q are the AC bus voltages in d- and q-axis, V_{cd} and V_{cq} are the grid- side converter output voltages in d- and q-axis, i_d and i_q are the grid side converter currents in d- and q-axis. The active power and reactive power flow between the grid and the grid-side converter can be presented as

$$\begin{bmatrix} P_{VSC} \\ Q_{VSC} \end{bmatrix} = \frac{3}{2} i_d \begin{bmatrix} V_d \\ V_q \end{bmatrix} + \frac{3}{2} i_q \begin{bmatrix} V_q \\ -V_d \end{bmatrix} \tag{2.10}$$

By using the Phase Locked-Loop (PLL), the voltage vector is aligned to the *d*-axis in the *dq*-coordinate, such that V_q is zero and V_d is the grid voltage amplitude. As a consequence, the active

power and reactive power exchanged between the grid and VSC would be proportional to i_d and i_q, respectively.

$$\begin{bmatrix} P_{VSC} \\ Q_{VSC} \end{bmatrix} = \frac{3}{2} i_d \begin{bmatrix} V_d \\ 0 \end{bmatrix} + \frac{3}{2} i_q \begin{bmatrix} 0 \\ -V_d \end{bmatrix} \tag{2.11}$$

According to the (2.8) and (2.9), Fig. 2.10 shows the block diagram of the vector current control method, which include the inner current control loop and outer power control loop.

The outer power control loop is used to generate the current references for regulating the output active power and reactive power of the VSC-HVDC link. Depending on the different control purposes, the active current reference can be obtained through either DC voltage control loop or active power control loop. The reactive current reference can be derived from either reactive power or AC voltage control loop [18].

In the case that the HVDC link connects to a weak system or a passive network, the AC voltage controller can be used to stabilize the system voltage. In the other case that the infeed system is strong, the reactive power controller can be adopted by the VSC-HVDC link. Notice that for a HVDC system, the power flows into and out of DC link must be equal, neglecting the DC losses. Thus, if the receiving-end converter uses active power control, the DC voltage needs to be controlled on the sending-end converter, and vice versa.

2.4.3 Comparison of the two different control schemes

Compare these two control strategies, under the same system condition, the response time of AC voltage regulation would be smaller with the AC voltage control than with the d-q current control method. That is because the magnitude of AC voltage modulation wave is directly obtained through the detected voltage error in the AC voltage control scheme, thus the voltage variation can be controlled in a very small limit so that keeping nearly constant voltage magnitude in transient situation. However, as shown in Fig.2.10, in the d-q current control method, the voltage error does not affect the modulation wave directly but take influence to the reactive current i_q through the outer voltage controller, and then make changes on the modulation wave through the inner current control

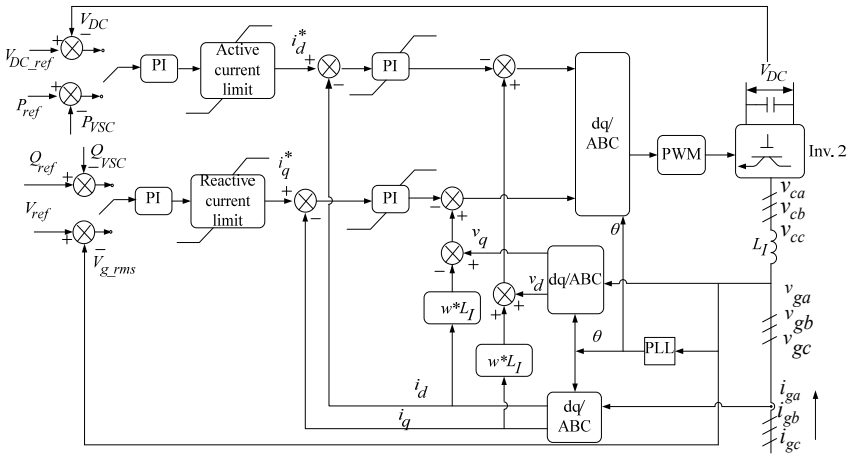

Fig. 2.10. Block diagram of the conventional control on VSC-HVDC converter

loop. Hence a larger equivalent time constant would be needed in the control loop under the vector current control method due to larger numbers of PI controllers.

On the other hand, under the transient situation, a much better performance on active power regulation can be achieved when using the d-q current control method than the AC voltage control scheme. During the system fault at the grid side, the AC current of VSC-HVDC link, i_a, i_b, i_c , would be changed suddenly. Under d-q current control method, the instantaneous variation of the current is introduced into the inner current control loop so as to change the voltage modulation wave, as shown in Fig.2.10. As a consequence, the active power output is controlled around the normal value.

However, under the AC voltage control shown in Fig.2.9, the current during grid fault situation will have a sharp change without the inner current control loop. Since the current variation is not introduced into the control loops, larger amplitude of oscillation on active and reactive power can be found during the transient compared with the situation under d-q current control method. Moreover, as mentioned before, the AC voltage control is not a decoupled control method, which means the control on system voltage takes influence to the regulation on active power and vice visa. That will even aggregate the power fluctuation under the fault transient. Therefore, the AC voltage control on VSC-HVDC may lead to transmission line breakers action on over current and result in cut off of the whole link when the active power oscillation increased large enough.

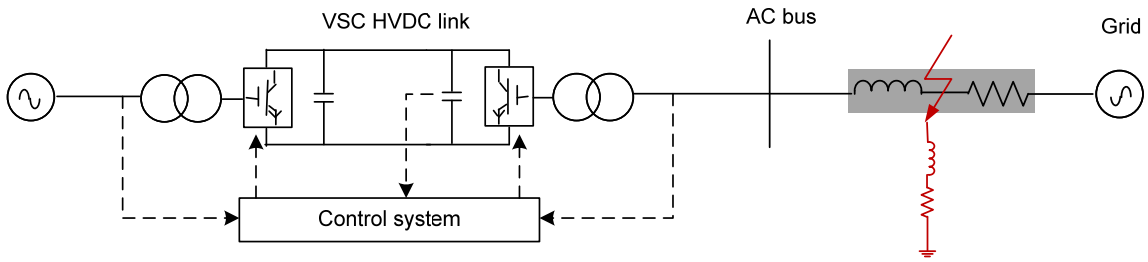

Fig.2.11 Simulation model of the two control methods on the VSC-HVDC link

To verify the analysis above, the two control methods are applied in a VSC-HVDC system model in Fig. 2.11 and simulated in EMTDC/PSCAD. A voltage sag which simulated by the short circuit to ground through a large impedance is adopted at the transmission line that connecting HVDC to the grid on 20s and last about 0.4s, as shown in Fig. 2.11. The simulation results of system voltage, active and reactive power are shown in Fig. 2.12 and 2.13 under the two control methods, respectively.

Compare the result curves in Fig. 2.12 and 2.13, during the disturbance, the AC voltage has a larger fluctuation under the d-q current control, which is due to the non-directly regulation of voltage amplitude in this control method. On the other hand, according to the analysis of power change with different control methods previously, the active and reactive power may suffer different influence from the fault and lead to different oscillation process, which also can be verified in the result waveforms in Fig.2.12 compared with Fig. 2.13.

Note that although the voltage response is faster under the AC voltage control, the difference of the voltage performance is actually quite small when using these two control methods. However the power fluctuation during the disturbance in the system can be found much larger when applying the AC voltage control compared with using the d-q current control. On the basis of that, the d-q current control method is widely adopted on the VSC-HVDC link due to its fast current control loop and the decoupled control characteristic.

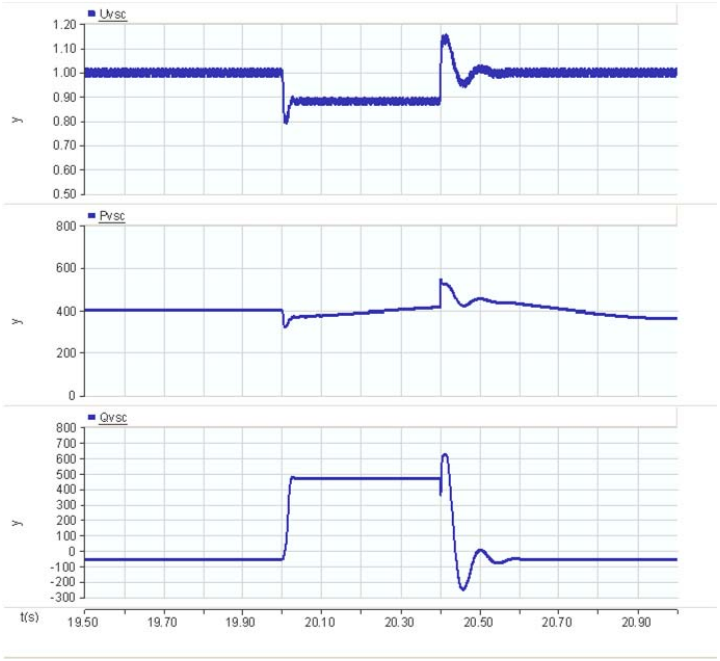

Fig.2.12 Simulation results of system under d-q current control method

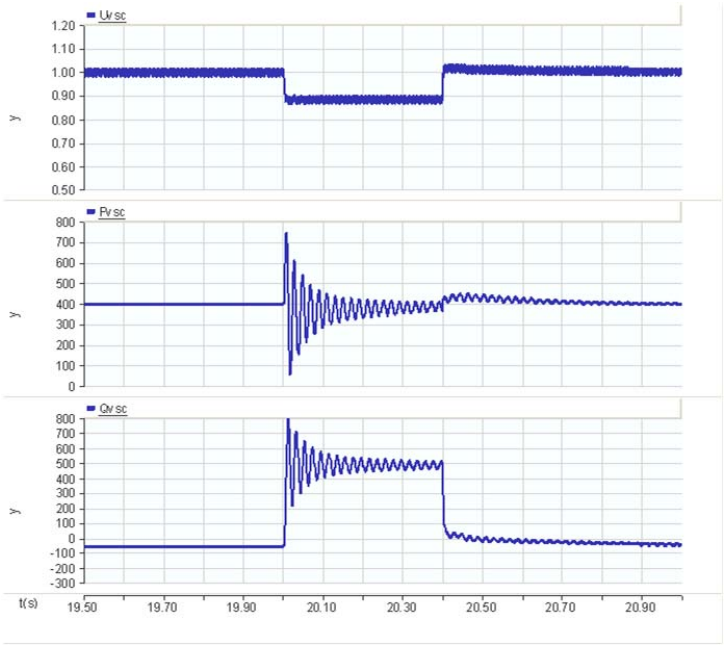

Fig.2.13 Simulation results of system under AC voltage control method

2.5 Power flow of the HMIDC system

For the modeled HMIDC system, the operation status of the system under steady state and grid fault situations can be presented through the power flow analysis shown below.

2.5.1 Steady state operation

The active and reactive power flow in the studied HMIDC system under the steady state is shown in Fig. 2.14.

In the figure, P_1 and P_2 are the active power output from BUS1 and BUS2 to BUS3 and BUS4, respectively.. And Q_1 and Q_2 are the reactive power output from the AC buses to the grid. P_e and Q_e are the power inject into BUS1 from the tie line. P_{LCC} and P_{VSC} are active power delivered by LCC-HVDC and VSC-HVDC links. Q_{LCC} represents the reactive power needed by LCC HVDC link, while Q_{VSC} means the reactive power supplied by the VSC HVDC.

The reactive power at BUS1 then can be described as

$$\boldsymbol{Q_{LCC} = Q_e + Q_c - Q_1 - Q_{L1}} \tag{2.12}$$

Where,

$$\boldsymbol{Q_c = \frac{V_{LCC}^2}{X_c}} \tag{2.13}$$

Where V_{LCC} and V_{VSC} are the RMS value of line-to-line voltage at AC bus of LCC-HVDC link and VSC-HVDC link. δ_1 and δ_2 means the phase angle of V_{LCC} and V_{VSC}. U_G is the RMS value of line-to-line grid voltage and X_1, X_2, X_L are the equivalent reactance of the two AC transmission lines and the tie line between two buses respectively, as shown in Fig.2.14.

Note that the power direction in the Fig. 2.14 is only the reference direction but not the absolute direction of the power flow. The actual flow direction would be determined by the relationship of the voltage magnitudes and phase angles at each bus.

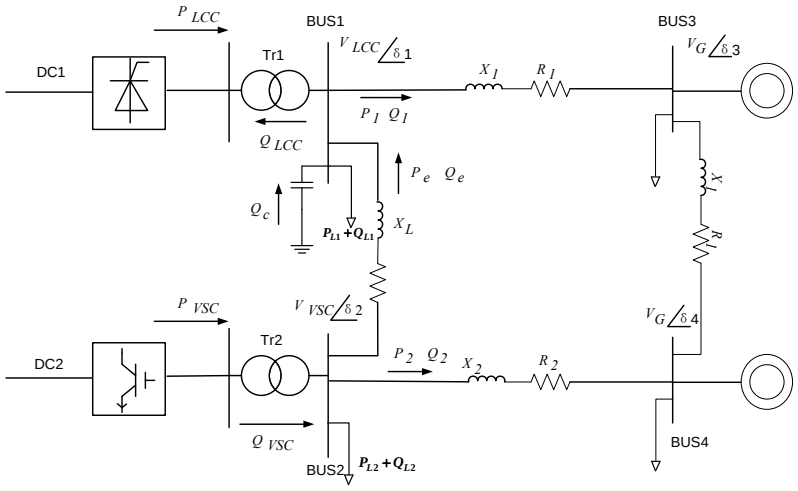

Fig.2.14 System power flow under steady state

2.5.2 Transient state operation

For the transient operation analysis, two types of the grid faults are considered, i.e. the short circuit to ground fault at the transmission line and the voltage sag due to a remote grid fault. In the case of three-phase voltage sag, a large inductive load can be used to emulate the remote grid fault condition. Then the voltage sag occurs at the HMIDC system can be presented by a suddenly connection of an inductive load at BUS1, the power flow in this situation is shown in Fig.2. 15.

Under the voltage sag, in order to restore the ac bus voltage, more reactive power is required in the system. The output reactive power of VSC-HVDC link would be increased due to its voltage control principle. Also the AC system which represented by synchronous generators would support more reactive power to keep the system voltage. Hence the system power flow may be changed from the situation under steady state, as shown in Fig. 2.15.

Note that the different reactive power output of the VSC-HVDC system changes the magnitude and phase angle of its terminal voltage, consequently the active power flow of the system would be different. And the reactive power on BUS1 in the system under this situation can be presented as

$$\boldsymbol{Q_{LCC} + Q_F + Q_1 + Q_{L1} = Q_e + Q_c} \tag{2.14}$$

In the case of three phase short circuit to ground fault, the sudden over current on the transmission line near the fault will lead to the action of protection instruments, i.e. the circuit breakers in this system. Assuming a three-phase-to-ground fault at the transmission line between BUS1 and BUS3, circuit breakers CB1 and CB2 in Fig.2.2 open when the fault occurs, the system structure thus is changed to the emergency situation and the power flow under this case can be depicted in Fig.2.16.

Under the emergency operation mode, since the transmission line between BUS1 and BUS3 is cut off due to the grid fault, the active power transmitted by the LCC-HVDC link has to inject into the system through the tie line between BUS1 and BUS2. On the other hand, the reactive power Q_1 will also disappeared along with the break of the transmission line.

The reactive power equation at BUS1 then is changed in this case and can be shown as

$$\boldsymbol{Q_{LCC} + Q_{L1} = Q_e + Q_c} \tag{2.15}$$

2.6 Summary

In this chapter, the studied HMIDC system model is established based on the possible future western Danish power system. Different from the previous models of the HMIDC system, both the dynamic interactions of the AC grid and the influence of comprehensive loads are considered in this model. The different HVDC links are also modeled together with their conventional control strategies in this chapter. And based on the established HMIDC model, the operation of the system under steady state and grid fault situations are presented through the power flow explanation.

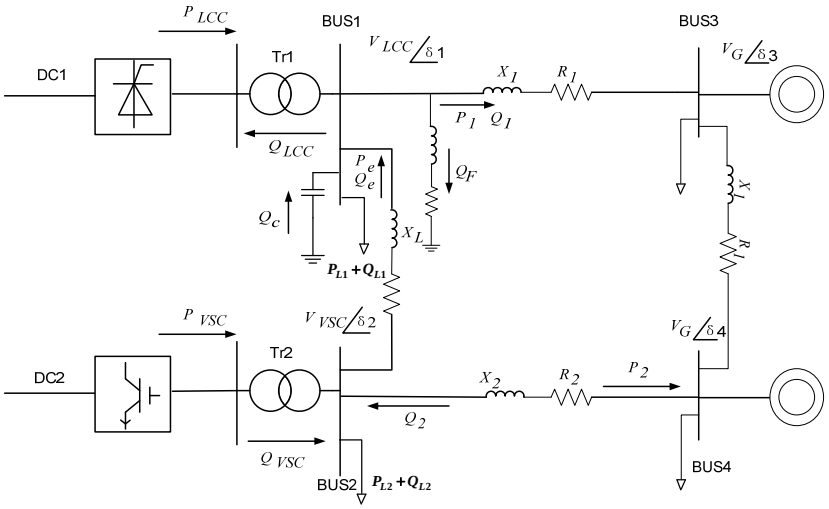

Fig.2.15 System power flow under voltage sag

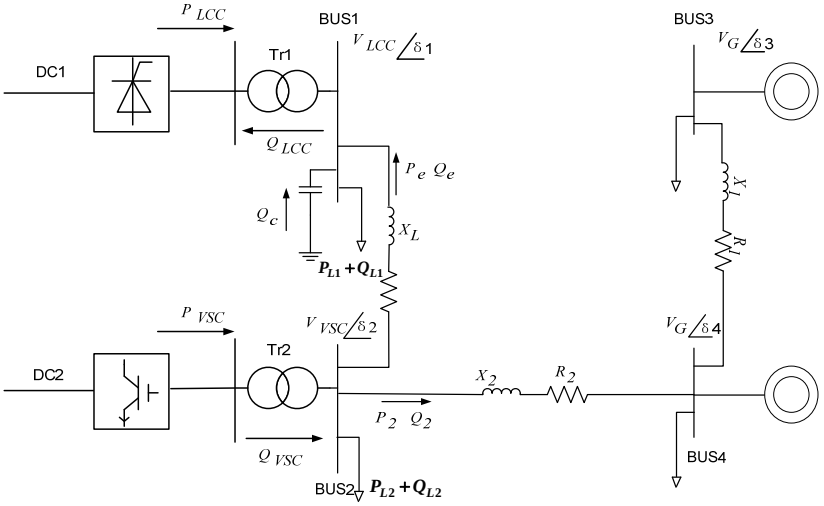

Fig.2.16 System power flow under grid fault

Bibliography:

[1] C. Zhao, and Y. Sun, "Study on control strategies to improve the stability of MULTI-INFEED HVDC systems applying VSC-HVDC," in Proc. IEEE Electrical and Computer Engineering Conf., 2006, pp.2253-2257.

[2] C. Guo, and C. Zhao. "Supply of an Entirely Passive AC Network through a Double-Infeed HVDC System," IEEE Trans. Power Electron., vol. 25, no. 11, pp. 2835- 2841, Nov. 2010.

[3] Q. Zhong, Y. Zhang, L. Lin, et al, "Study of HVDC light for its enhancement of AC/DC interconnected transmission system," in Proc. IEEE PES General Meeting, 2008, pp.1-6.

[4] V. Akhmatov and P. B. Eriksen, "A large wind power system in almost island operation—A Danish case study," IEEE Trans. Power Syst., vol. 22, no. 3, pp. 937–943, Aug. 2007.

[5] P. B. Eriksen, A. Orths, and V. Akhmatov, "Integrating dispersed generation into the Danish power system—Present situation and future prospects, invited panel session paper," in Proc. IEEE General Meeting, Montreal, Canada, Jun. 2006.

[6] www.energinet.dk

[7] IEEE Recommended Practice for Excitation System Models for Power System Stability Studies, IEEE Std. 421.5, Aug. 1992.

[8] Working Group on Prime Mover and Energy Supply Models for System Dynamic Performance Studies, "Dynamic Models for Fossil Fuelled Steam Units on Power System Studies," IEEE Trans. Power Syst., vol. 6, no. 2, pp:753-761, May. 1991.

[9] IEEE Committee Report, "Dynamic models for steam and hydro turbines in power system studies," IEEE Trans. Power App. Syst., vol. PAS-92, pp. 1904–1915, Nov./Dec. 1973.

[10] P. Kundur, Power System Stability and control. New York: McGraw-Hill, Inc. 1994, pp. 271-313.

[11] M. Szechtman, T. Wess, and C.V. Thio, "First benchmark model for HVDC control studies," in Proc. 1991 ELECTRA, pp. 55-73.

[12] R. Li, S. Bozhko, and G. Asher, "Frequency control design for offshore wind farm grid with LCC-HVDC link connection," IEEE Trans. Power Electron., vol. 23, no. 3, pp. 1085–1092, May 2008.

[13] H. Yin, L. Fan, Z. Miao, "Fast Power Routing Through HVDC," IEEE Trans. Power Del., vol. 27, no. 3, pp. 1432–1441, 2012.

[14] K.R. Padiyar, HVDC Power Transmission System-Technology and System Interactions. New Delhi, India: Wiley Eastern Limited, Inc. 1990, pp. 76-96.

[15] C. Du, VSC-HVDC for Industrial Power Systems, Ph.D Thesis, Chalmers University of Technology, Goteborg, Sweden 2007.

[16] G. Asplund, K. Eriksson, and K. Svensson, "DC transmission based on voltage source converters," in Proc. CIGRE SC14 Colloq. South Africa, 1997, pp. 1-7.

[17] A. Timbus, M. Liserre, R. Teodorescu, P. Rodriguez, F. Blaabjerg, "Evaluation of Current Controllers for Distributed Power Generation Systems," IEEE Trans. Power Electron., vol. 24, no.3, pp:654-664. Mar. 2009.

[18] L. Zhang, "Modeling and control of VSC-HVDC links connected to weak AC systems," Ph.D. dissertation, Dept. Electr. Eng., Royal Instit. Technol., Stockholm, Sweden, 2010.

Chapter 3

Voltage stability assessment and indicator of the HMIDC system

3.1 Introduction

For the studied HMIDC system, a lot of factors may take influence to the system voltage stability, such as the system parameters, the power loads and the HVDC links. So far, a comprehensive study on influence factors to the voltage stability of a HMIDC system has not been found in the existing documents. Therefore, in this chapter, the analysis on influence factors to the system voltage stability is firstly presented based on the built system model.

As explained in Chapter 2, the load model in this HMIDC system is a comprehensive model includes the static load and dynamic load. The voltage characteristics of those load models are analyzed in detail in this chapter, so as to present the influences to the system voltage stability by the power loads. Another influence factor to the system voltage stability is the VSC-HVDC link, which can be seen as a controllable reactive power source in the system. This effect from the VSC-HVDC link is also studied in this chapter and verified by the simulation studies. It is noticed that with different AC system parameters, the system voltage stability would also be different. Hence the influences from the system parameters are investigated on the basis of the HMIDC system model.

According to the influence analysis on system voltage stability, in order to assess the system voltage stability more accurately, it is expected that an indicator for presenting the HMIDC system voltage stability can be investigated. On the other hand, although the enhancement of VSC-HVDC link on the voltage stability of a HMIDC system has been studied in the previous literatures [1-3], those influences are only discussed qualitatively. Little information regarding the impacts of the

power capacity and control methods of VSC-HVDC link were presented. There is, consequently, a need to find a quantitative method for the system voltage stability analysis.

The Effective Short Circuit Ratio (ESCR) is known as an important index for the voltage stability assessment of a power system with HVDC links [4]. Therefore, the formulation of ESCR of the HMIDC system is derived in this chapter so that the system voltage stability can be presented by the ESCR values. At the same time, the contribution of the VSC-HVDC link to the system voltage stability can be quantitatively analyzed through the system ESCR.

3.2 Influence factors to system voltage stability

3.2.1 The influence to system voltage stability by the power loads

In power system analysis, voltage stability is also called load stability since the voltage performance is highly dependent on the load characteristics. According to the load characteristic of static load shown in (2.1) and (2.2) in chapter 2, the voltage response of the static load is found dependent on parameters NP and NQ, which also present the influence to the system voltage stability by the static loads. However, the critical influence factor to the system voltage stability from load side would be the dynamic loads, which is modeled by the induction machine in this research. Hence the voltage performance of an induction machine during the fault situation would be the main concern in the system stability study.

Under certain terminal voltage, the relationship between electric torque "T_e" and slip "s" of an induction machine can be drawn as a "T_e-s" curve. The representation of "T_e-s" characteristic can be described as [5].

$$T_e = \frac{3V_1^2 \frac{R_2^{'}}{s}}{\Omega_s \left[\left(R_1 + c\frac{R_2^{'}}{s} \right)^2 + \left(X_{1\sigma} + cX_{2\sigma}^{'} \right)^2 \right]} \tag{3.1}$$

Where, Ω_s is the synchronous speed of the rotating electromagnetic field. V_1 is the terminal voltage of the machine， c is the coefficient and can be derived as 1 approximately, R_1 and $X_{1\sigma}$ are the stator resistance and leakage inductance respectively, R_2' and $X_{2\sigma}'$ are the rotor resistance and leakage inductance referred to the stator side.

According to (3.1), it is obviously that the electrical torque T_e is dependent on V_1 and s. The induction machine "T_e-s" characteristic under different voltage situations can be presented as a group of curves in Fig. 3.1. In this figure, S_m is the slip at which the electrical torque T_e reaches its maximum value [5], and can be presented as

$$s_m = \frac{R_2'}{\sqrt{R_1^2 + \left(X_{1\sigma} + X_{2\sigma}'\right)^2}} \tag{3.2}$$

When the voltage drop occurs at the AC bus of an Induction Machine (IM), the electrical torque of the IM will drops down correspondingly due to the relationship of the terminal voltage and electrical torque shown in (3.1). With different reactive power support from the AC system, the induction machine may performs different operation states: goes back to its original working point or becomes unstable.

Fig. 3.1 shows the possible voltage restore processes of the IM on the basis of the "T_e-s" loci. The original working point of IM is P_n under the rated voltage V_n. The mechanical torque of the induction machine is assumed constant and represented by T_m in Fig. 3.1. T_e is equal to T_m at P_n and rated AC bus voltage V_n. When the voltage suddenly drops, the induction machine operating point falls down from P_n to P_f during the fault. That is because along with the voltage drop, T_e decreases and the imbalance of T_e and T_m reduces the rotor speed, the slip s is thus increased at the same time.

After fault clearance, the bus voltage begins to restore, as well as the electrical torque. During that period, if the electrical torque is still lower than the mechanical torque T_m, the rotor speed would keep decreasing. If the system voltage can be raised high enough, due to which the T_e goes higher than T_m, the rotor speed thus will be increased along with the voltage recovery.

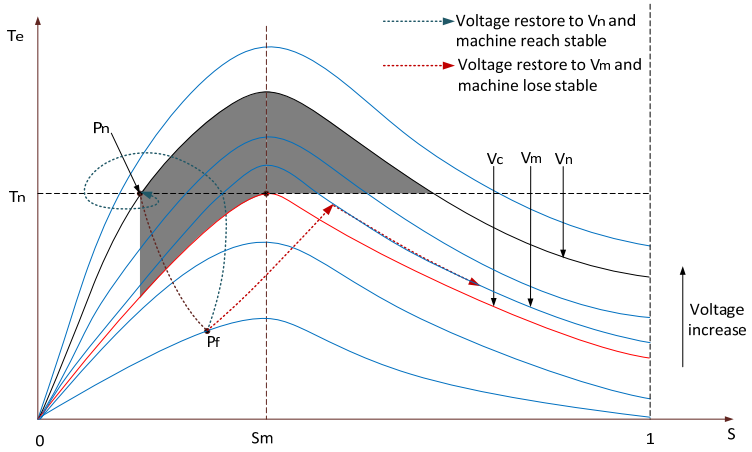

Fig.3.1. Induction machine "T_e-s" characteristic

With enough reactive power support, the voltage can be raised up to original value V_n, and the induction machine operating point goes back to P_n . The blue dotted line in Fig. 3.1 shows an example of "T_e-s" locus under this situation. Limited by the system reactive power support ability, the voltage may not be restored to the rated value in some cases. If the voltage is not high enough for the induction machine to achieve the balance on electrical and mechanical torque, it will lose stability.

For each T_e-s curve in Fig. 3.1, the value of the maximum torque can be found by inserting the expression of slip (3.2) into the torque equation (3.1). The resulting equation for the maximum torque is,

$$T_{emax} = \frac{3V_1^2}{2\Omega_s\left[R_1 + \sqrt{R_1^2 + \left(X_{1\sigma} + X'_{2\sigma}\right)^2}\right]} \tag{3.3}$$

It can be seen from Fig.3.1 that under voltage V_c , the maximum electrical torque is equal to the mechanical torque T_m . Hence if the system voltage cannot return to V_c, the rotor speed will keep going down and consequently the IM becomes unstable. In this situation, the V_c can be calculated from (3.3)

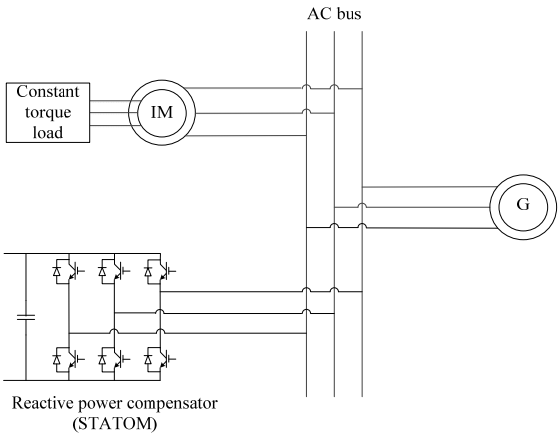

Fig. 3.2 Simple simulation model for the induction motor voltage stability

It should be noticed that although the system voltage increases to a value higher than V_c, the induction machine may still become unstable in some cases. For example, the voltage restores to V_m slowly in Fig. 3.1, V_m is larger than V_c but the rotor speed may keep dropping since T_e always lower than T_m, as a consequence the IM finally loses stability. The "T_e-s" locus under this situation is shown as the red dotted line in Fig. 3.1.

According to the analysis above, it can be found that in order to keep the induction machine stable, the "T_e-s" loci have to firstly enter the area marked in Fig. 3.1 as the blue shadow. In other words, only when the induction machine operation point goes into the marked area, it may achieve steady state after a fault. On the other hand, under some situations the "T_e-s" locus goes into the marked area and out again, in this case the induction machine may still become unstable. Hence the marked area in Fig. 3.1 can be seen as the necessary condition of induction machine voltage stability under the fault.

In order to verify the above analysis and the voltage restoration processed, the simulation study is investigated based on a simple model built in EMTDC/PSCAD. Fig. 3.2 shows the simulation model, which consists of an induction machine, a synchronous generator which represents the grid and reactive power compensation equipment to support system voltage.

In the simulation, a voltage drop which simulated by the short circuit to ground at the AC bus is applied in the system, the fault occurs at 20s and last about 0.2s. With different reactive power

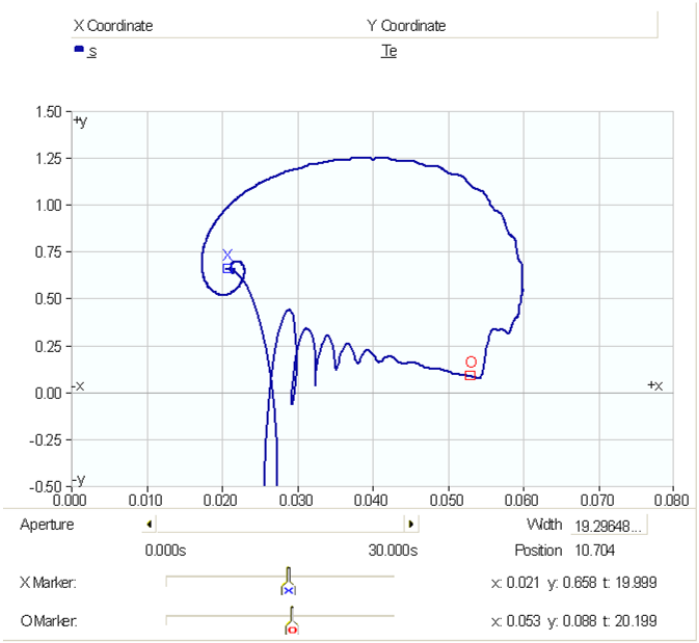

Fig. 3.3 "T_e-s" locus when voltage restore to V_n and machine is stable

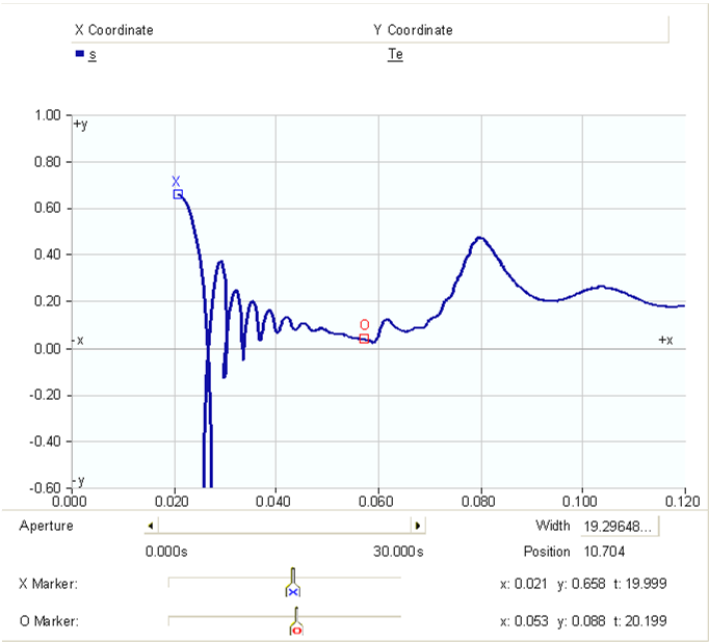

Fig. 3.4 "T_e-s" locus when induction machine lose stable

support from the Static Synchronous Condenser (STATOM), the induction machine may goes back to original state (case 1) or loses stability (case 2). Fig. 3.3 shows the "T_e-s" locus under case 1, in which situation the AC bus voltage restores to the original value V_n. Fig. 3.4 gives the "T_e-s" locus of case 2 and presents that the induction machine becomes unstable. T_e is in p.u. value and the time unit is second in both Fig. 3.3 and Fig.3.4. Substitute (3.2), (3.3) with the induction machine parameters, the maximum slip S_m can be derived as about 0.06s and V_c is approximately 0.44p.u. In Fig. 3.3, the system voltage increases to the original value and obviously "T_e-s" locus goes into presented area in Fig. 3.1, the induction machine then reaches stable again after the fault. In Fig. 3.4, the "T_e-s" locus cannot enter the discussed stable area and induction machine lose stability.

According to the above analysis and simulations, it is easy to know that the voltage recovery process plays an important role to the induction machine stability. The system voltage has to be restored back to the rated value as fast as possible, so as to keep the stabile operation of induction machine.

3.2.2 The influence to system voltage stability by the system parameters

In order to explain the influence of system parameters to the system voltage stability more clearly, the system model in chapter 2 is redrawn here as shown in Fig.3.5. The main system parameters in the HMIDC system are the power rating of generators, capacities of the HVDC links and the distance of transmission lines. For a certain AC grid, the grid short circuit capacity (SCC) is already fixed, thus the generator capacities and the grid impedances which presented by the transmission lines TL1 and TL2 in Fig. 1.2 would be certain values. Therefore, the distance of transmission line TL3 between BUS1 and BUS2 plays the important role in the system voltage stability study.

In the HMIDC system, the infeed point of LCC HVDC link--BUS1 is the relatively weak bus regarding the voltage stability. During a severe grid fault, for example the three phase short circuit at transmission line TL1, the system structure will be changed to the emergency situation, i.e. the TL1 will be cutoff due to the fault, as explained in section 5 of chapter 2. The power flow varies a lot since the system structure is changed. BUS1 thus only connects with the AC grid through the tie line (TL3). As a consequence, the BUS2 plays an important role under this situation.

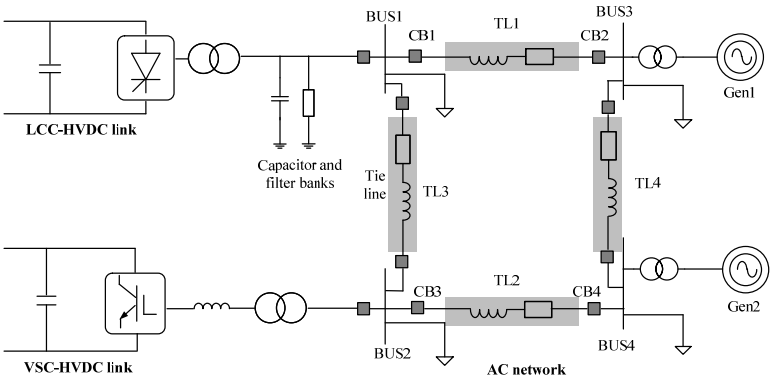

Fig. 3.5. Simplified one-line diagram of the built HMIDC system.

The voltage at BUS1 drops down significantly due to the grid fault, also the DC voltage of LCC-HVDC link. If the voltage at BUS1 cannot be raised up quickly, the circuit breakers (CB1 and CB2) will reclose under a situation that the LCC-HVDC link and the local dynamic load are not yet recovered, which may lead to the power fluctuation in the system and finally result in instability of the induction machine as well as system voltage. Therefore, it is expected that the voltage at BUS1 can be raised up and stabled as soon as possible in order to make sure the LCC-HVDC link and the dynamic load at that bus can go back to normal operation after the breaker reclose.

According to the above analysis, the interactions between the two HVDC links becomes important to the system voltage recovery after fault since it provides the possibilities for a required voltage support to BUS1 from BUS2. It is easy to know that the voltage support from BUS2 to BUS1 during the fault is not only dependent on the voltage at this bus but also rely on the electrical distance of the two buses. Obviously, a relatively weak electrical connection between the two buses cannot achieve the satisfied voltage support ability needed by the system under the severe fault situations.

When the electrical distance of the tie line TL3 is longer, its equivalent impedance goes higher and thus the reactive power consumption on the transmission line is larger for the same voltage support. In that way, the voltage at BUS2 has to be higher enough for realizing the satisfied voltage support to BUS1, otherwise the voltage drop at BUS1 cannot be eliminated after the fault. However, the voltage magnitude of the buses has to be controlled under the limit in case of the over voltage in a power system. Hence for the studied HMIDC system, when the tie line distance is longer than a certain

boundary, the reactive power support from BUS2 to BUS1 cannot help stable the voltage there anymore. And this distance boundary is determined by the capacities of HVDC links, dynamic load proportions as well as the upper limit of the bus voltage in the system.

To verify the analysis above, the simulation study of the HMIDC system has been investigated in EMTDC/PSCAD with the parameters in Table 3.1. Three phase short circuit is applied at the transmission line between BUS1 and BUS3. The breaker1 and breaker 2 in Fig.3.5 opened at 100ms after the fault occurred and then reclosed after 0.6s. Fig.3.6 and Fig.3.7 present the system voltages and the performance of the induction machine at BUS1 during the fault with different electrical distance of tie line. Fig.3.6 gives the simulation results when tie line is about 120 km while Fig.3.7 shows the waves when tie line is changed to180km.

TABLE 3.1
SYSTEM PARAMETERS IN SIMULATION MODEL

Grid parameters				
Frequency		50Hz		
Bus voltage (line-line)		400kV		
Generator capacity		500MVA		
Load value	Load name	Static Load (MVA)	Induction motor capacity(MVA)	Motor load torque(p.u.)
	Load1	120+90j	500	0.7
	Load2	150+60j	400	0.7
	Load3	75+90j	300	0.7
	Load4	75+60j	300	0.7
Transmission line	Between bus1,3	15km		
	Between bus2,4	15km		
	Between bus1,2	100-180km		
	Between bus3,4	360km		

HVDC parameters		
	LCC-HVDC	VSC-HVDC
Capacity	700MVA	500MVA
DC voltage	500kV	300kV

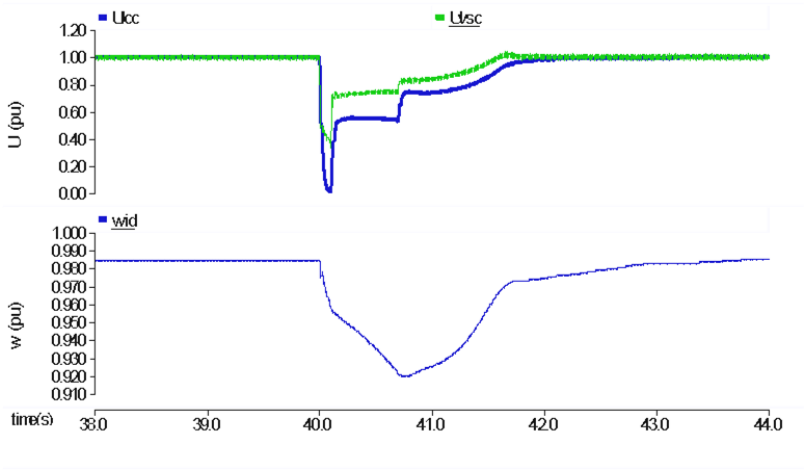

Fig. 3.6 System voltages and rotor speed of IM on BUS 1 when tie line is 120km

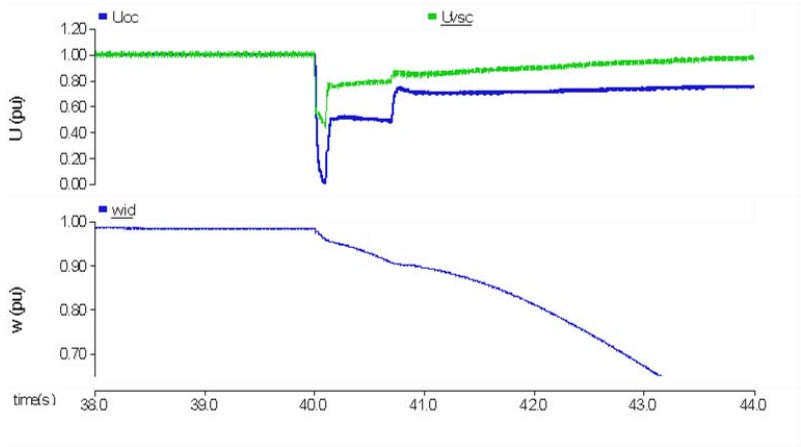

Fig. 3.7 System voltages and rotor speed of IM on BUS 1 when tie line is 180km

With the increase of tie line distance, the contribution of reactive power support from BUS2 to BUS1 is reduced, which means system voltage stability becomes lower. Hence compared with Fig.3.6, the voltage at BUS1 after the fault transient does not go back to stable again in Fig.3.7. And the rotor speed of induction machine at BUS1 reaccelerates after fault when the system has a relatively shorter tie line distance in Fig.3.6, whereas with longer tie line distance the rotor speed keeps dropping and the system loses stability in Fig.3.7.

3.2.3 The influence to system voltage stability by the VSC-HVDC

The voltage stability of the HMIDC system is highly dependent on the reactive power support in the system. There are several reactive sources in the system, such as synchronous generators (Gen 1and Gen 2), capacitor banks at BUS1 and the VSC-HVDC link connected with BUS2. The synchronous generators are normally operates under the certain power factor, which means the reactive power support from the generators is pre-limited according to the power factor. On the other hand, the reactive power output of the capacitor banks is affected by its thermal voltage. Hence under the grid fault situation, the voltage drop at the AC bus will reduce the reactive power of the capacitor banks even below to its rated value.

In this situation, the VSC-HVDC link becomes the important reactive power source in the studied system. Thanks to the flexible power control method of the VSC-HVDC system, it can support the required reactive power to the system to support the system voltage during the fault situation. Fig. 3.8 and Fig.3.9 gives the simulation results of the system voltage and rotor speed of IM at BUS1 during the same grid fault of last section (three phase short circuit to ground) with and without the VSC-HVDC link. The parameters applied in this simulation study are presented in Table 3.1 and the tie line distance is chosen as 100km in this case.

Compare the simulation results in Fig.3.8 and Fig.3.9, after the fault transient, the system cannot go back to stable again without the voltage support of VSC-HVDC link, and thus the rotor speed of induction machine at BUS1 cannot restored after the fault in that situation. The system dynamic response in the simulation study shows that it is easier for the system to lose stability after the disturbance without the VSC-HVDC link.

It is worthy to note that the reactive power support ability of VSC-HVDC link will be affected by its power rating and control methods. During the grid fault situation, the short circuit current is an important indicator for the system stability, which mainly consists of the reactive current. The system voltage stability will be higher when a larger short circuit current can be achieved in the system during the fault. Obviously, with higher capacity of the VSC, the reactive current can be supported by the HVDC link is larger, and thus the system voltage stability would be higher. On the other hand, with different control strategies, the reactive power support ability of the VSC would be different since the short circuit current contribution of the HVDC link to the system would be different.

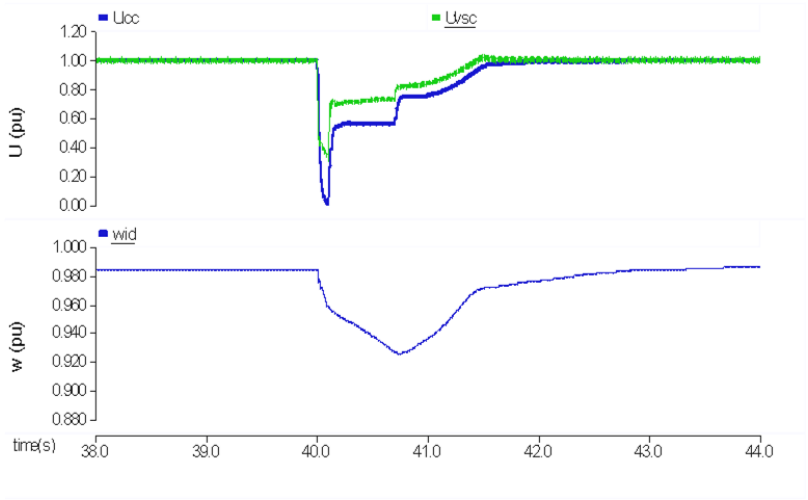

Fig.3.8 System performance with VSC-HVDC link

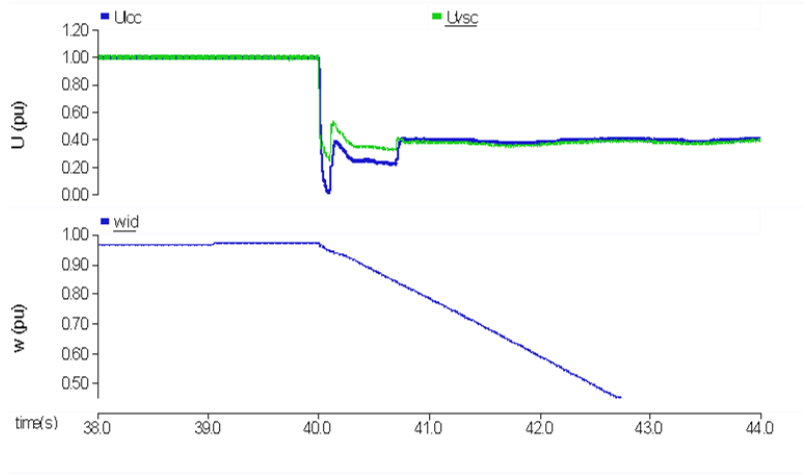

Fig.3.9 system performance without VSC-HVDC link

In view of that, it is expected to develop a quantitative way of presenting the contribution of VSC-HVDC to the system voltage stability instead of the qualitative analysis.

3.3 The voltage stability index in a HMIDC system

Based on the analysis above, there is an urgent need to investigate an assessment index for the HMIDC system in order to achieve the quantitative analysis of the influence to system voltage stability by the different factors, especially by the VSC-HVDC link. The Effective Short Circuit Ratio (ESCR) is known as an important index for the voltage stability assessment of a power system with HVDC links. It is an easy way to assess the system voltage stability when considering the connected HVDC links. The ESCR calculation method of the MIDC system has been well discussed in [6]. However, the specific system structure of the HMIDC system brings the new challenge for the ESCR analysis. The formulation of the ESCR of a HMIDC system and the contribution of VSC-HVDC on the improvement of the ESCR still remain to be clarified. Therefore, the new calculation method of ESCR for the HMIDC system is presented in this section below. The parameters applied in the ESCR calculation is the same with shown in Table 3.1, whereas the load values adopted is different and given in Table 3.2 below.

TABLE 3.2

Load values in the ESCR calculation

Load at BUS1	480MW, 320MVar
Load at BUS2	400MW, 280MVar
Load at BUS3	350MW, 120MVar
Load at BUS4	380MW, 120MVar

3.3.1 Definition of the Effective Short Circuit Ratio

For the power system include HVDC links, especially LCC-HVDC link, the Short Circuit Ratio (SCR) at the HVDC infeed bus would be an important indicator for the system stability. Furthermore, the ESCR which considered the influence of reactive equipment at HVDC terminal may reflect the system stability more accurately. Hence the ESCR is generally deemed as an important index for the strength of an AC system with a HVDC link, which can be simply calculated as [7]:

$$\text{ESCR} = \frac{S_{sc} + S_{scc} - Q_C}{P_{DC}} = \frac{\sqrt{3}V_s I_{sc} + S_{scc} - Q_C}{P_{DC}} \tag{3.4}$$

where S_{sc} and I_{sc} are the short-circuit capacity and the RMS short-circuit current at the commutated bus, respectively. S_{scc} is the synchronous condenser capacity and Q_C is the reactive power generated from the capacitor banks. V_S is the rated rms line-to-line bus voltage, and P_{DC} is the power of HVDC link.

It is known that a higher ESCR value indicates better system voltage stability. On the contrary, with a smaller ESCR value, the system voltage stability is lower, which means a large voltage drop can be found in the system under the fault. That may cause commutation failure on the LCC-HVDC link and even unstable of the system. Normally, when it shows a relatively low ESCR value of the system, some special control technology should be applied to get the satisfied system dynamic performance.

From (3.4), it can be seen that the value of ESCR is dependent on the types of reactive power compensators, which is increased in the case of using the synchronous condensers and reduced in the presence of capacitors. As mentioned in the chapter 2, the capacitors are used to compensate the reactive power needed by the LCC-HVDC link in the studied HMIDC system, which implies the S_{scc} is zero in (3.4). And the Q_C would be approximately 0.6 times of the P_{DC} under the typical value of extinction angle (15^o) in the LCC-HVDC system [8]. Hence, the derivation of the system ESCR in the studied system then depends on the magnitude of short-circuit current I_{sc}.

3.3.2 The equivalent circuit of HMIDC system under short circuit situation

Fig.3.10-Fig.3.12 illustrates the studied system equivalent circuit under a three-phase-to-ground fault at the BUS1. The load models are simply equivalent as constant impedances Z_1~Z_4. The 400 kV transmission lines are represented by the reactance X_1~X_4. It is noted that the synchronous generator can be equivalent as a voltage source in series with its transient reactance for the derivation of short-circuit current [9].

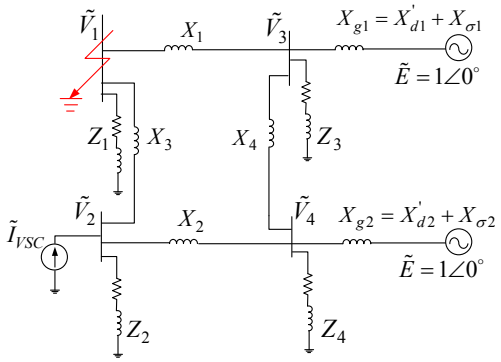

Fig.3.10. Equivalent circuits of the HMIDC system under short-circuit condition.

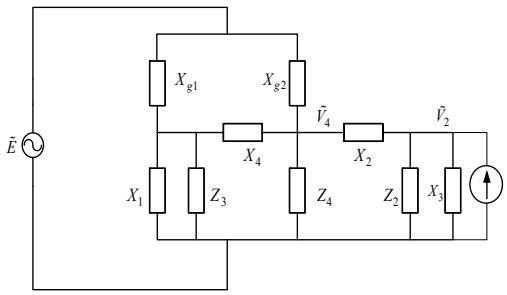

Fig.3.11. Simplified equivalent circuit of Fig.3.10

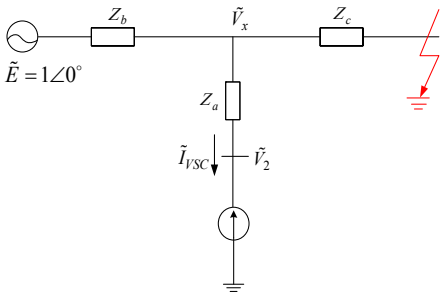

Fig.3.12. Delta-star transformed equivalent circuit.

Since Gen 1 and Gen 2 are equivalent as the same back Electromotive Force (EMF) $\tilde{E}$ in series with their own transient reactance, X'_{d1} and X'_{d2}, respectively. The leakage inductances of the transformers T_{G1} and T_{G2} in Fig. 1 are identified as $X_{\sigma 1}$ and $X_{\sigma 2}$.

Under the short-circuit condition, the voltage and delivered power at BUS2 drops significantly. The power controllers of the VSC are consequently saturated and the current references, i_d^* and i_q^*, reach the limit. Hence, the VSC-HVDC link can be equivalent as the constant current source, where the magnitude and the phase angle of the $\tilde{I}_{VSC}$ depend on the VSC capacity limit and the power control methods. To derive the ESCR at BUS1, the equivalent circuit in Fig. 3.10 is redrawn in Fig. 3.11.

With the help of the delta-star transformation, Fig. 3.11 can be further simplified as shown in Fig. 3.12, and the related parameters are given in Table 3.3. Notice that the system base voltage is 400 kV and the base capacity is 500 MVA.

TABLE 3.3

PARAMETERS OF EQUIVALENT CIRCUIT

Circuit Parameters	**Values**
Transient reactance $X_{d1}^{'}$	0.15 p.u.
Transient reactance $X_{d2}^{'}$	0.13 p.u.
Transformer leakage reactance $X_{\sigma 1}$	0.015 p.u.
Transformer leakage reactance $X_{\sigma 2}$	0.04 p.u.
Transmission line reactance (per km)	0.001 p.u.

3.3.3 Calculation of system ESCR in a HMIDC system

Generally, the current limit of the VSC could be 1.5 times of the rated value. The current output of VSC can be given by

$$\tilde{I}_{VSC} = 1.5 \times \frac{S_{VSC}}{\sqrt{3}V_2}(\cos\varphi + j\sin\varphi) = I_{VSC}\cos\varphi + jI_{VSC}\sin\varphi \tag{3.5}$$

where S_{VSC} is the rated capacity of VSC, V_2 is the rated rms value of the VSC-HVDC infeed bus voltage, and φ is the phase angle of $\tilde{I}_{VSC}$ referred to the back EMF of generators, $\tilde{E}$.

From Fig. 3.12, the short-circuit current at BUS1 can be obtained as

$$\tilde{I}_{sc} = \frac{\tilde{V}_x}{Z_c} = \frac{Z_c\tilde{E} - Z_c Z_b \tilde{I}_{VSC}}{Z_c(Z_c + Z_b)} = \frac{\tilde{E} - Z_b\tilde{I}_{VSC}}{Z_c + Z_b} \tag{3.6}$$

where Z_a, Z_b and Z_c are the delta-star transformations of the circuit constants X_{g1}, X_{g2}, X_1~X_4 and Z_1~Z_4. It is noted that the real parts of the Z_b and Z_c are much smaller compared to the imaginary parts, which consequently can be neglected. Thus, Z_b and Z_c are substituted by their imaginary parts X_b and X_c, respectively. Substituting the X_b, X_c and (3.5) into (3.6), set $\tilde{E}$ equal to 1.0 the magnitude of the short-circuit current $\tilde{I}_{sc}$ can be derived as

$$I_{sc} = \left|\tilde{I}_{sc}\right| = \sqrt{G_m^2 {I_{VSC}}^2 + G_n^2 + 2G_m G_n I_{VSC} sin\varphi} \tag{3.7}$$

where G_m and G_n are

$$\begin{cases} G_m = \dfrac{X_b}{X_c + X_b} \\ G_n = \dfrac{1}{X_c + X_b} \end{cases} \tag{3.8}$$

Substituting (3.7) into (3.4), and the S_{scc} should be zero in the studied system, the ESCR at BUS1 is derived as

$$\text{ESCR} = \frac{\sqrt{3}V_s\sqrt{G_m^2 {I_{VSC}}^2 + G_n^2 + 2G_m G_n I_{VSC} sin\varphi} - 0.6P_{DC}}{P_{DC}} \tag{3.9}$$

3.4 Enhancement of ESCR by VSC-HVDC

According to the ESCR equation in (3.9), both the system parameters and VSC-HVDC link take influence to the system ESCR value.From (3.9), it is found that the ESCR is dependent on the magnitude and phase angle of the output current of the VSC-HVDC link, I_{VSC} and φ, in addition to other circuit parameters. Fig. 3.13 depicts the ESCR variations with the changes of I_{VSC} (from 0 p.u. to

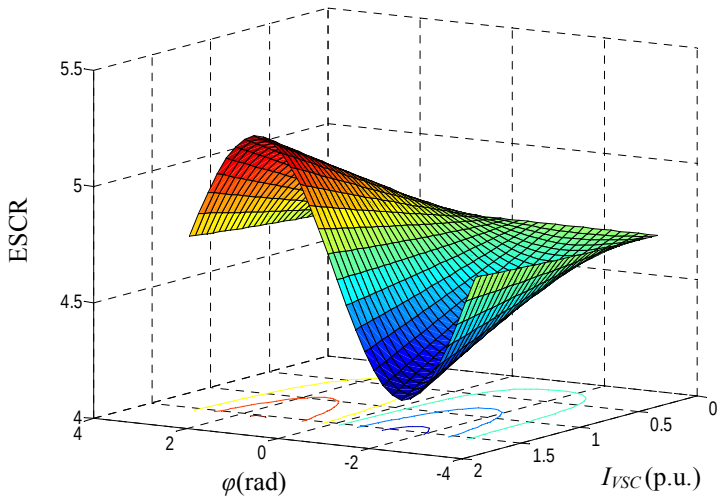

Fig. 3.13 The relationship between ESCR and the current vector $\tilde{I}_{VSC}$

2 p.u.) and φ (from - π to π). Since the G_m and G_n are positive, the system ESCR can be enhanced through the increase of I_{VSC}. Under the certain VSC-HVDC capacity, i.e. certain I_{VSC}, the ESCR reaches the minimum and maximum values at φ=-π/2 and φ=π/2, respectively.

Note that the vector current control of VSC-HVDC link is oriented to the voltage vector at BUS2, $\tilde{V}_2$, whereas the phase angle φ is referred to the back EMF of the generator, $\tilde{E}$. Hence, to quantitatively analyze the enhancement of ESCR by VSC-HVDC link, the phase shift between the voltage at BUS2 and the generator back EMF needs to be identified under short-circuit condition. From Fig. 3.12, the voltage vector $\tilde{V}_2$ can be obtained by

$$\tilde{V}_2 = \frac{|Z_x|}{(X_c + X_b)} I_{VSC} \angle(\varphi + \theta + \frac{\pi}{2}) + \frac{X_c E}{X_c + X_b} \tag{3.10}$$

where Z_x can be expressed as

$$Z_x = (X_c + X_b) Z_a + X_c X_b = |Z_x| \angle \theta \tag{3.11}$$

where the θ is the phase angle of Z_x referred to $\tilde{E}$. Based on the parameters in Table 3.1-Table 3.3 (the

tie line distance is chosen as 100km in Table 3.1), the voltage vector $\tilde{V}_2$ is

$$\tilde{V}_2 = 0.06\angle(\varphi + \theta + \frac{\pi}{2}) + 0.204\angle 0 \tag{3.12}$$

It is shown that the former part of $\tilde{V}_2$ is much smaller than the latter in (3.12), hence no matter how much the angle value φ and θ are, the phase angle of $\tilde{V}_2$ can be seen as almost 0 and in phase with $\tilde{E}$. Therefore, the phase angle φ of $\tilde{I}_{VSC}$ referred to $\tilde{E}$ can be equivalent as the angle between $\tilde{I}_{VSC}$ and $\tilde{V}_2$.

Furthermore, since $\tilde{I}_{VSC}$ can be decomposed into i_d^* and i_q^* in the rotating reference frame, the outer power control loop that yields i_d^* and i_q^* determines the extent of ESCR enhancement of VSC-HVDC link. Traditionally, the i_d^* and i_q^* are subjected to the limit of the outer power controllers, such that the phase angle φ and the consequent ESCR are constrained as certain values. Hence, it is needed to develop a proper power control method to enhance the ESCR to a maximum extent within the VSC power capacity.

3.5 Validation of the calculation method on ESCR and short circuit current

To validate the calculation method of the system ESCR, the simulation studies on the HMIDC system shown in Fig. 3.1 are conducted in PSCAD/EMTDC. The system parameters are summarized in Table 3.2. And the following initial operating conditions are assumed in the case studies.

1) The synchronous generators (Gen1 and Gen2) deliver 0.75 p.u. active power, respectively, to the transmission system.
2) The voltage magnitudes at the terminals of generators are set as 1.05 p.u, respectively.
3) The VSC-HVDC and the LCC-HVDC deliver 0.8 p.u. power (P_{VSC}) and 0.7p.u. power (P_{LCC}) to the AC system, respectively.
4) The VSC current limit is 1.5 times of the rated current.

Fig. 3.14 shows the simulation results of system symmetrical short circuit current [10], when the three-phase-to-ground fault appears at BUS1. Notice that the current peaks during the first line frequency period is the sub-transient fault currents, while the short circuit currents used for the ESCR

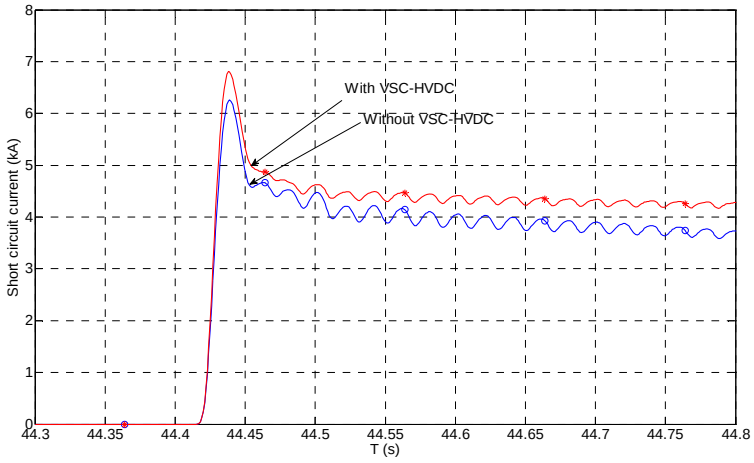

Fig.3.14 System short circuit current on BUS1 with different situations.

calculation ($|\tilde{I}_{SC}|$) is the transient fault current values as marked in Fig. 3.14.

In the case of without the VSC-HVDC link, based on the system parameters shown in Table 3.1 and Table 3.2, the short circuit current $|\tilde{I}_{SC}|$ and the system ESCR can be derived from (3.7) and (3.9) as 4.6 kA and 4.27, respectively. Compared with the blue curve shown in Fig. 3.14, it can be seen that the theoretical analysis matches well with the time-domain simulation result.

When applying the VSC-HVDC link with the conventional control method in the system, the active and reactive currents of VSC reach to their own limits, which are assumed as i_d = 1.3 p.u., i_q = 0.75 p.u.in this case. Then, substituting them into (3.7) and (3.9), the $|\tilde{I}_{SC}|$ is 4.99kA and the ESCR is obtained as 4.67, which are verified by the red curve in Fig. 3.14.

3.6 Summary

The ESCR of studied HMIDC system is derived and calculated with an equivalent circuit method in this Chapter. Based on analysis of system short circuit current, the equivalent circuit of the HMIDC system during short circuit transient is obtained. According to this equivalent circuit, system ESCR is calculated through Thevenin equivalent method. As a consequence, a method of quantitatively

evaluating the improvement of system voltage stability by a VSC-HVDC link can be obtained. Simulation studies verified the changes of system stability corresponding to the calculated ESCR values under different cases with and without VSC-HVDC link.

Bibliography:

[1] C. Zhao, and Y. Sun, “Study on control strategies to improve the stability of MULTI-INFEED HVDC systems applying VSC-HVDC,” in Proc. IEEE Electrical and Computer Engineering Conf., 2006, pp.2253-2257.

[2] C. Guo, and C. Zhao. “Supply of an Entirely Passive AC Network through a Double-Infeed HVDC System,” IEEE Trans. Power Electron., vol. 25, no. 11, pp. 2835- 2841, Nov. 2010.

[3] Q. Zhong, Y. Zhang, L. Lin, et al, “Study of HVDC light for its enhancement of AC/DC interconnected transmission system,” in Proc. IEEE PES General Meeting, 2008, pp.1-6.

[4] D.L.H. Aik, and G. Andersson, “Power stability analysis of multi-infeed HVDC systems,” IEEE Trans. Power Del., vol. 13, no. 3, pp. 923-931, Jul. 1998.

[5] S.J. Chapman, "Electric machinery fundamentals, " 4th ed., New York: McGraw-Hill, Inc. International Edition 2005, pp. 405-415.

[6] J. B. Davies, I. T. Fernando, K. L. Kent, E. K. Bard, K. H. Sobrink, “HVDC Multiinfeed Considerations in Norway and Denmark,” in Proc. Cigre SC B4 Colloq., Norway, 2009.

[7] C. W. Taylor, Power system voltage stability, McGraw-Hill, Inc. International Editions, 1994, pp. 181-202.

[8] K. R. Padiyar, HVDC Power Transmission systems-Technology and system interactions, New Delhi, India: Wiley Eastem Limited, 1990, pp. 130-144.

[9] B. M. weedy, B. J. Cory, Electric Power systems, 4th Edition, 1998.

[10] Short-Circuit Currents in Three-Phase A.C. Systems, IEC Int. Std. 60909-3 Ed. II, 2003.

Chapter 4

Power control method on VSC-HVDC link to enhance system voltage stability

4.1 Introduction

Based on the analysis and calculation of system ESCR in last Chapter, it is noted that the ESCR of the HMIDC system is highly influenced by the current output of VSC-HVDC during the short circuit situation. The current magnitude is determined by the capacity of the VSC-HVDC link, whereas the phase angle of the current will be different due to the different control methods. In that way, the control method of the VSC-HVDC link has an important effect on the enhancement of system ESCR.

In the previous literatures, several control approaches have been reported to allow the VSC-HVDC system to generate a certain amount of reactive power under the grid voltage drops [1]-[3]. However, most of them assumed that the reactive current reference is under a pre-set limit, which restricts the voltage support capability, especially during the severe voltage drops [4]. Hence, it is important to develop a proper control scheme for the VSC-HVDC link, in order to dynamically adjust the output reactive power under different voltage drops.

In view of that, in this Chapter, a flexible power control method of the VSC-HVDC link is proposed according to the quantitative analysis of system ESCR. Different from the conventional control method, in the proposed control strategy, the active current reference is dynamically adjusted based on the output of the AC voltage controller. Thus, the maximum use of reactive power support capability of the VSC-HVDC link can be realized.

In addition, considering the influence to system stability by the fault at sending end of VSC-HVDC link, an operation mode switch is designed in the proposed control system, so as to ride through the sending end voltage drop.

To verify the proposed control method, the case studies of the built HMIDC system under the different grid fault conditions are performed in PSCAD/EMTDC. The system performance in each case is simulated under the different control methods. And the enhancement to the system voltage stability by the proposed control strategy can be verified through the simulation results.

4.2 The limitation on voltage support ability of the conventional control method based on ESCR analysis

As explained in Chapter 2, the control strategy of the VSC-HVDC link is conventionally designed based on the vector current control method (d-q current control) shown in Fig.2.11. For the voltage stability of the AC system, the control method on the receiving-end converter (REC) of VSC-HVDC link would be more important since it may take large influence to the voltage support ability from the VSC-HVDC to the AC grid.

According to the block diagram of the control method in Fig.2.11, under the conventional control method, DC voltage of VSC-HVDC link is normally controlled by the REC and the active power is controlled by the sending-end converter (SEC). On the other hand, in order to get higher voltage support ability, the ac voltage is controlled in the reactive power control loop in the REC of the VSC-HVDC link.

Fig.4.1 shows the block diagram of the conventional control method on REC of the VSC-HVDC system. According to the control principles, to prevent the VSC-HVDC from the over-current trip, the current references are generally limited at the output of power control loop, as shown in Fig. 4.1. The maximum current of the converter are generally chosen as 1.5 times of the rated value. Hence the current reference limit of VSC is defined as:

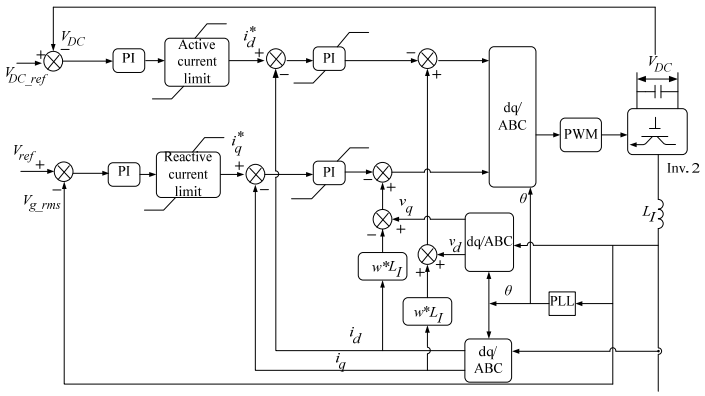

Fig.4.1 Block diagram of the conventional control method on REC

$$i_{\lim}^* = 1.5 i_{rated} \tag{4.1}$$

where i_{rated} is the rated current of VSC-HVDC. The current limit i_{lim}^* comprises an active current limit and a reactive current limit, which can be given by:

$$i_{\lim}^* = \sqrt{{i_{d\lim}^*}^2 + {i_{q\lim}^*}^2} \tag{4.2}$$

where i_{dlim}^* and i_{qlim}^* are the active and reactive current limits, and the choice of them depends on the application.

Under the short-circuit condition in Chapter 3, the VSC current vector $\tilde{I}_{VSC}$ can be obtained by the current limits, i_{dlim}^* and i_{qlim}^*, which thus has an important effect on the system ESCR. With the different pre-setting limits i_{dlim}^* and i_{qlim}^*, the magnitude of $\tilde{I}_{VSC}$ is fixed as i_{lim}^* due to (4.2), whereas the phase angle φ can be different so that the enhancement of system ESCR by the VSC-HVDC link is different.

Fig. 4.2 shows the current controller margins of the VSC and the different current vector $\tilde{I}_{VSC}$ when changing the limit set-points, i.e. i_{dlim}^* and i_{qlim}^*. Three different current limit set-points corresponding to the three operating scenarios are chosen in Fig. 4.2 as follows:

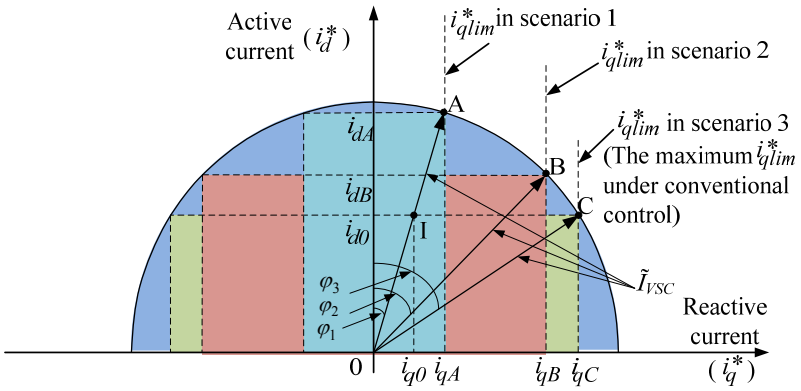

Fig.4.2 Current control margin and current vector of receiving end VSC

1) The limit set-point is set at the point A, where the power factor is kept equal to the value at the initial operating point, I.
2) The limit set point is set at the point B, where the i_{dlim}^* and i_{qlim}^* have the same value.
3) The limit set point is set at the point C, where the current margin of VSC is only given to the reactive current.

It is worthy to mention that the limit i_{dlim}^* has to be equal or higher than the rated active current i_{rated}, in order to guarantee the active power transmission at steady state. Thus the reactive current limit in the scenario 3) reaches its maximum value as

$$i_{q\lim\_Max}^* = \sqrt{{i_{\lim}^*}^2 - {i_{rated}}^2} = 1.12 i_{rated} \tag{4.3}$$

With the different current limits, the current references are limited in the different shaded areas, as shown in Fig. 4.2, which can be seen as the current controller margin of VSC. Under the short circuit situation (see Fig. 3.10), the locus of the current reference is driven to the current limit point, 'A' 'B' or 'C', thus the current vector $\tilde{I}_{VSC}$ in three scenarios can be obtained in Fig. 4.2. The relationship between the phase angles of these current vectors can be given by

$$\varphi_1 < \varphi_2 < \varphi_3 < \pi/2 \tag{4.4}$$

As a consequence, from (8) it is known that the ESCR values of the HMIDC system in these three scenarios are

$$ESCR_1 < ESCR_2 < ESCR_3 \tag{4.5}$$

It can be concluded that the pre-set limit of the VSC-HVDC restricts the current phase angle φ in the conventional control method, which consequently limits the enhancement of the system ESCR. Hence, it is needed to develop proper control methods so that the maximum system ESCR can be obtained within the capacity of VSC-HVDC link.

4.3 Proposed power control method of VSC-HVDC to enhance AC system voltage stability

From the above analysis, it is known that the ESCR of the HMIDC system reaches the maximum value when the phase angle between the output current of VSC and the grid voltage, is equal to $\pi/2$. In light of this, instead of pre-setting the output limits in the outer power controllers, a flexible power control method for the VSC-HVDC link is proposed, which allows the phase angle to dynamically approach to $\pi/2$ under the grid voltage drops.

Fig. 4.3 depicts the block diagram of the proposed control method for the VSC-HVDC system. In the approach, a multi-layer control scheme is employed, which includes 1) the inner vector-current controller for the independent control of active power and reactive power, 2) the intermediate adaptive current limiter for realizing maximum reactive power support under the voltage drops of the infeed grid, and 3) the AC voltage as well as active power controllers. Furthermore, to ride-through the grid faults at the sending-end grid, an improved active power control loop is developed. Notice that although only the receiving-end converter of VSC-HVDC is discussed here, the sending-end converter has the same control structure.

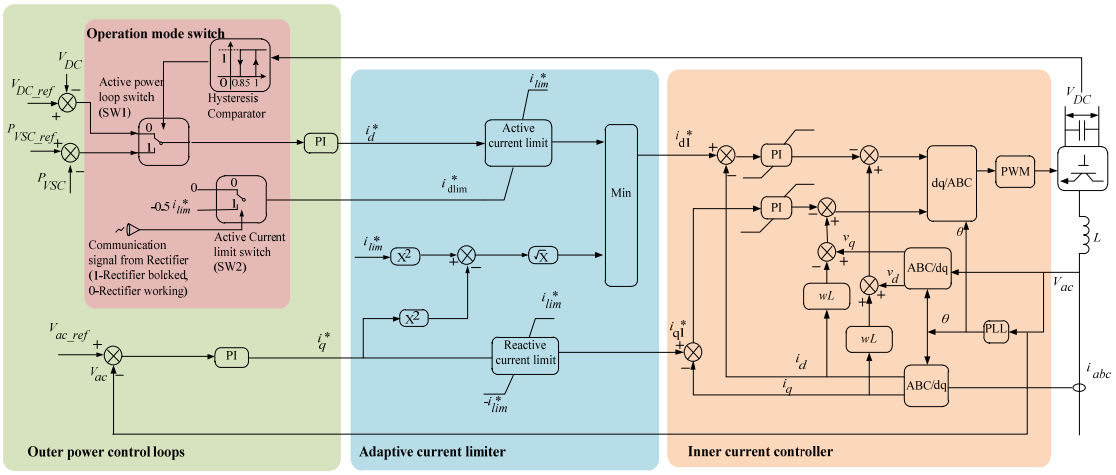

Fig. 4.3. Block diagram of proposed control method of the VSC-HVDC link at the receiving end.

4.3.1 Adaptive Current Limiter

To overcome the drawback of the pre-setting current limit at the outputs of power controllers, an adaptive current limiter is developed. The idea behind this approach is to dynamically adjust the active current reference according to the change of reactive current reference for restoring the grid voltage during system faults.

The operation principle of the adaptive current limiter can be expressed as follows

$$i_{q1}^{*}=\begin{cases} i_{q}^{*} & ,\ -i_{\lim}^{*}<i_{q}^{*}<i_{\lim}^{*} \\ i_{\lim}^{*} & ,\ i_{q}^{*}\geq i_{\lim}^{*} \\ -i_{\lim}^{*} & ,\ i_{q}^{*}\leq -i_{\lim}^{*} \end{cases} \tag{4.6}$$

$$i_{d1}^{*}=\begin{cases} i_{d}^{*} & ,\ i_{d\,\lim}^{*}<i_{d}^{*}\leq\sqrt{i_{\lim}^{*\,2}-i_{q}^{*2}} \\ \sqrt{i_{\lim}^{*\,2}-i_{q}^{*2}} & ,\ \sqrt{i_{\lim}^{*\,2}-i_{q}^{*2}}<i_{d}^{*}<i_{\lim}^{*} \\ i_{\lim}^{*} & ,\ i_{d}^{*}\geq i_{\lim}^{*} \\ i_{d\,\lim}^{*} & ,\ i_{d}^{*}\leq i_{d\,\lim}^{*} \end{cases} \tag{4.7}$$

where i_d^* and i_q^* are the current signals generated by the outer power control loops. i_{d1}^* and i_{q1}^* are the actual current references regulated by the adaptive current limiter. i_{lim}^* is the VSC current limit defined in (4.1) and i_{dlim}^* is the lower limit of active current coming from active power control loop.

According to (4.6) and (4.7), the current trajectory of i_{d1}^* and i_{q1}^* under the grid voltage drops can be illustrated in Fig. 4.4. Assuming that the VSC-HVDC system operates at the steady-state point, I. With small grid voltage disturbances, the current references generated from the outer power control loops is still inside the circle shown in Fig. 4.4. Thus, the system achieves a new stable operation point, M, where the current references i_{d1}^* and i_{q1}^* remain equal to i_d^* and i_q^*, respectively.

On the other hand, under a severe voltage drop, large imbalances between the active power and ac voltage arise, which tends to increase current signals i_d^* and i_q^* significantly. Once the current signals reach the VSC current limit, i.e. $i_d^{*2} + i_q^{*2} = i_{lim}^{*2}$, the adaptive current limiter changes the active current reference i_{d1}^* as equal to $\sqrt{i_{\lim}^{*\,2} - i_q^{*2}}$ base on (4.7) instead of the i_d^*, which indicates that the current reference vector rotates in clockwise along the current limit circle, as shown in Fig. 4.4.

Depending on the fault condition, the current reference vector tends to reach at a new stabile operation point N, or continues to rotate until point D where the current phase angle φ is $\pi/2$ and the whole power capacity of the VSC is utilized for the reactive power support.

Fig. 4.5 shows the VSC capability circle under different AC voltages. Under the certain operation mode, the active power transmission by the VSC-HVDC link is unidirectional. Hence, the VSC capacity circle is drawn in two quadrants. With the various voltage drops, the capability circle shrinks differently. Notice that the steady-state operating point should always be inside the capacity circle, take the point I for example. Under a voltage drop, the output power of VSC drops to the point, F, inside a smaller circle. And the current vector reference meets its limit rapidly.

With the conventional control method, the reactive current reference is limited to be lower than $1.12 i_{rated}$, as shown in (4.3). In contrast, the reactive current reference i_{q1}^* can be increased to i_{lim}^* with the adaptive current limiter. The different reactive current limits result in different voltage restoration, as shown in Fig. 4.5. The lower restored voltage in turn leads to a smaller capacity of VSC, which is

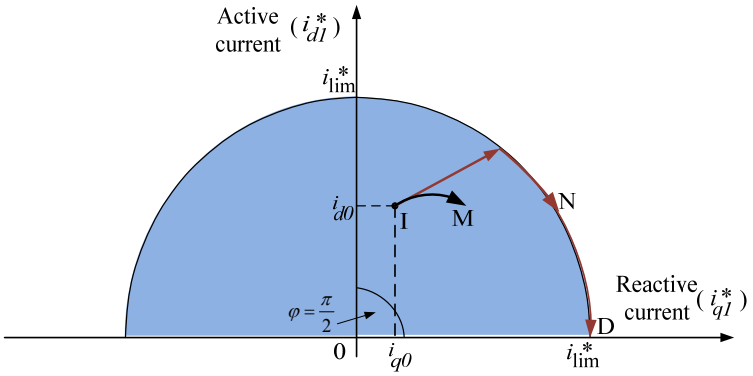

Fig. 4.4. Current trajectory with the regulation of adaptive current limiter

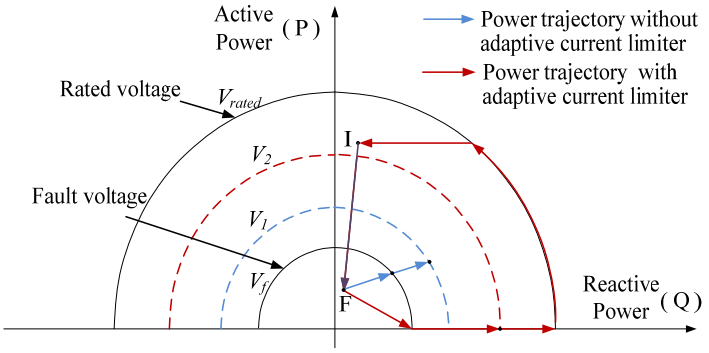

Fig. 4.5. Capability curve of VSC under voltage drop

more difficult for a further voltage recovery, and the infeed system tends to become unstable with the conventional control method.

4.3.2 Operation mode switch

Considering the impact of the sending-end grid fault on the stability of the VSC-HVDC system, an operation mode switch controller is developed in the active power control loop, as highlighted in Fig. 4.3. This method employs a hysteresis-based active power loop switch (SW1) and an active current limit switch (SW2).

Depending on the system conditions, three operation modes are available for the VSC-HVDC link, which are chosen by the operation mode switch. Table 4.1 gives the operation modes and corresponding switch states under different system conditions. Notice that in all the operation modes, AC voltage control is applied in power control loops of VSCs at both sides of VSC-HVDC link to keep the grid voltage constant.

During the steady-state operation, SW1 = SW2 = 0, and the active power control is applied at the receiving-end VSC. The lower limit of the active current, i_{dlim}^{*}, is set as zero to prevent inverse active power, as shown in Fig. 4.3. In the presence of the sending-end voltage drops, the active power transmission by the VSC-HVDC link is limited, and the DC voltage drops down rapidly, due to the loss of DC voltage control capability at the sending-end converter. Thus, to prevent the DC voltage from collapse, SW1 is set to 1 through a hysteresis comparator once the DC voltage drops down lower than the 0.9 p.u. And consequently, the DC voltage is regulated at the receiving-end converter, which decreases the output active power rapidly.

If the fault is temporary and be cleared in a short period, along with the recovery of active power injected into VSC-HVDC link, the DC voltage is restored. Once the DC voltage is higher than the rated value, the SW1 will be set to zero and the power control loop changes back to the pre-event situation.

TABLE 4.1

Operation modes and switch states

SW1	SW2	Operation mode	System condition (event)
0	0	Active power control at Inverter; DC voltage control at Rectifier.	Under steady stated or infeed grid fault.
1	0	DC voltage control at Inverter; Active power control at Rectifier.	Under sending end grid fault.
1	1	Rectifier blocked and rest of the VSC-HVDC is controlled as a STATOM.	Under the severe permanent fault at the output terminal of the rectifier.

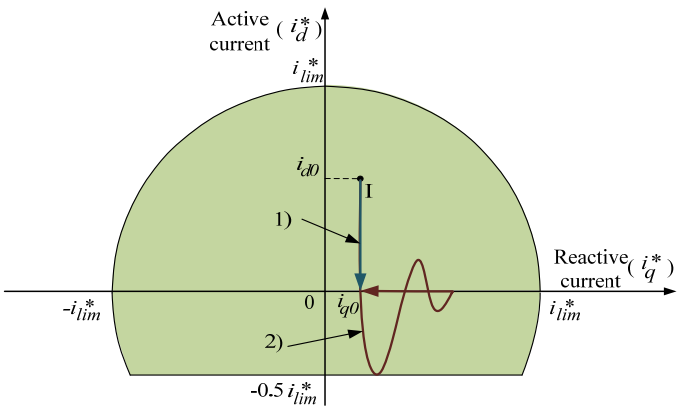

Fig. 4.6. Current reference trajectory of VSC in the presence of permanent fault at sending end grid.

On the other hand, if the fault is severe and occurred at the output terminal of rectifier, the sending-end converter should be blocked to isolate the fault. In this case, the SW2 is set as 1 through the communication signal form the sending-end and the i_{dlim}^* becomes lower than zero. Thus, the receiving-end VSC operates like a STATCOM to stabilize the infeed system voltage. The DC voltage is kept constant by the inverse active current. It is noted that the lower limit of active current i_{dlim}^* is designed based on the expected restoring speed of DC voltage, which is chosen as -0.5 i_{lim}^*.

Fig. 4.6 shows the current controller margin and the current reference trajectory of the receiving-end VSC during the permanent fault at the sending-end grid. The trajectory can be divided into two parts: 1) the i_d^* first drops down quickly to maintain the DC voltage by setting SW1 as 1, and then 2) the sending-end converter is blocked, the i_{dlim}^* is changed to be -0.5 i_{lim}^*. The output current of VSC-HVDC becomes pure reactive current after a short transient.

4.3.3 Impact of Adaptive Current Limiter on Active Power Delivery

It is noted that to realize the maximum voltage support by the VSC-HVDC under a severe grid voltage drop, the adaptive current limiter reduces the active current reference to release the current control margin for reactive current reference. Thus, it is needed to first evaluate the infeed AC system response through case studies before using the proposed control method for the VSC-HVDC link.

However, the frequency deviation brought by the proposed control method is usually small and

decays in a short period. Take the studied system for example, the frequency fluctuations shown in Section VI is within the grid code, due to the following reasons:

1) The active power imbalance in the infeed AC system is low, since both the output active power of VSC-HVDC link and active power demand from the load are reduced under the voltage drop. Thus, a further active power reduction by the adaptive current limiter on this basis will not result in large system frequency deviation.
2) Furthermore, the active power reduction of the VSC-HVDC link is a transient phenomenon. During the transient, the inertia energy stored in the rotating mass of the infeed system maintains the system frequency within the reasonable limit.

On the other hand, in the studied system, with the reduction of active power delivery by the VSC-HVDC link, the frequency of the sending-end grid tends to increase. It is worthy to mention that the power system with HVDC links is normally designed with a certain tolerance of frequency deviation, particularly in the cases of emergency power change in HVDC systems or the grid faults at the other side of HVDC links [5]. Therefore, the small frequency fluctuation at the sending-end grid does not bring additional stability problems.

4.4 Simulation studies

To validate the performance of the proposed power control method, case studies on the HMIDC system are conducted in PSCAD/EMTDC. The system parameters adopted in the simulation study are the same as applied in the ESCR calculation in chapter 3 (Table 3.1-Table 3.3). And the induction motor load parameters used here are given in Table 4.2 below. The initial operating conditions assumed in the case studies are also the same as that explained in section 3.5 of chapter 3.

4.4.1 Validation of the ESCR Calculation

In the last chapter, the simulation results of system symmetrical short circuit current under the three-phase-to-ground fault at BUS1 when the system with and without the VSC-HVDC link have been given in Fig. 3.14. It shows that with the VSC-HVDC link, system short circuit current has been increased due to the reactive power support ability of VSC. Nevertheless, from the analysis of the

TABLE 4.2

PARAMETERS OF DYNAMIC LOADS

Parameters	**Induction motor I**	**Induction motor II**
Location	BUS1	BUS2
MVA	500	500
Percentage in local load	75%	60%
Mechanical torque	0.7p.u.	0.6p.u.
Inertia	3.412 s	3.412 s

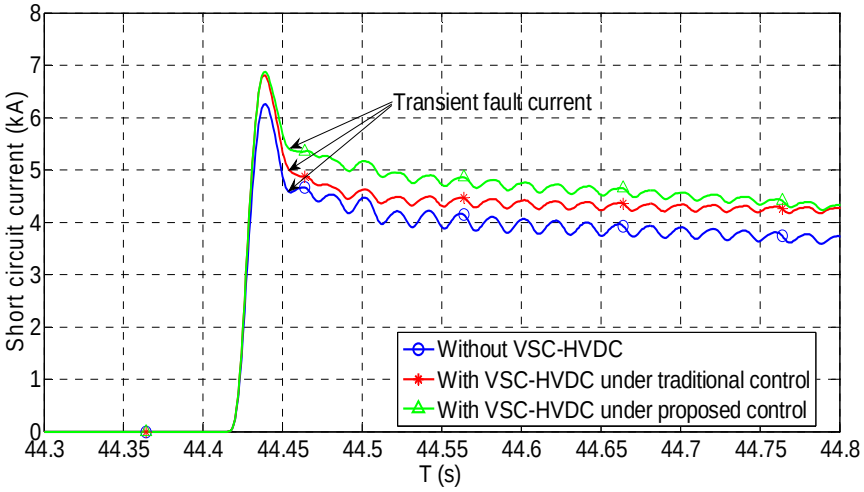

Fig.4.7. System short circuit current on BUS1 with different situations.

proposed control method above, it can be anticipated that the system short circuit current will be further increased when applying the proposed control method. Fig 4.7 then gives the system symmetrical short circuit current under the three situations.

It can be seen clearly from the simulation results that without the VSC-HVDC link, the system short circuit current is the smallest. When applying the VSC-HVDC link in the system, the short circuit current is increased since the reactive current supplied from the VSC under the fault. Furthermore, the short circuit current of the system achieves the largest value when applying the proposed control method on the VSC-HVDC link, which shows that the system voltage stability is effectively enhanced through the proposed control strategy.

4.4.2 Three-Phase-to-Ground Fault at the Transmission Line between BUS1 and BUS3

Fig. 4.8 shows the simulated waveforms for the system with a three-phase-to-ground fault at the transmission line between BUS1 and BUS3. The fault occurs at the instant of 40 s and is cleared by CB1 and CB2 0.1 s later. A reclosure takes place at 40.7 s. The three different scenarios under conventional control method corresponding to the different pre-setting current limits, as shown in Fig. 4.2, are evaluated together with the situation when applying proposed control strategy.

Before the fault is cleared, it is seen from Fig. 4.8 (a) and (b) that the voltage at BUS1 drops to nearly zero and the voltage at BUS2 drops to 0.3 p.u. once the fault occurs. The induction motors decelerate due to the mismatch between the electromagnetic torque and the mechanical torque, as shown in Fig. 4.8 (e).

From Fig. 4.5 it is known that the capability of the VSC-HVDC link decreases significantly with the voltage drop at BUS2. Furthermore, depending on the setting of current limits, the extents of reducing active power and increasing reactive power are different, as shown in Fig. 4.8 (c) and (d). It can be seen that with the proposed adaptive current limiter, the severe voltage drop at BUS2 moves the current reference vector to the current boundary and then rotate clockwise until the point D in Fig. 4.4, where all the VSC-HVDC capability are utilized to contribute reactive power support to the system. Notice that little change arises on the system frequency before the fault is cleared, as shown in Fig. 4.8 (f), due to the voltage-dependent load characteristic.

Once the fault is cleared at the instant of 40.1 s, the system voltages begin to recover. From Fig. 4.8 (c) and (d), it is clearly seen that the higher the reactive current reference limit, the more reactive power support can be obtained in the three scenarios of the conventional control method. In contrast, with the proposed adaptive current limiter, the reactive current limit reaches the full current limit and the maximum reactive power support is obtained. Consequently, the adaptive current limiter realizes the highest system voltage recovery level and lowest speed reduction of the induction motors, as shown in Fig. 4.8 (a), (b) and (e).

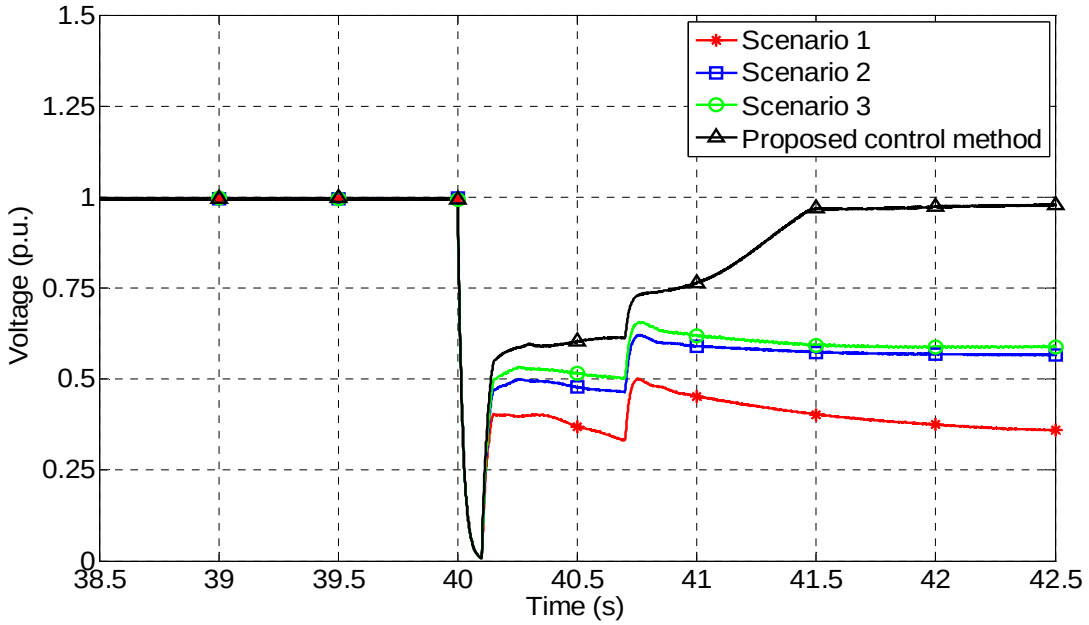

(a) Voltage at BUS1.

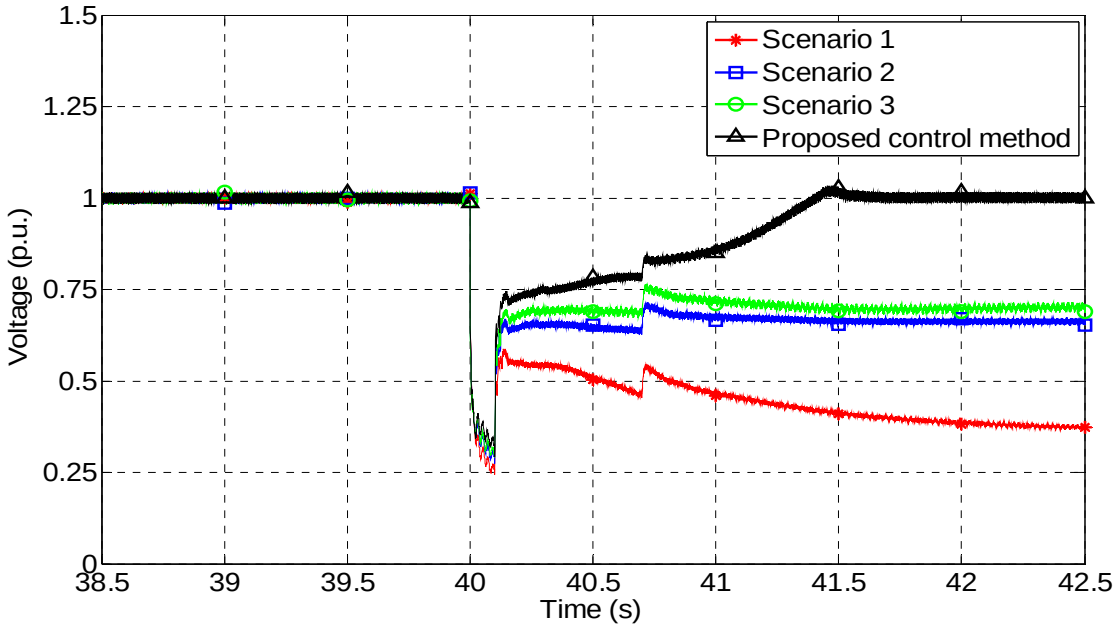

(b) Voltage at BUS2.

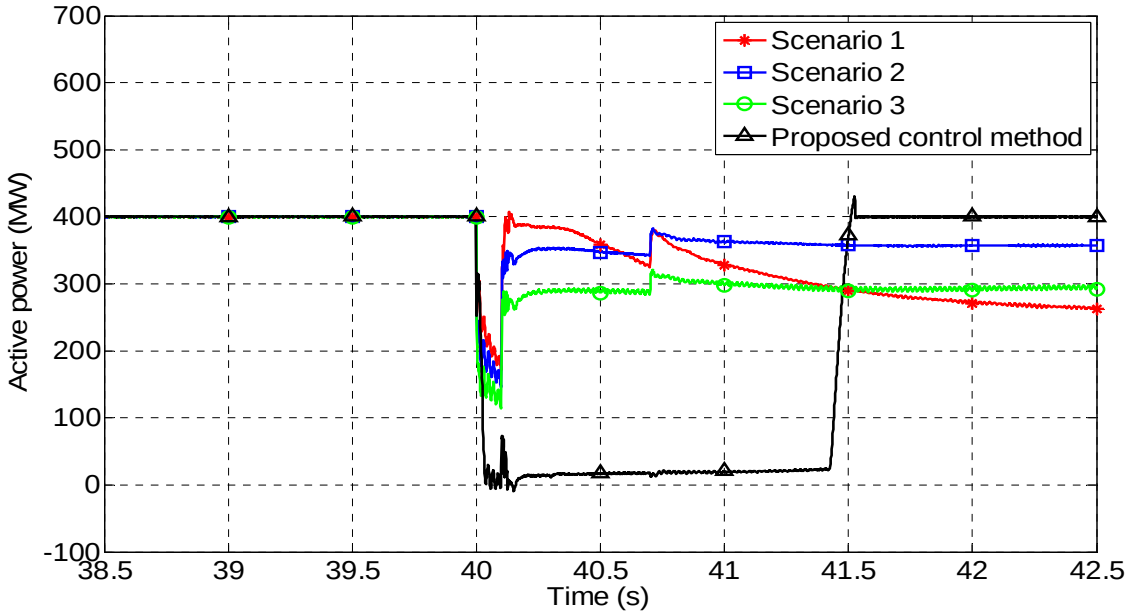

(c) Active power of VSC-HVDC.

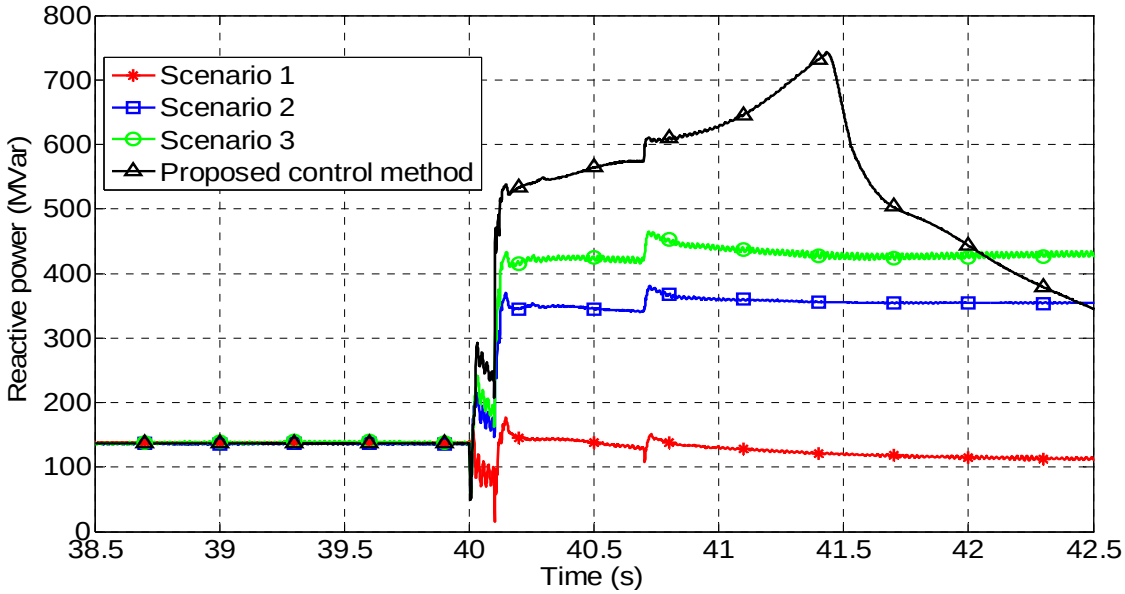

(d) Reactive power of VSC-HVDC.

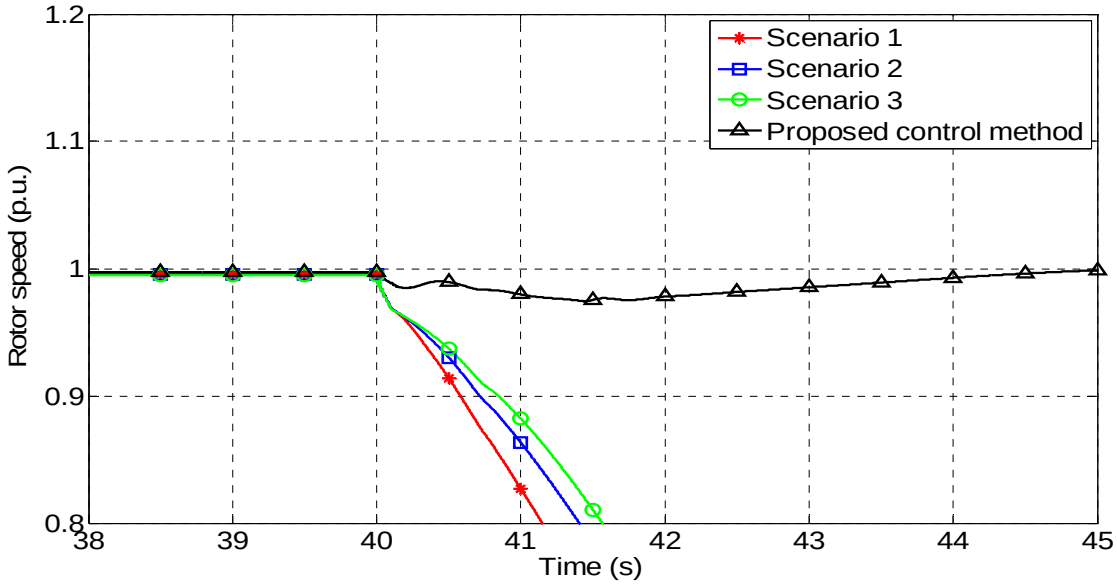

(e) Rotor speed of induction machine at BUS1.

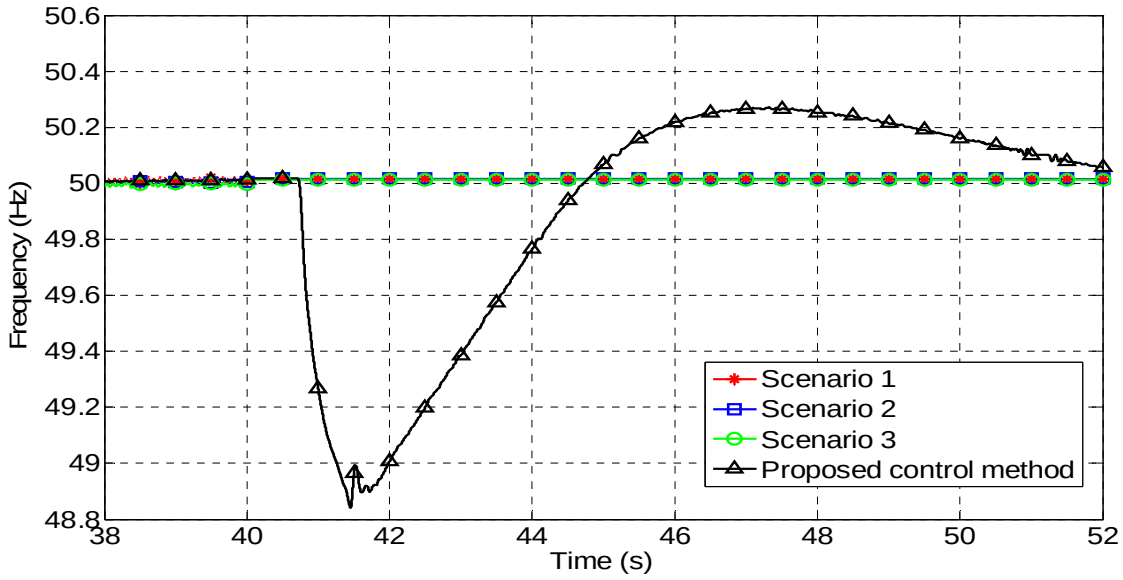

(f) System frequency.

Fig. 4.8. System performance under grid fault of three phase to ground with different control law.

At the instant of 40.7 s, the CB1 and CB2 reclose and the system structure is restored. From the voltage waveforms, it can be seen that the adaptive current limiter enables the VSC to provide sufficient reactive power support in order to restore the system voltages, whereas the conventional control method fails to recover the system voltages and the speed of induction motors keeps reducing to make the system unstable. It implies that a full reactive power support capability is needed under the severe voltage drops to ensure a stable operation of power system.

Furthermore, once the voltage at BUS2 recovers back to the rated value using the adaptive current limiter, the reactive current reference drops down quickly and release the control margin to the active current. Then, the current reference vector of the VSC-HVDC moves back to the original operation point, and the output powers of the VSC-HVDC go back to nominal value. However, before the voltage at BUS2 reaches the rated value, the reactive current reference is kept as the full current limit value. Then, the active power injected from VSC-HVDC is kept almost zero, whereas the active power demanded from the load increases due to the restoration of the system voltage. As a consequence, the system frequency keeps reducing till the instant of 41.5 s when the system voltage becomes higher than the rated voltage, as shown in Fig. 4.8 (f). Nevertheless, it is worthy to note that such a transient fluctuation of the system frequency is in the acceptable area according to the Grid Code [6] hence it is not perceived as a stability problem.

4.4.3 Voltage Sag Caused by the Remote Grid Fault

Fig. 4.9 shows the simulated waveforms under the system voltage sag resulting from a remote grid fault. In this case, the voltage disturbance is represented by a short circuit to ground through an inductance at BUS3. The voltage sag is assumed small compared to the Case in subsection 4.4.2, so that there is no action on any circuit breakers in the HMIDC system. The voltage sag occurs at 40 s and last about 0.5 s.

Fig. 4.9 (a) and (b) shows the different system voltage sags corresponding to different settings of the current limit during the fault period. It is clearly seen that the higher the reactive current reference limit, the smaller the voltage sag presents in the three scenarios of the conventional control method. Also, from Fig. 4.9 (d), it can be seen that the reactive power support from the VSC is enhanced with the increase of reactive current reference limit.

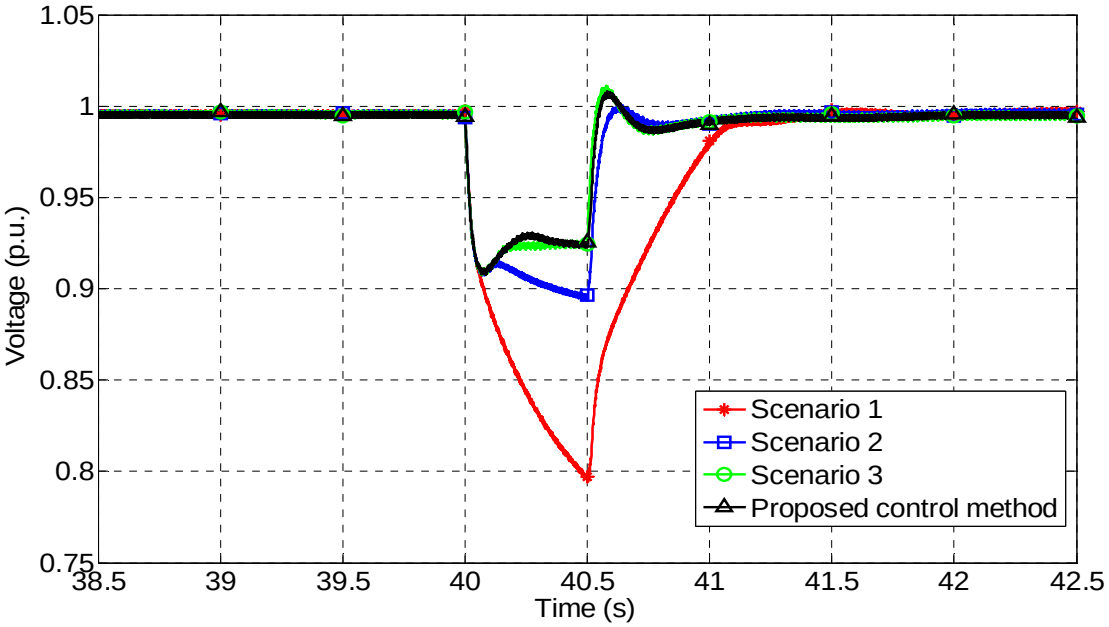

(a) Voltage at BUS1.

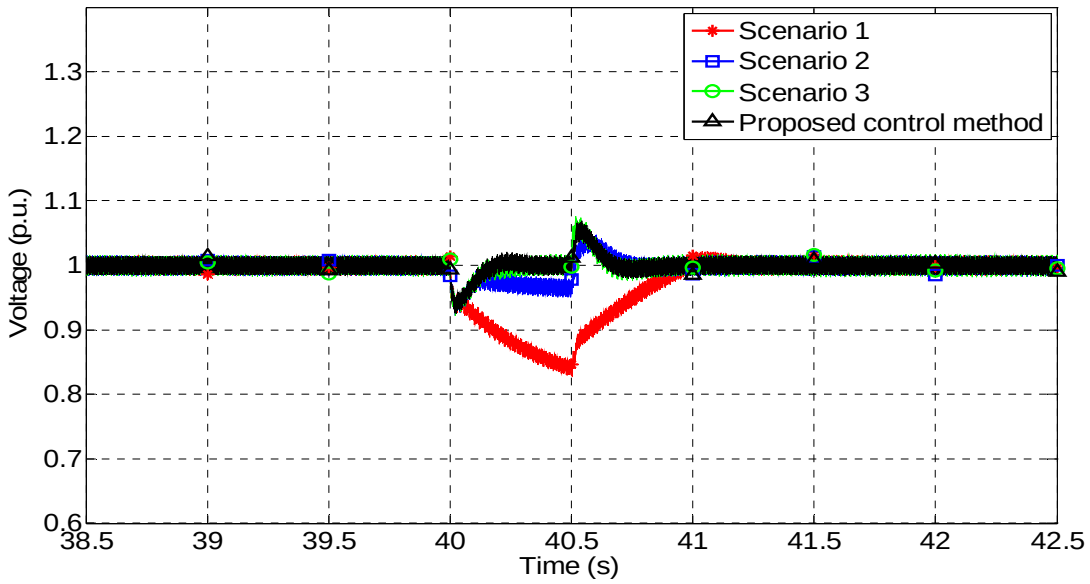

(b) Voltage at BUS2.

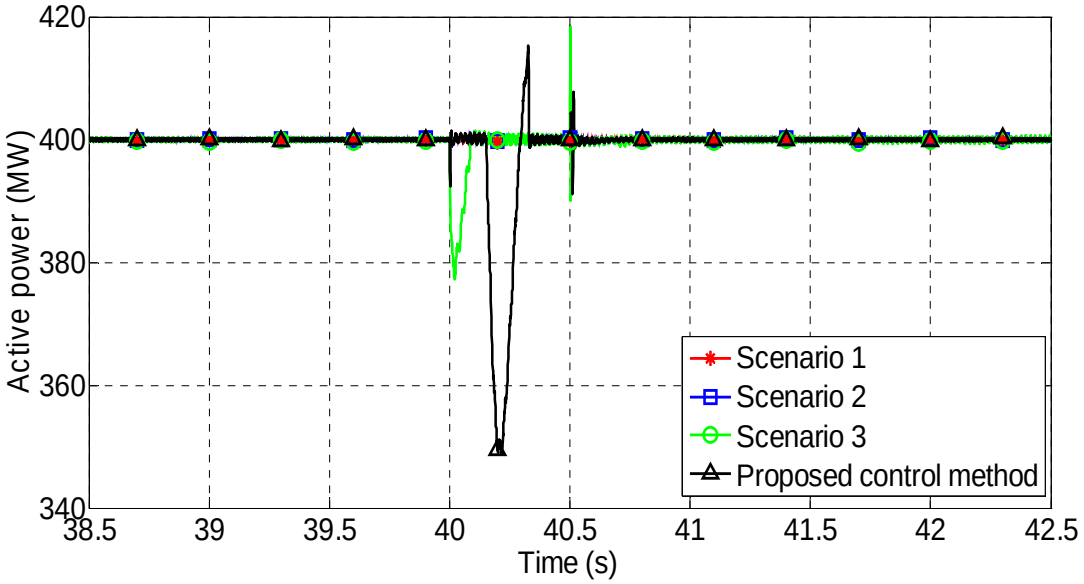

(c) Active power of VSC-HVDC.

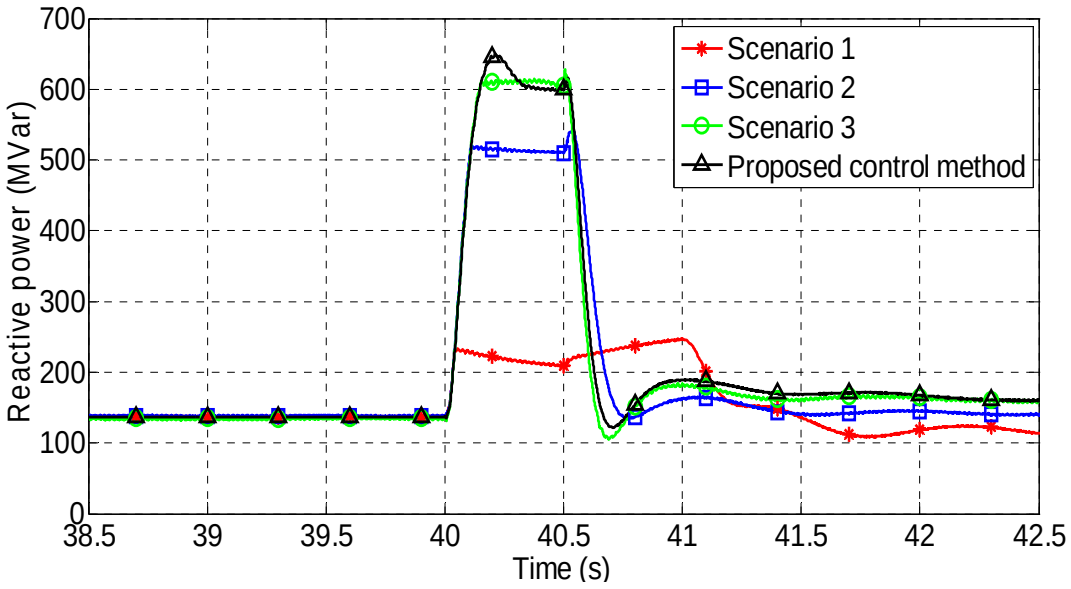

(d) Reactive power of VSC-HVDC.

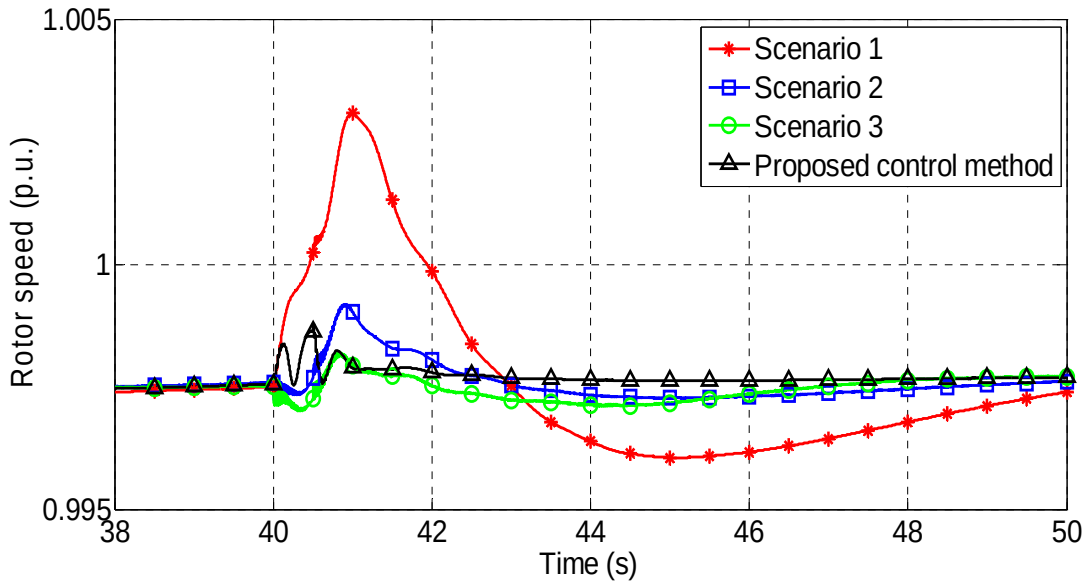

(e) Rotor speed of induction machine at BUS1.

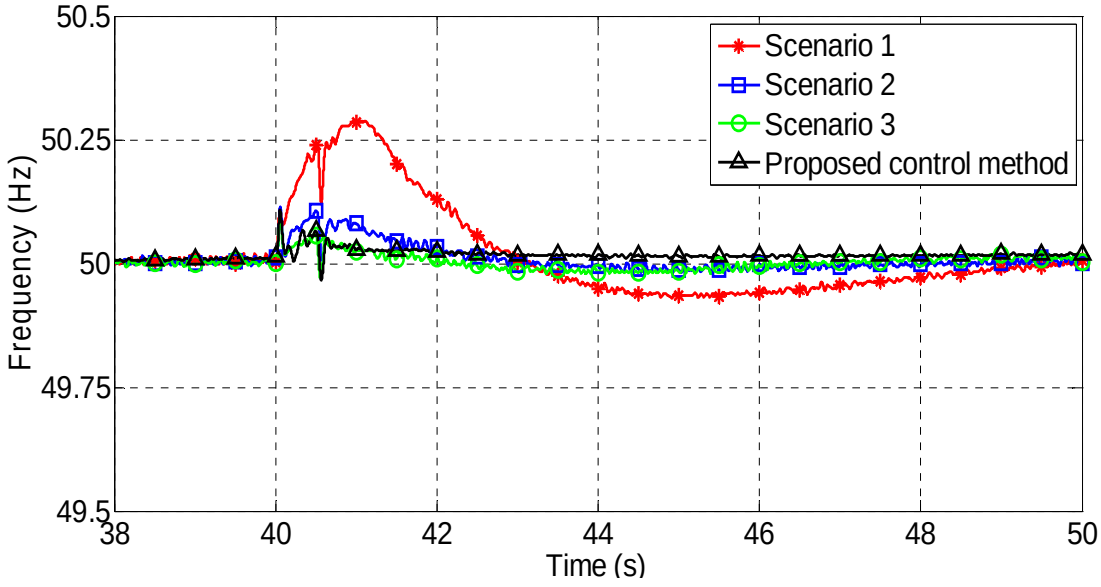

(f) System frequency.

Fig. 4.9. System performance under grid fault of voltage sag.

Notice that the presence of the active power dip in scenario 3 is caused by the low active current margin in this case. Once the fault occurs, the small voltage dip at BUS2 has little effect on the capability of the VSC-HVDC. Thus, an increase on the active current is needed to maintain the output active power, whereas the active current limit in scenario 3 is still kept as the rated active current as discussed in Section 4.2. Hence, a small active power dip appears at the beginning of the fault and then disappears rapidly.

Fig. 4.9 (e) shows the speed change of the induction motor at BUS1. It is seen that an increase with different extent arises during the voltage sag, and the less the reactive current limit reference, the higher the motor speed increases. Notice that similar variation can also be observed in the system frequency, as shown in Fig. 4.9 (f). This is resulted from a temporary unbalance of active power. Little change on the output active power of LCC-HVDC and generators appears due to the small voltage sag in system. And the active power of VSC-HVDC is kept almost the same by the active power controller, whereas the active power demand from the load is reduced with the voltage drop. Hence, the extra active power accelerates the induction motor and increase the system frequency correspondingly. However, with the proposed control method, the temporary active power drop of VSC-HVDC alleviates this unbalance of active power. As a consequence, the fluctuations of the induction motor speed and the system frequency is the smallest one.

4.4.4 Sending-End Grid Fault

To further confirm the performance of the proposed control method, the effect of the sending-end grid fault in the HMIDC system is evaluated in the simulation study. Fig. 4.10 shows the system waveforms under both the temporary and permanent fault conditions at the sending-end grid.

Considering the worst situation, a three-phase short circuit to ground is assumed to occur at the connection bus of VSC-HVDC link in the sending-end grid. Two cases are considered, which includes 1) the fault is temporary and cleared after 0.4s of fault occurrence, and 2) the fault is permanent and rectifier of HVDC link is blocked after 0.4s of fault occurrence.

Notice that in the second case, the fault results in a permanent loss of the active power injection from VSC-HVDC to the grid. Thus, some other controllers have to be activated to keep the system

frequency stable, such as the injection of spinning reserve of generator or the load shedding. In this simulation study, 50% of the active load at BUS3 and BUS4 are shed once the system frequency drops down to 48 Hz.

Fig. 4.10 (a) and (d) shows the simulated system voltage and the reactive power waveforms of the VSC-HVDC link. During the sending-end grid faults, the delivered active power drops down significantly, whereas little reactive power disturbance is imposed on the receiving-end grid, hence the infeed AC system voltages keep around the rated values, as shown in Fig. 4.10 (a), and the reactive power of VSC-HVDC in such case has little fluctuation, as shown in Fig. 4.10 (d).

Fig. 4.10 (b) and (c) shows the DC voltage and active power waveforms of the VSC-HVDC system. Notice that the active power transmission failure decreases the DC-link voltage of VSC-HVDC system. Thus, the sending-end grid fault can be detected by measuring the DC-link voltage at the receiving-end converter. Once the DC voltage drops below 0.9 p.u., the active power loop switches from controlling the active power to keeping the DC voltage constant, as shown in Fig. 4.10 (b). Thus, the output active power is controlled to be zero, as shown in Fig. 4.10 (c). Due to the loss of active power, the system frequency and the induction motor speed becomes decreased, as shown in Fig. 4.10 (e) and (f).

In the first case of temporary grid fault, after the fault clearance (40.4s), the active power transmission is thus restored and DC voltage is increased to the rated value, as shown by the red lines in Fig. 4.10 (b) and (c). Also, the system frequency is increased to 50 Hz again and the rotor speed restore to the rated value. During the recovery period, it is noted that the reactive power demand from the static load is higher than the normal operation due to its frequency-dependent characteristic in (2), and meanwhile, the speed restoration of the induction motor needs both the active and reactive power support. Thus, an increase of the reactive power consequently appears at the output of VSC, as shown in Fig. 4.10 (d), such that the system voltage only has a small dip, as shown in Fig. 4.10 (a).

In the second case of permanent grid fault, after 0.4 s of fault occurrence, the sending-end converter of the VSC-HVDC link is blocked, and the receiving-end converter is switched into a STATCOM operation, in which the active current reference is extended below zero, as shown in Fig. 4.6. The DC voltage is maintained by injecting active power from the infeed system to the DC

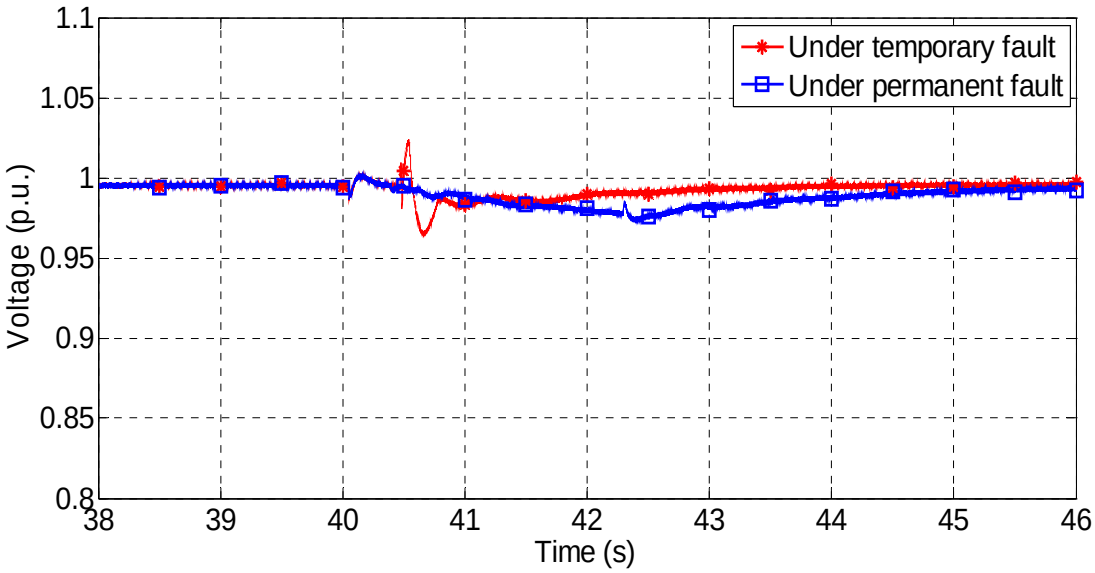

(a) Voltage at BUS1.

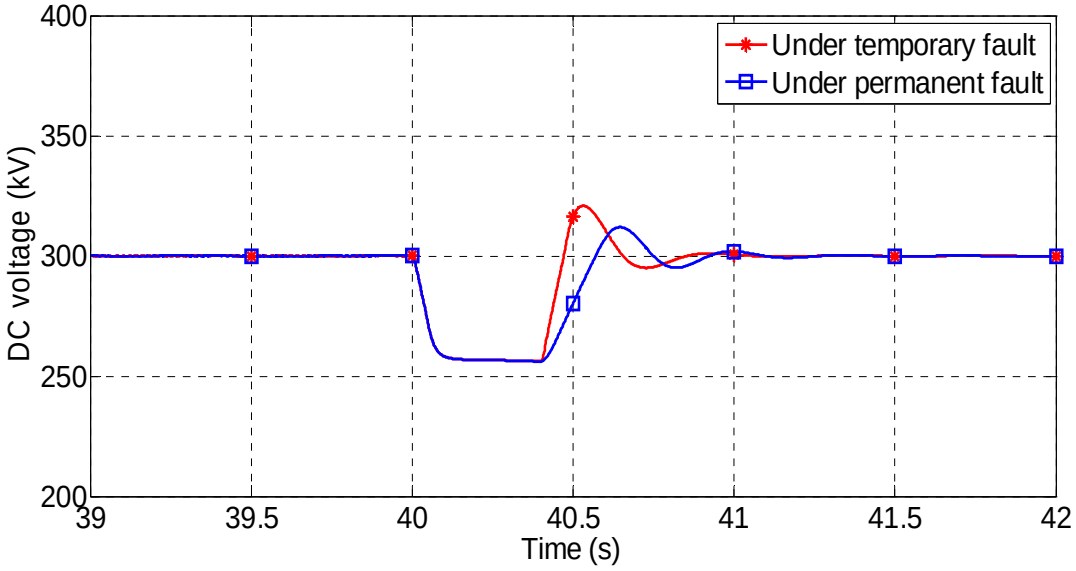

(b) DC voltage of VSC-HVDC link.

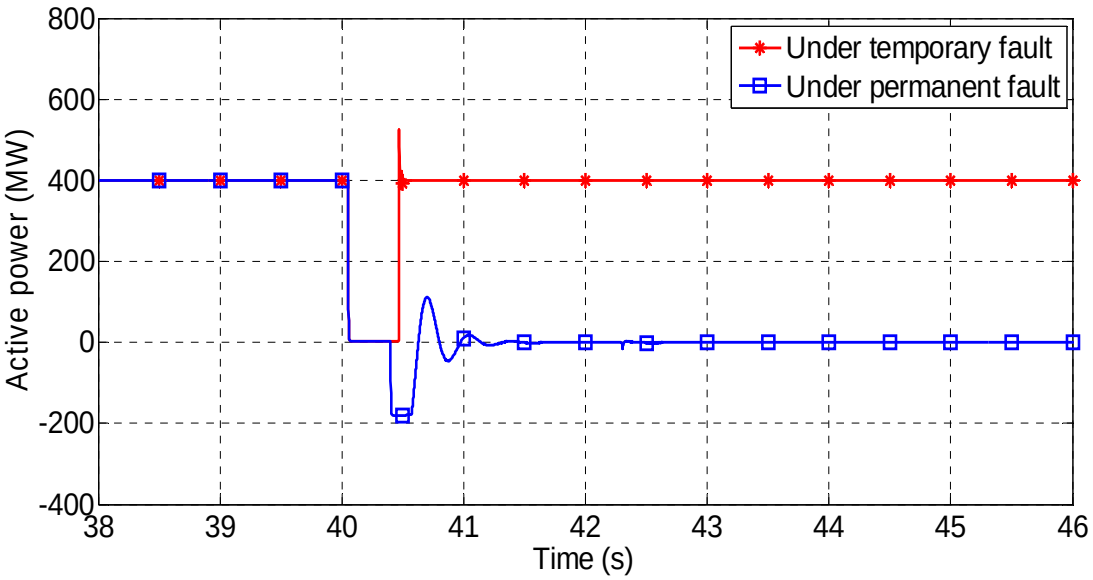

(c) Active power of VSC-HVDC.

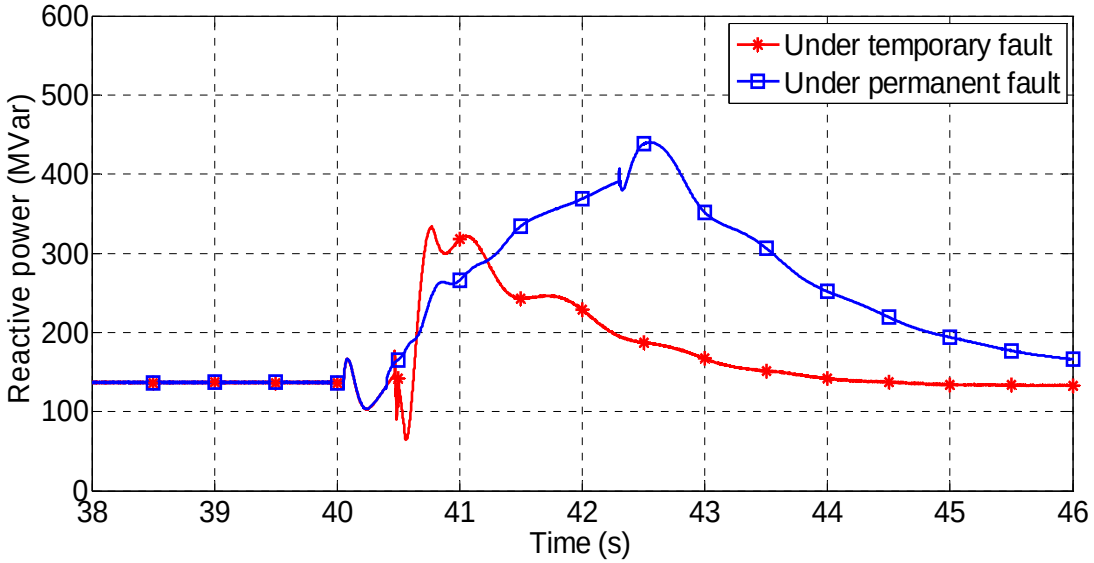

(d) Reactive power of VSC-HVDC at grid side.

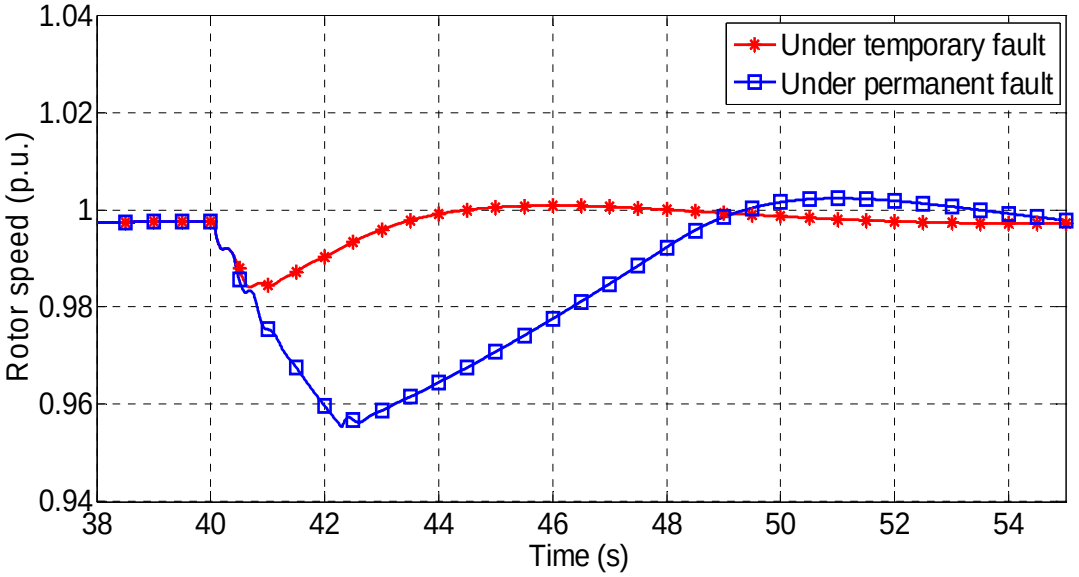

(e) Rotor speed of induction machine at BUS1.

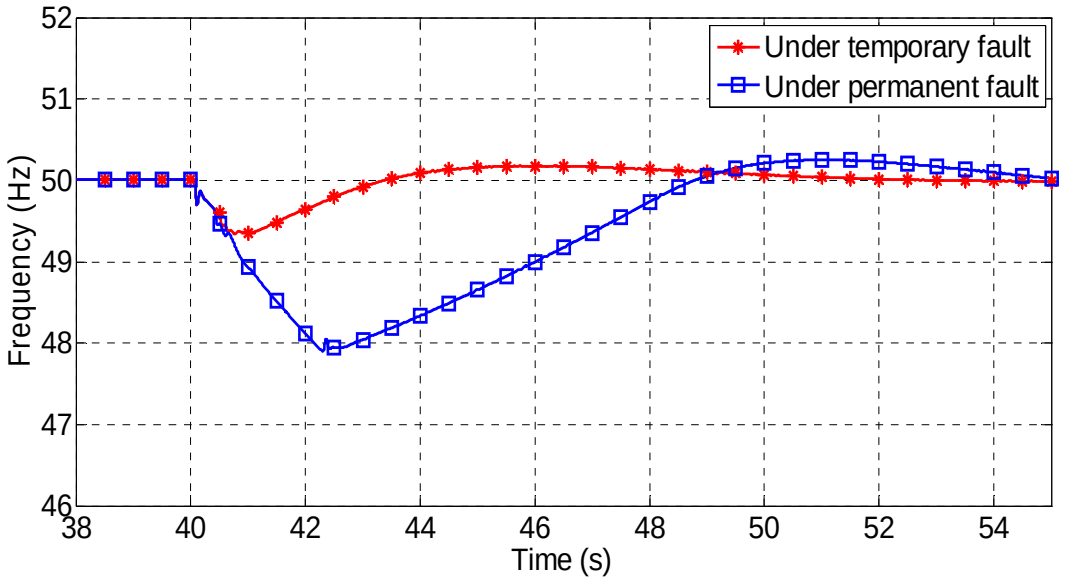

(f) System frequency.

Fig. 4.10. System performance under grid fault at sending end of VSC-HVDC.

capacitor, as shown in Fig. 4.10 (b). Fig. 4.10 (c) shows the inverse active power flow of the receiving-end converter.

To maintain the system frequency stable, the load shedding at BUS3 and BUS4 is enabled once the system frequency is lower than 48 Hz. After the load shedding, system frequency is increased and the speed of induction motor is also increased consequently, as shown by the blue lines in Fig. 4.10 (e) and (f).

Furthermore, from Fig. 4.10 (d), it is clearly seen that due to the larger drops of induction motor speed and system frequency compared to the temporary fault case, the needed reactive power is consequently higher.

4.5 Summary

In order to make the AC grid stiffer with higher ESCR value, this Chapter proposes a power control method for the VSC-HVDC link. The control method can achieve the required current angle of VSC under short circuit situation, which increase the ESCR to a satisfactory value. Thereby, system voltage stability can be improved.

The proposed control method is verified by simulation study in PSCAD. Three disturbance situations in the AC system have been considered and the simulation results show that the proposed power control method can support system voltage more effectively. Hence the system voltage stability can be significantly improved in comparison with the traditional VSC-HVDC control method.

Bibliography:

[1] C. Feltes, H. Wrede, F. W. Koch, I. Erlich, "Enhanced Fault Ride-Through Method for Wind Farms Connected to the Grid Through VSC-Based HVDC Transmission," IEEE Trans. Power Syst., vol. 24, no. 3, pp:1537-1546, Aug. 2009.

[2] L. Zhang, L. Harnefors, and H.-P. Nee, "Power-Synchronization Control of Grid-Connected Voltage-Source Converters," IEEE Trans. Power Syst., vol. 25, no. 2, pp: 809-820, May. 2010.

[3] L. Xu, and S. Li, "Analysis of HVDC light control using conventional decoupled vector control technology," in Proc. IEEE PES General Meeting, 2010, pp:1-8.

[4] C. Du, E. Agneholm, and G. Olsson, "VSC-HVDC System for Industrial Plants With Onsite Generators," IEEE Trans. Power Del. vol. 24, no. 3, pp:1359-1366, Jul. 2009.

[5]] S. P. Teeuwsen, C. Rasmussen, and H. Abildgaard, "Dynamic performance of the new 400 kV Storebaelt HVDC project," in Proc. IEEE/PES Power Systems Conference and Exposition, 2009, pp:1-7.

[6] M. Tsili, and S. Papathanassiou, "A review of grid code technical requirements for wind farms," IET Renew. Power Gener., vol. 3, no. 3, pp. 308–332, 2009.

Chapter 5

Cooperative control of VSC-HVDC Connected Offshore Wind Farm with Low-Voltage Ride-Through Capability

5.1 Introduction

According to the analysis in above chapters, the influence to the system stability by the system parameters and VSC-HVDC links has been investigated in detail. However, the influence from the wind power is not considered in the above studies. As explained in the very beginning, the studied HMIDC system is supposed to connect with the offshore wind farm through the VSC-HVDC link. Hence the influence to system stability from the offshore wind farm would also be an important research issue in this project.

In recent years, driven by the fast revolution of power electronics technology, the VSC-HVDC system has received significant attention on the offshore wind power integration due to its fixable controllability. A number of VSC-HVDC applications on the integration of offshore wind farms have been reported [1-5].

Due to the intermittent nature of wind power, the impact of large wind farms on power system operations have attracted more and more attention. Since the large wind farms have ratings like conventional power plants, the disconnection of a large amount of wind power during fault may result in serious stability problems. A number of grid connection codes requiring the Low-Voltage Ride-Through (LVRT) capability have been imposed on wind power systems [6], which imply that the wind turbines and wind farms should be able to continuously connect to the network for a certain time period during grid faults and voltage sags.

The requirement of LVRT capability offers a new challenge to the wind farm integration through VSC-HVDC link. During the system fault, receiving end converter (REC) cannot inject all the power into the grid, whereas the power from the wind farm keep flowing to the DC link through sending end converter (SEC) because valves of VSC have no reverse blocking capability. Hence the imbalanced power through SEC and REC charges the DC capacitance and results in a large increase on DC voltage quickly, which is unacceptable for the HVDC equipment. Therefore, the key point in achieving the LVRT capability of VSC-HVDC connected wind farm is to restrain the increment of DC voltage of VSC-HVDC system under the grid fault.

A number of research efforts have been spent to achieve this objective. According to different techniques adopted, these schemes can be grouped as:

1. Release the excess power through a full-rated DC chopper at the DC circuit.
2. Active power reduction of wind turbines according to the power set point signal from the SEC.
3. Transferring the grid fault to wind farm side AC bus.
4. Active power reduction of wind turbines through frequency control on SEC.

In scheme 1 the DC chopper circuit is used to dissipate the excess power on the chopper resistance, which is simple but costly [7], [8].

In order to bring down the active power generated from the wind farm, the power set point of each wind turbine (WT) can be calculated sent through the communication link during the fault in scheme 2 [9]. This scheme can only achieved with the help of fast communication links between the VSC-HVDC system and WTs. However, the use of communication lines may bring cost and reliability issues.

Scheme 3 gives a way to reduce the wind power transmission without communication links, which is the voltage reduction at wind farm grid. With the voltage decrease at wind farm AC bus through SEC controller, the grid side fault is transferred to wind farm side, the wind farm output power thus drop down rapidly and the decreased voltage can be adopted to produce the power signal for converter-based WTs [10]. However, in this scheme the back-to-back converters of WTs can only apply voltage control at their outer control loops, because the wind power regulation is the based on

the wind farm voltage detection. On the other hand, unlike frequency, the ac voltage in wind farm would be different at each wind turbine due to the transmission line impedance, which may affect the control ability of the voltage-based method. Another drawback of this scheme is that the emulated fault at wind farm grid may results in typical short circuit currents with high DC components [11], which leads to mechanical stress for WT drive train and electrical stress for the valves of converters of HVDC and converters connecting with wind generators [12].

Another way to decrease the wind power transmission without communications is scheme 4. Instead of delivering the power set point signal by communication links, the WF frequency is adopted in this scheme for the power reduction. Under grid fault situation, the WF frequency is increased through SEC controller. For fixed speed induction generators and DFIGs, the active power transmission from wind turbine would be reduced directly due to the frequency increase. For the fully rated converter-based WTs, the increased frequency can be detected as the fault signal and a fast frequency control is needed to reduce the wind power output.

According to the comparison of those schemes, the scheme 4 seems a good choice for enhancing the wind farm LVRT capability with VSC-HVDC. The application of scheme 4 on the fixed speed induction generator and DFIGs have been studied in [13] and [14], whereas due to the requirement of fast frequency control, the research about this scheme on fully rated converter-based WTs are lacked in previous literatures.

In this chapter, a cooperative control strategy for variable speed SCIG-based offshore wind farm connecting with VSC-HVDC system is proposed. The approach is based on scheme 4 and employs a fast frequency control to regulate the active power output of each wind turbine. The DC-link voltage versus offshore AC-bus frequency droop control is adopted on the offshore converter side of VSC-HVDC link. And the back-to-back converters of variable speed SCIG-based wind turbines adjust the generated active power based on the AC-bus frequency deviation through the fast frequency controllers. To evaluate the performance of the proposed control scheme, a 300 MW variable speed SCIG offshore wind farm connecting with a VSC-HVDC link is modeled in the EMTDC/PSCAD. Simulation results confirm the effectiveness of the control method.

5.2 Modeling of the VSC-HVDC connected offshore wind farm

5.2.1 System layout

Fig. 5.1 shows the diagram of the studied 300MW offshore wind farm connecting with a VSC-HVDC link. The wind farm consists of SCIG-based wind generators interfaced to the offshore collection bus with fully rated back-to-back converters, and the power rating of each wind turbine is 2MW. The parameters of SCIG-based wind generator are given in Table 5.1

A VSC-HVDC link composed by two converter stations, DC cables, DC capacitors and AC filters is connected to the offshore ac-bus to integrate the wind power into onshore AC network. In each converter station, an IGBT-based two level converter is connecting the DC link to the AC bus. The parameters of VSC-HVDC link in the studied system are shown in Table 5.2.

TABLE 5.1

PARAMETERS OF SCIG-BASED GENERATOR

Parameters	**Wind generator**
MVA	2MW
Rated L-L voltage	0.69kV
Inertia	5 s (J=2H)

TABLE 5.2

HVDC SYSTEM PARAMETERS

Parameters	**VSC-HVDC**
Rated capacity	400 MVA
Rated AC voltage (line-line)	150 kV
DC voltage	300 kV
Switching frequency	1650Hz
DC cable	100km
DC capacitor	70uF

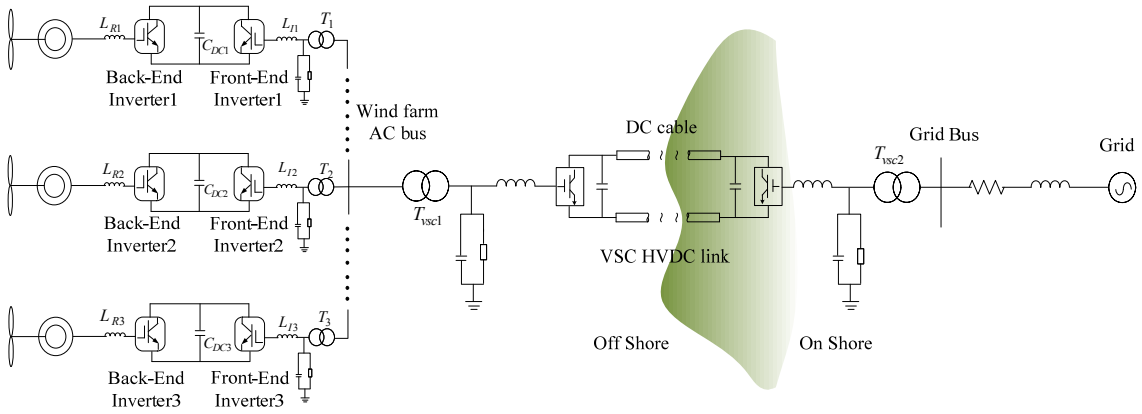

Fig.5.1 SCIG-based variable speed offshore wind farm connecting with VSC-HVDC Link

5.2.2 The aerodynamic model of wind turbine

The aerodynamic model of wind turbine is developed based on the algebraic relation between wind speed and mechanical power extracted [15]:

$$P_w = \frac{1}{2}\rho A_r c_p(\lambda,\theta) v_w^3 \tag{5.1}$$

where P_w is the power extracted from the wind, ρ is the air density; c_p is the performance coefficient or power coefficient; V_w is the wind speed and θ is the pitch angle of rotor blades; A_r is the area covered by the rotor; λ is the tip speed ratio which defined as:

$$\lambda = \frac{\omega R}{v_w} \tag{5.2}$$

where, ω is the wind turbine rotation speed and R is the blade radius. For the given values of λ and θ, with the numerical approximations[16], c_p can be calculated as:

$$c_p(\lambda,\theta) = 0.73\left(\frac{151}{\lambda_i} - 0.58\theta - 0.002\theta^{2.14} - 13.2\right)e^{-18.4/\lambda_i} \tag{5.3}$$

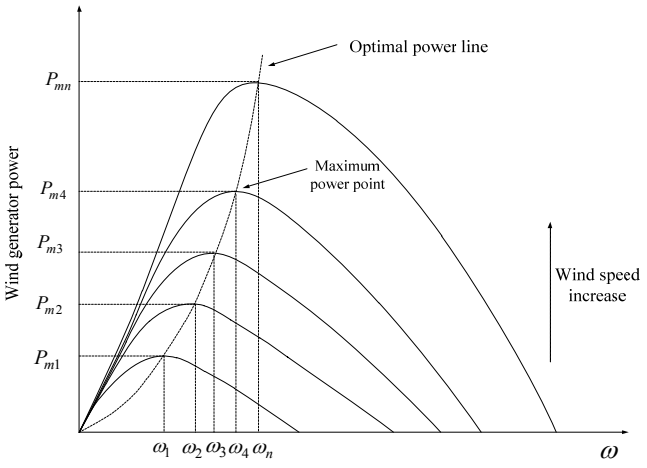

Fig. 5.2 Wind generator curves at various wind speed

where,

$$\frac{1}{\lambda_i} = \frac{1}{\left(\lambda - 0.02\theta\right)} - \frac{0.003}{\left(\theta^3 + 1\right)} \tag{5.4}$$

The wind generator power curves for various wind speeds are shown in Fig. 5.2 [17]. It can be found that for different wind speed, the maximum wind power can be achieved at a corresponding wind turbine rotating speed. It is expected that the maximum wind power can be extracted with different wind speed.

The dashed line in Fig. 5.2 shows the maximum power trace along with wind speed variation. According to the wind power equations (5.1)-(5.4), the optimum wind power, i.e. the power shown by the dashed line can be presented as:

$$P_{\max} = K_w \omega^3 \tag{5.5}$$

where,

$$K_w = \frac{1}{2}\rho\pi R^5 \frac{C_{pM}}{\lambda_M} \tag{5.6}$$

Hence (5.5) can be used as the power reference in the control loop of wind generator to realize the maximum wind power tracking.

5.3 Control system of the induction machine based variable speed wind turbine

During wind power development, the early generator used on wind turbines is the Squirrel-Cage winding Induction Generator (SCIG) and nowadays it is still a very attractive choice for wind power generation because of its simplicity, robust, low cost, reliability, efficiency and economical advantages. The SCIGs are the most widely used machine at fixed speed. The research on the SCIG-based fixed speed wind turbines connecting with VSC-HVDC can be found in previous literatures [18], [19]. However, to achieve maximum energy capture in a wide range of wind conditions, back-to-back converters are applied together with SCIG based wind generator, which is also called SCIG-based variable speed wind turbine.

In the existed studies on LVRT capability of VSC-HVDC connected wind farm, few documents are focus on the SCIG-based variable speed wind farms, and the study on LVRT capability improvement of this kind of system is also lacked. Hence in the studied system, SCIG-based variable speed wind turbine is applied in the offshore wind farm, and the control strategies of the back-to-back converters connecting the generator and offshore AC bus are explained below in this subsection.

5.3.1 Rotor flux oriented control on back -end converter

The vector controls are conventionally adopted on the voltage source converter-based induction machine, including the stator flux-oriented control, rotor-flux oriented control, and magnetizing-oriented control. In this study, the rotor-flux oriented control is applied on the back-end converter connecting with the wind generator.

As the space phasors of the generator are all presented in the rotor-flux oriented coordinate system, it is easy to know that

$$\begin{cases} \psi_r = \psi_{rd} \\ \psi_{rq} = 0 \end{cases} \tag{5.7}$$

where ψ_r is the rotor flux and ψ_{rd} and ψ_{rq} are the component of rotor flux on the *d*- and *q*-axis, respectively.

Then under the rotating reference coordinate system oriented on the rotor flux, according to the equivalent circuit of the induction machine, the electromagnetic torque of the generator can be derived as [20]

$$T_e = \frac{3}{2} P \frac{L_m}{L_r} \psi_{rd} i_{sq} \tag{5.8}$$

where

$$\psi_{rd} = \psi_r = L_m i_{mr} = L_m i_{sd} \tag{5.9}$$

where T_e is the electromagnetic torque of generator, P is the number of pole pairs of the generator, L_m and L_r are the magnetizing inductance and the rotor induction, respectively, i_{mr} is the rotor magnetizing-current, and i_{sd} and i_{sq} are the stator current component on the *d*-axis and *q*-axis under the rotor-flux oriented rotating frame, respectively.

According to the relationship of the electromagnetic torque and the rotor flux and stator currents in equation (5.8) and (5.9), it can be found that if the parameters of the machine are considered to be constant, then the rotor flux is proportional to the *d*-axis stator current while the electromagnetic torque is proportional to the q-axis stator current expressed in the rotor flux-oriented reference frame.

Therefore, the rotor flux and electromagnetic torque of the generator can be controlled decoupled through the *d*-axis and *q*-axis stator currents, respectively.

On the basis of above analysis and equations, Fig. 5.3 shows the control strategy of the back-end converter oriented on the rotor flux. To realize the maximum wind power tracing, the torque reference T^* is obtained from the optimum power function $P_w = f(w_m)$ in order to attain maximum power at a given angular speed of the shaft. The inner current control loops include i_{wb_d} and i_{wb_q} are working in the rotating reference frame *dq* which oriented to the rotor flux. The generator flux and torque thus are decomposed and can be controlled in two separated paths, as shown in Fig. 5.3.

5.3.2 Vector current control on Front-end converter

The vector current control strategy is applied in this front-end inverter and the basic control principle of the control method adopted here is the same as the vector current control strategy applied on the VSC-HVDC converters which has been explained in Chapter 2.

Fig.5.4 shows the control diagram of the front-end inverter. The ac variables on the offshore ac-bus can be expressed in the synchronous d–q reference frame [21], where the d-axis is fixed to the voltage V_{wn}, as

$$\begin{bmatrix} V_{wnd} \\ V_{wnq} \end{bmatrix} = L_{fn} \frac{d}{dt} \begin{bmatrix} i_{wf\_d} \\ i_{wf\_q} \end{bmatrix} + \omega L_{fn} \begin{bmatrix} -i_{wf\_q} \\ i_{wf\_d} \end{bmatrix} + \begin{bmatrix} V_{cnd} \\ V_{cnq} \end{bmatrix} \tag{5.10}$$

where V_{wnd} and V_{wnq} , i_{wf_d} and i_{wf_q} are the d- and q-axis components of voltage V_{wn} and current vector flowing through the phase reactor, respectively. V_{cnd} and V_{cnq} represent the corresponding values of converter output voltage vector under reference rotating frame.

Using the power balancing equation, the active and reactive power transferred through the converter can be derived as

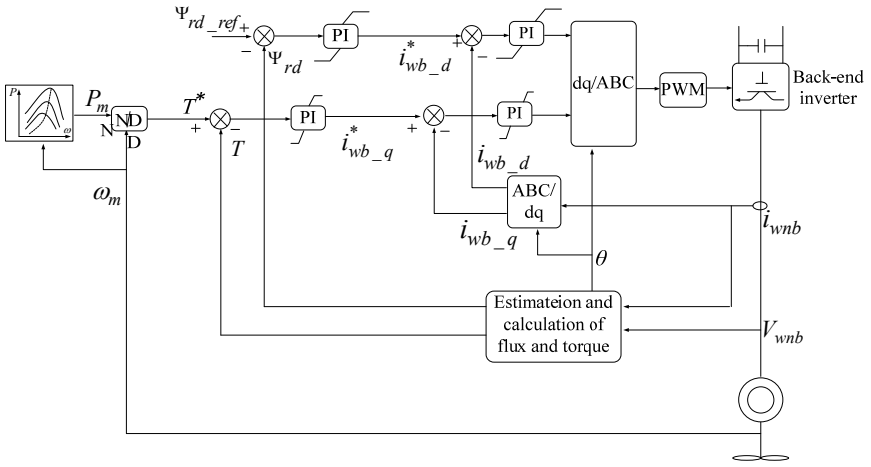

Fig. 5.3 Block diagram of control scheme on front-end converter

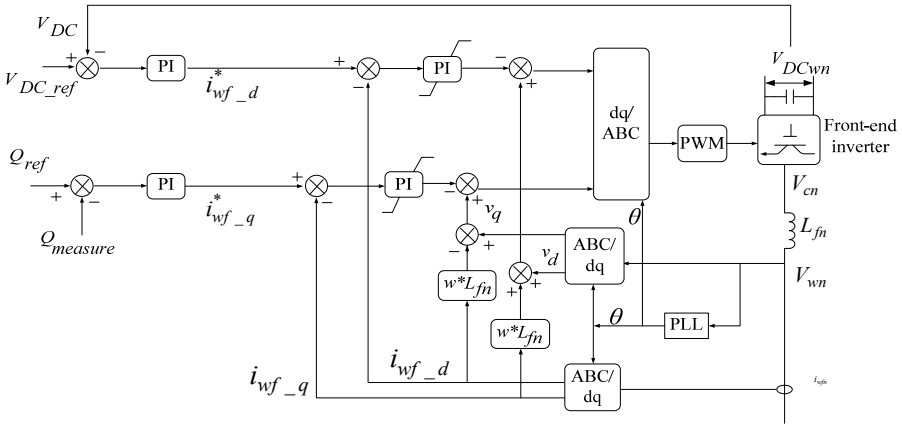

Fig. 5.4 Block diagram of control scheme on back-end converter

$$\begin{bmatrix} P_{wn} \\ Q_{wn} \end{bmatrix} = \frac{3}{2} i_{wf\_d} \begin{bmatrix} V_{wnd} \\ V_{wnq} \end{bmatrix} + \frac{3}{2} i_{wf\_q} \begin{bmatrix} V_{wnq} \\ -V_{wnd} \end{bmatrix} \tag{5.11}$$

As the reference synchronous frame is oriented on V_{wn}, V_{wnq} is zero and the active and reactive power can be given by

$$\begin{bmatrix} P_{wn} \\ Q_{wn} \end{bmatrix} = \frac{3}{2} i_{wf\_d} \begin{bmatrix} V_{wnd} \\ 0 \end{bmatrix} + \frac{3}{2} i_{wf\_q} \begin{bmatrix} 0 \\ -V_{wnd} \end{bmatrix} \tag{5.12}$$

It is obvious that the P_{wn} and Q_{wn} are proportional to i_{wf_d} and i_{wf_q}, respectively. In the studied system, the current order $i^*_{wf\_d}$ is obtained through DC voltage control loop and $i^*_{wf\_q}$ is derived from reactive power control loop.

5.4 Cooperative control of VSC-HVDC Connected Offshore Wind Farm with Low-Voltage Ride-Through Capability

Fig. 5.5 gives the overall control diagram of the HVDC connected offshore wind farm. The control scheme in Fig. 5.5 presents both the normal control strategies and the proposed control method for LVRT. Under steady state, the control variables in the proposed control part are zero and the system is operating with only normal control schemes. In the offshore wind farm, the back-to-back converters connected with each wind generator are controlled based on the same strategy. The back-end inverter applied rotor flux oriented control to regulate the electrical torque directly and vector current control method is used on front-end inverter. The offshore converter (Con. 1 in Fig. 5.1) of VSC-HVDC link is controlled as a voltage source, which supplies the offshore as-bus voltage. The onshore converter of HVDC is controlled to regulate the DC link voltage and grid bus AC voltage based on vector current control method.

The proposed control scheme can be explained in three parts: the frequency control on SEC, the production of power change signal based on frequency error and the fast power regulation on back-to-back converters of WT.

5.4.1 Frequency control on SEC

As explained above, the SEC is controlled as a voltage source. In the proposed control method, at the offshore AC bus, the voltage magnitude is kept constant while the voltage frequency is controlled according to the DC voltage error of the HVDC link. Note that there are neither loads nor generators on the offshore ac-bus. Hence the frequency under stable state there can be chosen at a relatively

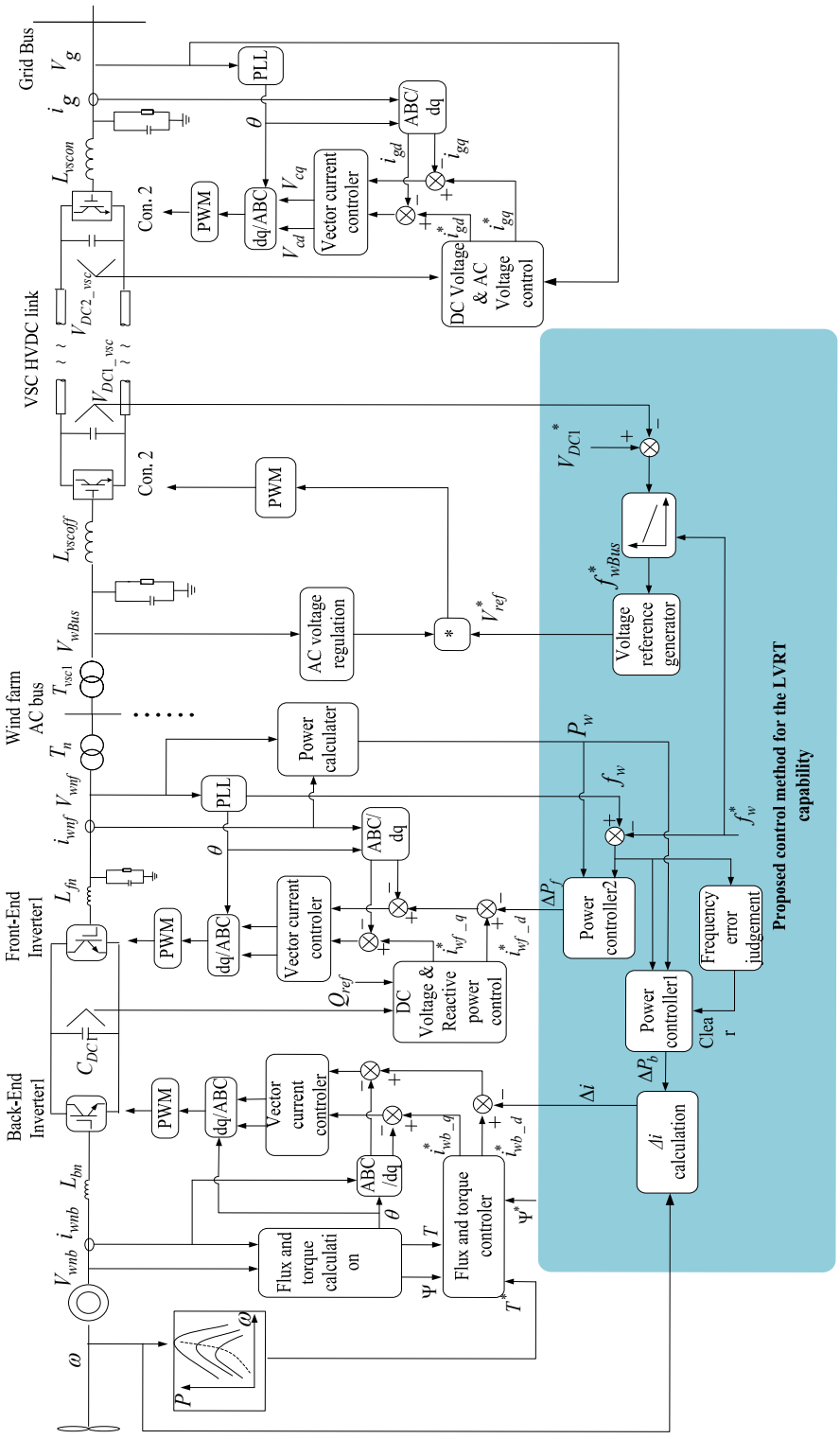

Fig.5.5 Overall control diagram of the HVDC connected offshore

low value—20Hz in this study, which can bring down the system power loss as well as the reactive current through the equivalent capacitor of ac transmission line.

During onshore power system voltage drop, the grid voltage drops, the power output of VSC HVDC to the grid drops down and the DC voltage is increased due to the power imbalance in HVDC system, the increment of DC voltage enables the proposed control circuit and is introduced into the HVDC offshore converter control loop, the offshore ac-bus frequency thus increased through the droop controller, as shown in Fig. 5.5.

5.4.2 Production of power change signal based on frequency error

At wind farm side, the changed offshore ac-bus frequency information is detected by each wind turbine. As shown in Fig. 5.5, two power reduction references ΔP_f and ΔP_b are obtained according to the frequency error and feed into the front-end and back-end converter control loops, respectively. The detailed control loop of the power reduction references based on frequency change for each wind turbine is drawn in Fig. 5.6.

To achieve a stable and rapid power reduction during onshore voltage drop, ΔP_b is obtained through a PID (proportional-indication-differential) controller and feed into the back-end inverter inner control loop to bring down the generator electrical torque. The integrator here is used to get a stable power reference whereas the differentiator is applied to increase the response speed of the controller.

It is noticed that even though the power controller 1 has a fast response speed, during the short transient after grid fault the power reduction at wind farm is still relatively low compare to the onshore power drop, which will result in a large increase on the DC link voltage. Hence, the other power reduction reference ΔP_f is feed into the front-end inverter inner control loop through PD (proportional-differential) controller at the same time. The differentiator here is also adopted for achieving a high response speed of power controller 2. Then the combination of controller 1 and 2 achieves a stable and fast enough power reduction of the wind farm during onshore voltage drop.

Note that for different wind turbines, the different wind speed may result in different active power

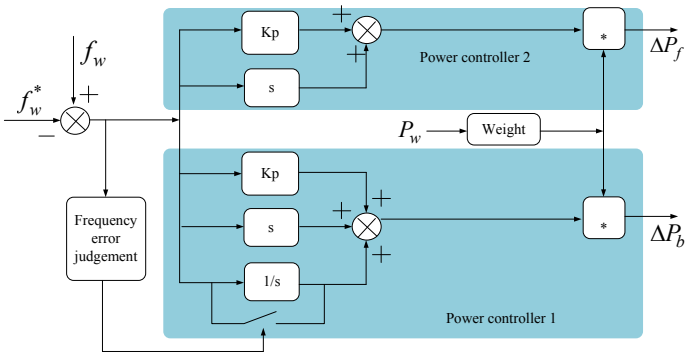

Fig. 5.6 The control scheme for regulated power signal

output under steady state. The power reduction of each wind turbine during onshore grid fault should be proportional to its operating power before the fault to make sure the required power reduction of the whole wind farm. Hence the power order ΔP_f and ΔP_b of each wind turbine are weighted according to its own power output, as shown in Fig. 5.6, so that the power reduction can be shared reasonably.

It should be noticed that when the grid fault is cleared, ΔP_b and ΔP_f are expected to be zero and the system should go back to normal operation. As the integrator is applied in the power controller 1 for producing ΔP_b, the reset signal is needed to make sure the ΔP_b restore to zero after fault cleared, which can be obtained according to the frequency error as shown in Fig. 5.6. When the grid fault is cleared, DC voltage of HVDC link will have a sudden dip due to the increased power transmission at the onshore grid, as a consequence the frequency error drops suddenly. Therefore, the reset signal of the integrator can be set to high level when the frequency error drops down under a certain value (0.2Hz in this study). To distinguish the frequency error drop caused by fault clearance from that caused by transient control progress, the reset signal is enabled after the minimum regulation time of the controller (0.2s in this study).

5.4.3 The fast power regulation on back-to-back converters

For the control system of the back-end converter, the fast power regulation is achieved through the power change added in the inner current control loop. Fig. 5.7 gives the improved control strategy of the back-end converter.

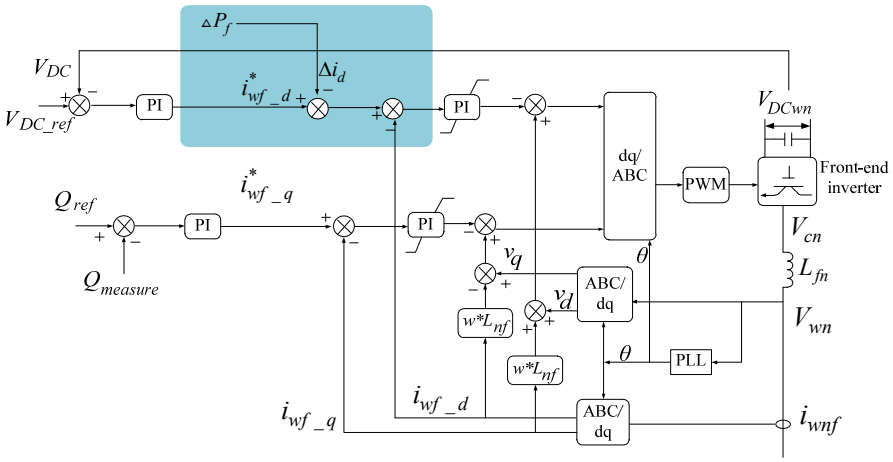

Fig. 5.7 Block diagram of proposed control scheme on front-end converter

The power reduction reference ΔP_b is added into the inner current control loop to realize the fast and effective power reduction under onshore grid fault, as shown in the shadow area in Fig. 5.7. Under normal operation, the ΔP_b is equal to zero and converter is controlled to tracking the maximum wind power. During the onshore grid fault situation, ΔP_b obtained according to the frequency error in Fig. 5.6 is introduced into inner current control loop by Δi to achieve the fast electrical torque reduction, i.e. the active power decrease. The Δi limit here is applied to avoid the unaccepted torque change for the generator.

On the other hand, for the front-end converter, the fast power regulation can also be realized through the change on power reference of inner current loop. Fig. 5.8 shows the improved control system of the front-end converter.

The power reduction reference ΔP_f is added into the d-axis inner current control loop to achieve the fast power regulation at the transient of onshore grid fault. Under normal operation, ΔP_f is zero and the converter is controlled to realize effective power deliver from the DC link to the offshore ac-bus. During fault transient, ΔP_f is obtained through the frequency change at offshore ac-bus and the equivalent current reference thus decreased, so that the power output drops down quickly.

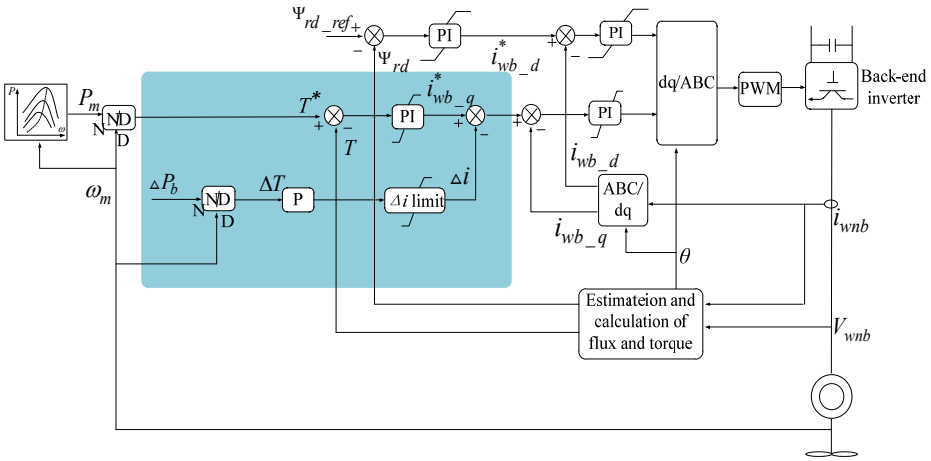

Fig. 5.8 Block diagram of proposed control scheme on front-end converter

5.5 Simulation study

The studied wind power system is modeled and simulated in PSCAD. The wind farm is rated as 300MW and presented by three parallel aggregated wind turbines. The system is firstly operating under steady state and then a grid fault occurs at the onshore system, which presented by a voltage drop at the infeed bus of HVDC link down to around 0.2pu. The fault occurs at 40s and last about 0.3s. In order to present the different regulation on wind power based on the proposed control method, the three wind turbines are assumed operation at different wind speed before the onshore grid fault. Table 5.3 gives the parameters and wind speed of the three wind turbines.

TABLE 5.3

PARAMETERS OF THE WIND TURBINES

Wind Turbine	Capacity	Wind speed	Active power output
1	100MVA	14m/s	100MW
2	100MVA	11m/s	75MW
3	100MVA	8m/s	35MW

Rated wind speed: 12m/s

In order to verify the enhancement on LVRT capability under proposed control method, the studied system is simulated under both the conventional control method and the proposed control scheme. Fig. 5.9 and Fig. 5.10 show the response of the system under conventional control and proposed control strategies, respectively.

Under the conventional control method, due to the onshore grid voltage drop, the active power from the onshore converter to the power system suddenly drops down. The voltage of offshore wind farm keeps constant because the SEC works as a voltage source. Without the power regulation in wind farm, the power keeps flowing from the wind farm to SEC. Consequently the DC voltage of HVDC link increases quickly. The large active power difference charges the DC capacitor and finally rises up the DC voltage to higher than 2.0 p.u., which is unacceptable to the DC link and the connected power electronics equipment. Hence with the conventional control method, the VSC-HVDC connected wind farm cannot ride through the onshore grid fault.

The simulation results for the same fault applied on the system using proposed control scheme are shown in Fig. 5.10. The increased DC voltage due to the power imbalance of HVDC is detected by the SEC and thus the frequency modulation is activated. The offshore wind farm frequency is raised and detected by each wind turbine, the power output of the wind farm (P_w) is reduced quickly along with the grid side power (P_{VSC}) decrease through the fast frequency controller. It can be found that the DC link voltage increase is restrained to only around 1.2p.u. through the fast reduction of wind power output. After the fault cleared, the frequency modulation on SEC is stopped and the wind farm power output restore to the pre-fault value.

As explained in subsection 5.4, under the proposed control method, the power reduction for each wind turbine is different according to its power output. Fig. 5.11 to Fig. 5.13 show the simulation results of the three equivalent wind turbines in the studied model. The active power of each wind turbine is different due to the different wind speed shown in Table 5.3.

With the different power output, the power reduction ΔP_f and ΔP_b for the back-to-back converters of each wind turbine are proportion to its own active power. For each wind turbine, it is obviously that the ΔP_b obtained through a PID controller goes to a stable value during the fault period, which represents the expected power reduction for keeping the DC link voltage of HVDC system. However,

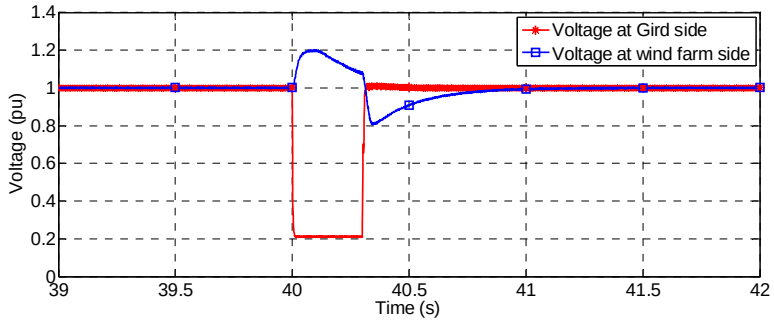

(a) AC voltages at SEC and REC

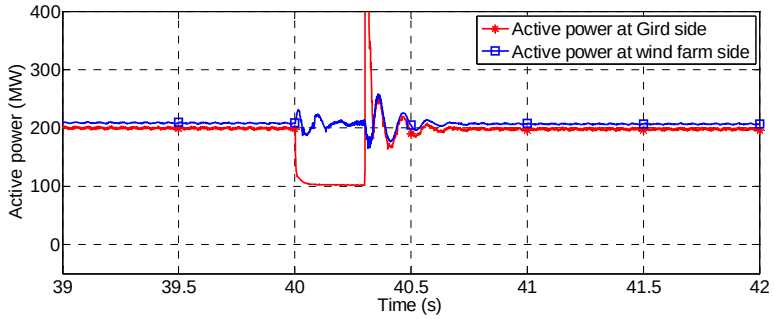

(b) Active power of

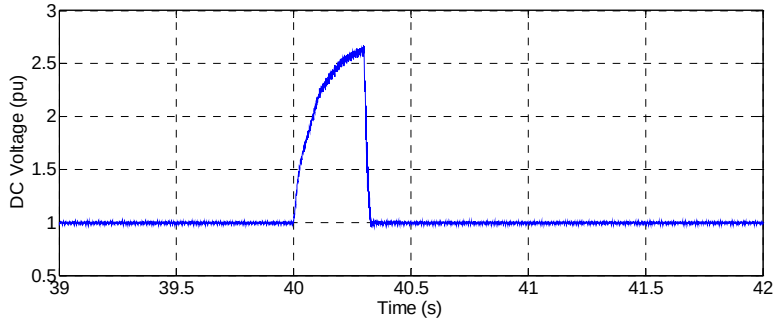

(c) DC voltage of HVDC

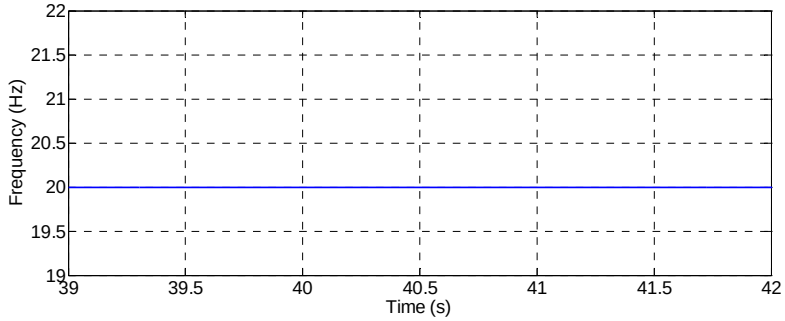

(d) Offshore wind farm frequency

Fig. 5.9 Simulation results during onshore grid fault under conventional control method.

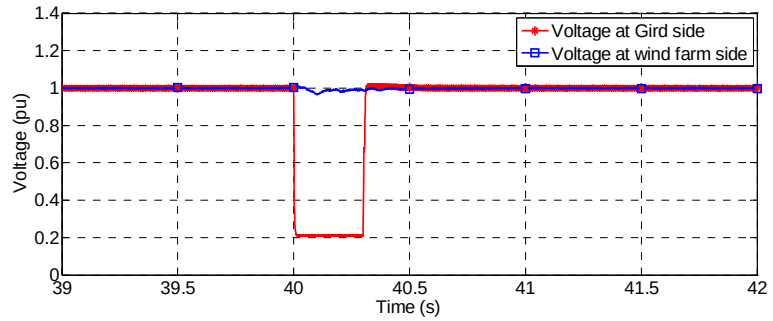

(a) AC voltages at SEC and REC

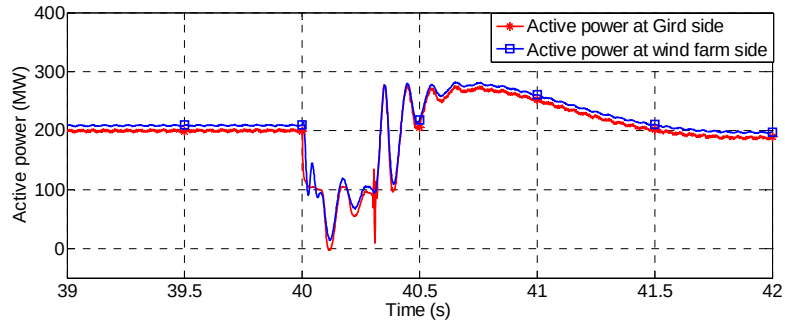

(b) Active power of

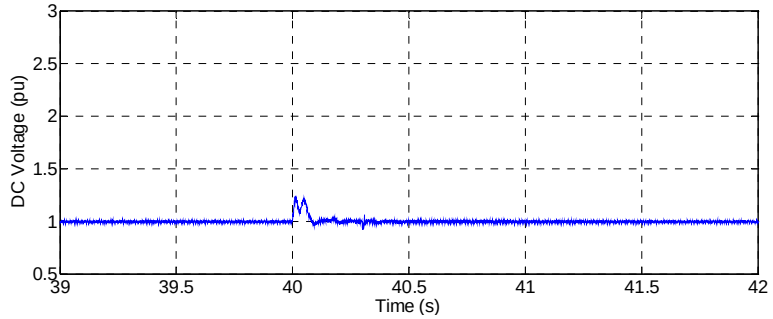

(c) DC voltage of HVDC

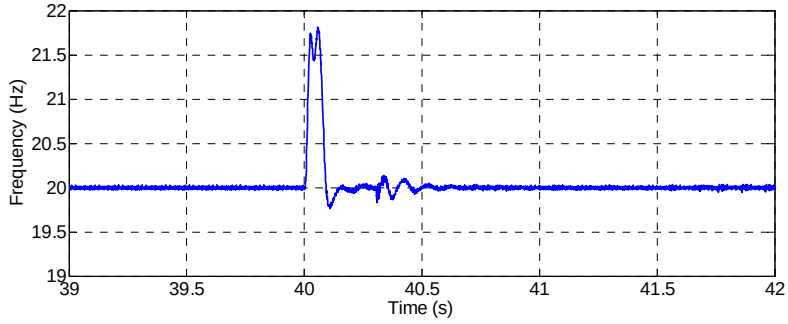

(d) Offshore wind farm frequency

Fig. 5.10 Simulation results during onshore grid fault under proposed control method.

the increasing rate of ΔP_b during the short transient after fault is not high enough, which cannot achieve the fast enough power reduction. The ΔP_f then covers the requirement of power reduction at this short time period.

From the simulation results in Fig. 5.11-Fig. 5.13, it can be found that the combination of ΔP_b and ΔP_f in the control system can achieve the optimum power reduction performance at each wind turbine.

As explained before, the power reduction ΔP_b is added directly in the torque control loop of back-end converter, which achieves the quickly drop of electrical torque of each wind generator during the fault period. However the mechanical torque is almost constant during the transient, the imbalance of electrical and mechanical torque thus increase the rotor speed of the wind turbine. In that way, the excess energy is converted to the kinetic energy on the wind turbine.

5.6 Summary

In this Chapter, a VSC-HVDC connected variable speed SCIG wind farm is studied and a control method aiming to improving the system LVRT capability is investigated. The proposed control strategy is developed for restraining the surge on DC voltage of the VSC-HVDC link under onshore grid voltage drop.

During the grid fault situation, the DC voltage increment is introduced into the HVDC offshore converter control loop, thus changed the offshore ac-bus frequency. Two power reduction references obtained based on the frequency error are added into the inner control loops of the back-to-back converters at each wind turbine to reduce the wind farm power output. The studied system is modeled and simulated in EMTDC/PSCAD. According to the simulation results, the proposed control scheme restrained the DC voltage of VSC-HVDC link effectively, and the system LVRT ability is improved.

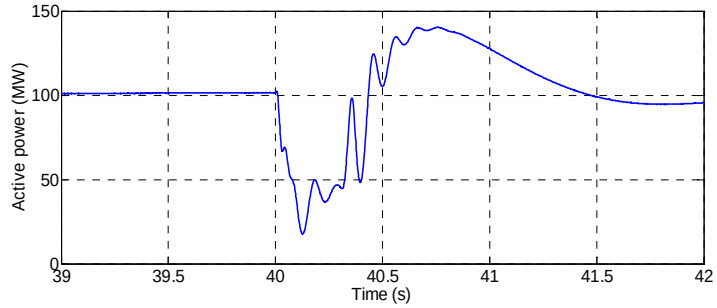

(a) Active power output

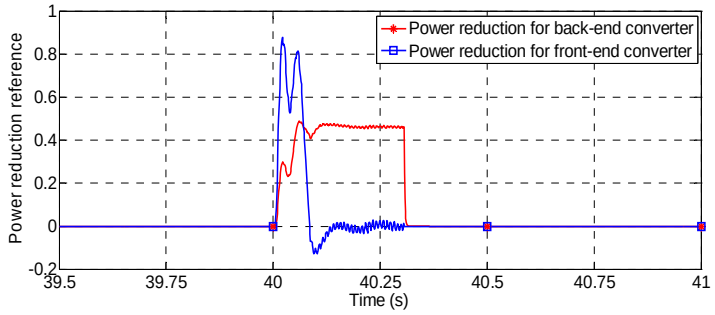

(b) Power reduction reference

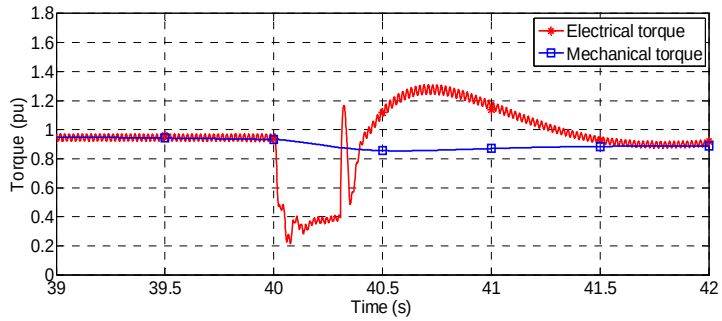

(c) Electrical and mechanical torque

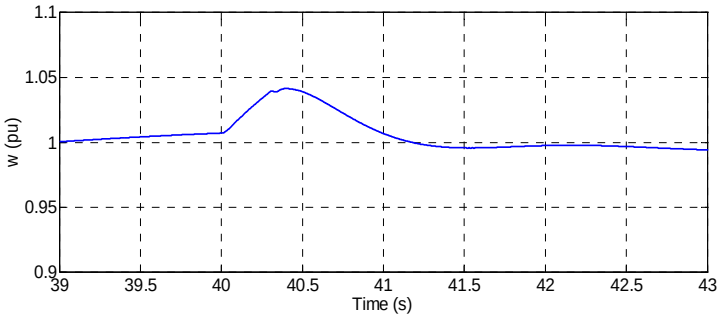

(d) Rotor speed

Fig. 5.11 Simulation results of wind turbine 1 under onshore grid fault.

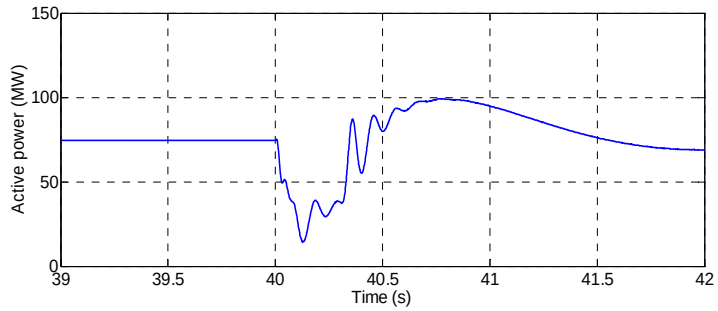

(a) Active power output

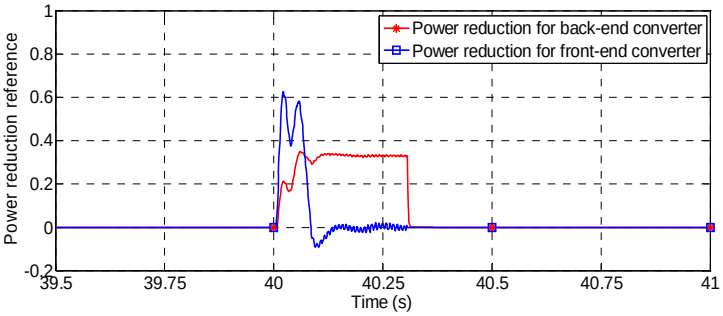

(b) Power reduction reference

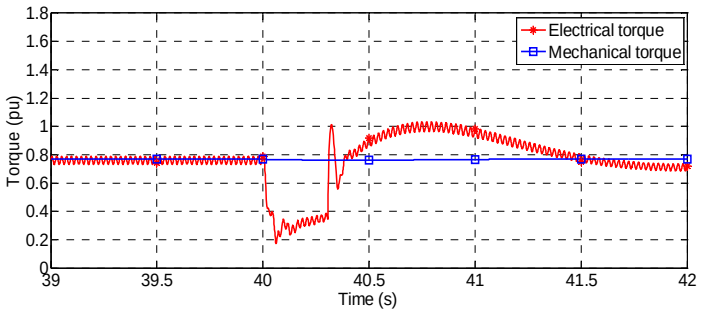

(c) Electrical and mechanical torque

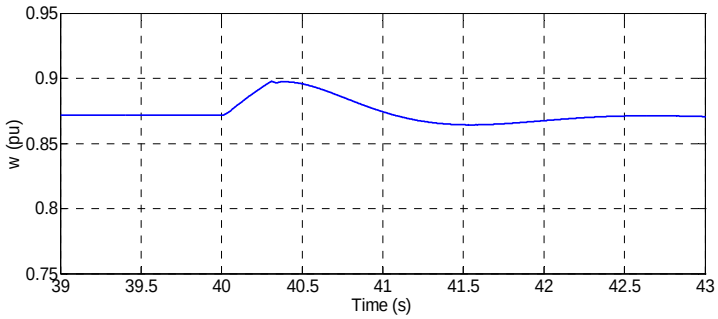

(d) Rotor speed

Fig. 5.12 Simulation results of wind turbine 2 under onshore grid fault.

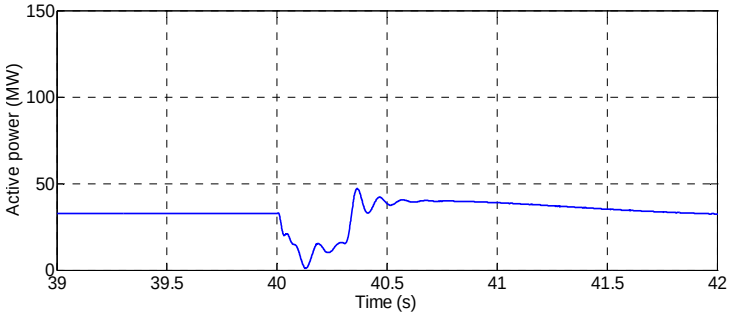

(a) Active power output

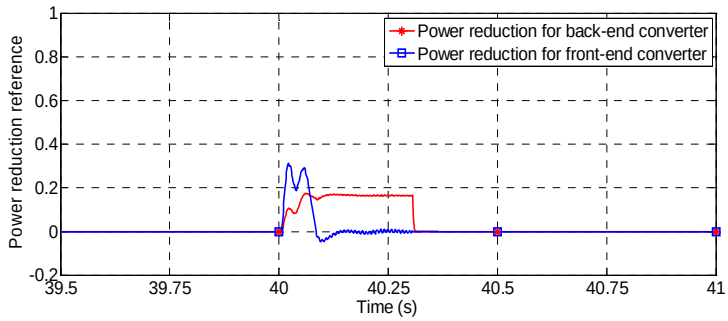

(b) Power reduction reference

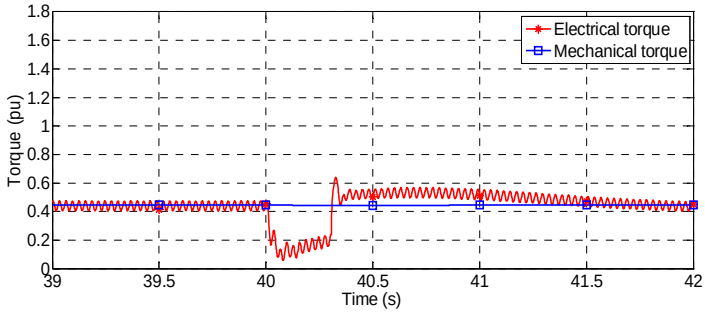

(c) Electrical and mechanical torque

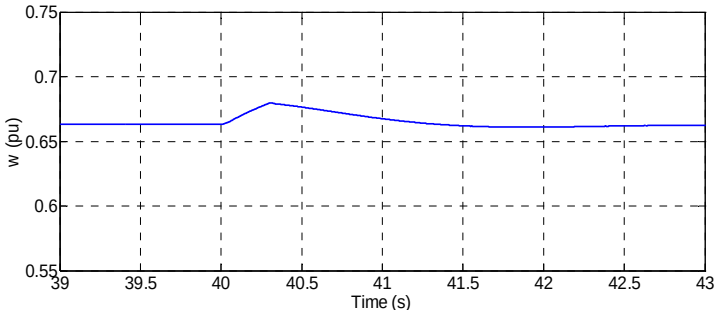

(d) Rotor speed

Fig. 5.13 Simulation results of wind turbine 3 under onshore grid fault.

Bibliography:

[1] K. H. Sobrink, P. L. Sorensen, P. Christensen, N. Sandersen, K. Eriksson, and P. Holmberg, "DC feeder for connection of a wind farm," in Proc. Cigré Symp., Sep. 1999.

[2] X. I. Koutiva, T. D. Vrionis, N. A. Vovos, and G. B. Giannakopoulos, "Optimal integration of an offshore wind farm to a weak AC grid," IEEE Trans. Power Del., vol. 21, no. 2, pp. 987–994, Apr. 2006.

[3] W. Lu and B. T. Ooi, "Optimal acquisition and aggregation of offshore wind power by multiterminal voltage-source HVDC," IEEE Trans. Power Del., vol. 18, no. 1, pp. 201–206, Jan. 2003.

[4] L. Xu and B. R. Andersen, "Grid connection of large offshore wind farms using HVDC," Wind Energy, vol. 9, no. 4, pp. 371–382, 2006.

[5] S. M. Muyeen, R. Takahashi, J. Tamura, "Operation and Control of HVDC-Connected Offshore Wind Farm," IEEE Trans. sustainable energy., vol. 1, no. 1, pp. 30-37, Apr. 2010.

[6] M. Tsili, S. Papathanassiou, "A review of grid code technical requirements for wind farms," IET Trans. Renewable Power Generation, vol. 3, no. 3, pp. 308-332, 2009.

[7] G. Ramtharan, O. Anya-Lara, and N. Jenkins, "Modelling and control of synchronous generators for wide-range variable-speed wind turbines," Wind Energy, vol. 10, no. 3, pp. 231–246, 2007.

[8] V. Akhmatov, A. Nielsen, J.K. Pedersen, O. Nymann, "Variable speed wind turbines with multi-pole synchronous permanent magnet generators. Part 1: modelling in dynamic simulation tools," Wind Eng., vol. 27, pp. 531–548, 2003.

[9] G. Ramtharan, A. Arulampalam, J.B. Ekanayake, F.M. Hughes, N. Jenkins "Fault ride through of fully rated converter wind turbines with AC and DC transmission systems," IET Trans. Renewable Power Generation, vol. 3, no.4, pp. 426-438, 2009.

[10] C. Feltes, H. Wrede, F. Koch, and I. Erlich, "Fault ride-through of DFIG-based wind farms connected to the grid through VSC-based HVDC link," in Proc. 16th Power System Computation Conference (PSCC'08), 2008.

[11] M. S. Vicatos and J. A. Tegopoulos, "Transient state analysis of a doubly-fed induction generator under three phase short circuit," IEEE Trans. Energy Convers., vol. 6, no. 1, pp. 62–68, Mar. 1991.

[12] I. Erlich et al., "Modeling of wind turbines based on doubly-fed induction generators for power system stability studies," IEEE Trans. Power Syst., vol. 22, no. 3, pp. 909–919, Aug. 2007.

[13] A. Arulampalam, G. Ramtharan, N. Caliao, J.B. Ekanayake, N. Jenkins, "Somulated onshore-fault ride through of offshore wind farms connected through VSC HVDC," Wind Eng., vol. 32, no. 2, pp. 103-114, 2008.

[14] L. Xu, L. Yao, C. Sasse, "Grid integration of large DFIG-based wind farms using VSC transmission," IEEE Trans. Power Syst., vol. 22, no. 3, pp. 976-984, 2007.

[15] S. M. Muyeen, M. H. Ali, R. Takahashi, T. Murata, J. Tamura, Y. Tomaki, A. Sakahara and E. Sasano, "Blade-shaft Torsional Oscillation Minimization of Wind Turbine Generator System by Using STATCOM/ESS," in Proc. 2007 IEEE Lausanne POWERTECH, pp.184-189.

[16] J. G. Slootweg, S. W. H. Haan, H. Polinder, and W. L. Kling, "General model for representing variable speed wind turbines in power system dynamics simulations," IEEE Trans. Power Syst., vol. 18, no. 1, pp. 144-151, Feb. 2003.

[17] E. Koutroulis and K. Kalaitzakis, "Design of a maximum power tracking system for wind-energy-conversion applications," IEEE Trans. Ind. Electron., vol. 53, no. 2, pp. 486-494, Apr. 2006.

[18] W. Qiao, R. G. Harley, and G. K. Venayagamoorthy, "Dynamic modeling of wind farms with fixed-speed wind turbine generators," in Proc. IEEE PES 2007 General Meeting., pp:1-8.

[19] M. J. Hossain, H. R. Pota, and V. A. Ugrinovskii, "Simultaneous STATCOM and pitch angle control for improved LVRT capability of fixed-speed wind turbines," IEEE Trans. Sustain. Energy, vol. 1, no. 3, pp. 142–151, Oct. 2010.

[20] P. Vas, Sensorless Vector and Direct Torque Control. New York: Oxford University Press, Inc., 1998, pp. 263-333.

[21] M. P. Kazmierkowski, L. Malesani, "Current Control Techniques for Three-Phase Voltage-Source PWM Converters: A Survey," IEEE Trans. Ind. Electron., vol. 45, no. 5, pp.691-703, Oct. 1998.

Chapter 6

Improved reactive power control of VSC-HVDC based on voltage sensitivity analysis in the HMIDC system with offshore wind farm

6.1 Introduction

Besides the LVRT ability of the wind farm, the wind power fluctuation during the normal operation is also an important issue which may take influence to the system stability. Hence for the studied HMIDC system connecting with offshore wind farm, some effort is essential to be made on the study of influence to AC system stability by the wind power fluctuation.

It is known that the variable nature of the wind speed will lead to the fluctuations in electrical variables, which consequently affect the power quality [1], [2], bring the bus voltages variations [3]. Note that the stable operation of LCC-HVDC link is highly dependent on its ac side voltage [4]. The voltage fluctuation at the infeed bus of LCC-HVDC link may lead to the commutation failures on the converters of HVDC link and even large voltage drop at the bus. Therefore, considering a wind farm connected HMIDC system, the influence of wind power variation to the voltage at infeed bus of LCC-HVDC link plays an important role to the system voltage stability.

Over the last years, a number of research efforts have been made on the study of wind farm integration through VSC-HVDC links. Thanks to the flexible power control ability of the VSC-HVDC link, the reactive power output can be controlled in different way according to different system requirements. In [5], a certain value of reactive power reference is adopted in the control loop of VSC-HVDC to realize a constant reactive power output from HVDC to the grid. On the other hand,

wind energy systems are expected to operate under the power factors greater than 0.95 through FERC 661-A [6], hence many wind power operators prefer unity power factor operation[7]. The unity power factor can be achieved in the VSC-HVDC link by a variable reactive power reference proportion to its active power delivery. However, in the above control methods, the influence to system voltage at other buses by the infeed wind power variation is not considered. Thus for a HMIDC system, an improved reactive power control method is expected to constrain the voltage fluctuation on infeed bus of LCC-HVDC link under the wind power variation. Notice that the onshore VSC station also can be controlled as a voltage source through the voltage control method in [8], which supply another option of VSC-HVDC control method for supporting the system voltage.

In this chapter, a reactive power control method on VSC-HVDC link is proposed based on the voltage sensitivity analysis in order to mitigate the voltage variations at a target bus in the system caused by the wind power fluctuation. The control scheme provides variable reactive power references according to the active power delivered from the wind farm by HVDC link and the system voltage sensitivity factors. And the verification of the control method is carried out using the dynamic simulations in PSCAD together with MATAB.

6.2 The Voltage sensitivity analysis in power system with wind power integration

In a power system, the current injected into bus i can be given in terms of the bus admittance matrix,

$$I_i = \sum_{j=1}^{n} Y_{ij} V_j \tag{6.1}$$

where V_j is the voltage at bus j and Y_{ij} is the system admittance matrix. The current equation can be expressed in polar form as

$$I_i = \sum_{j=1}^{n} \left|Y_{ij}\right|\left|V_j\right| \angle \theta_{ij} + \delta_j \tag{6.2}$$

where θ_{ij} is the voltage angle difference that bus i leading bus j, δ_j is the phase angle of voltage at bus j . The complex power at bus i can be expressed as

$$P_i - jQ_i = V_i^* I_i \tag{6.3}$$

Substituting (6.2) into (6.3) and separating the real and imaginary parts, it can be obtained that,

$$P_i = \sum_{j=1}^{n} |V_i||V_j||Y_{ij}|\cos(\theta_{ij} - \delta_i + \delta_j) \tag{6.4}$$

$$Q_i = -\sum_{j=1}^{n} |V_i||V_j||Y_{ij}|\sin(\theta_{ij} - \delta_i + \delta_j) \tag{6.5}$$

where P_i and Q_i are the active and reactive power of bus i. Equations (6.4) and (6.5) are the power flow equations for a power system. Expending (6.4) and (6.5) in Taylor's series and neglecting all higher order terms, the small changes in active and reactive power due to the small changes in voltage angle and magnitude can be expressed through the Jacobian matrix as

$$\begin{bmatrix} \Delta P_1 \\ \Delta Q_1 \\ \vdots \\ \Delta P_i \\ \Delta Q_i \\ \vdots \\ \Delta P_j \\ \Delta Q_j \\ \vdots \end{bmatrix} = \begin{bmatrix} \frac{\partial P_1}{\partial \delta_1} & \frac{\partial P_1}{\partial V_1} & \cdots & \frac{\partial P_1}{\partial \delta_i} & \frac{\partial P_1}{\partial V_i} & \cdots & \frac{\partial P_1}{\partial \delta_j} & \frac{\partial P_1}{\partial V_j} & \cdots \\ \frac{\partial Q_1}{\partial \delta_1} & \frac{\partial Q_1}{\partial V_1} & \cdots & \frac{\partial Q_1}{\partial \delta_i} & \frac{\partial Q_1}{\partial V_i} & \cdots & \frac{\partial Q_1}{\partial \delta_j} & \frac{\partial Q_1}{\partial V_j} & \cdots \\ \vdots & \vdots & & \vdots & \vdots & & \vdots & \vdots & \\ \frac{\partial P_i}{\partial \delta_1} & \frac{\partial P_i}{\partial V_1} & \cdots & \frac{\partial P_i}{\partial \delta_i} & \frac{\partial P_i}{\partial V_i} & \cdots & \frac{\partial P_i}{\partial \delta_j} & \frac{\partial P_i}{\partial V_j} & \cdots \\ \frac{\partial Q_i}{\partial \delta_1} & \frac{\partial Q_i}{\partial V_1} & \cdots & \frac{\partial Q_i}{\partial \delta_i} & \frac{\partial Q_i}{\partial V_i} & \cdots & \frac{\partial Q_i}{\partial \delta_j} & \frac{\partial Q_i}{\partial V_j} & \cdots \\ \vdots & \vdots & & \vdots & \vdots & & \vdots & \vdots & \\ \frac{\partial P_j}{\partial \delta_1} & \frac{\partial P_j}{\partial V_1} & \cdots & \frac{\partial P_j}{\partial \delta_i} & \frac{\partial P_j}{\partial V_i} & \cdots & \frac{\partial P_j}{\partial \delta_j} & \frac{\partial P_j}{\partial V_j} & \cdots \\ \frac{\partial Q_j}{\partial \delta_1} & \frac{\partial Q_j}{\partial V_1} & \cdots & \frac{\partial Q_j}{\partial \delta_i} & \frac{\partial Q_j}{\partial V_i} & \cdots & \frac{\partial Q_j}{\partial \delta_j} & \frac{\partial Q_j}{\partial V_j} & \cdots \\ \vdots & \vdots & & \vdots & \vdots & & \vdots & \vdots & \end{bmatrix} \begin{bmatrix} \Delta \delta_1 \\ \Delta V_1 \\ \vdots \\ \Delta \delta_i \\ \Delta V_i \\ \vdots \\ \Delta \delta_j \\ \Delta V_j \\ \vdots \end{bmatrix} \tag{6.6}$$

In order to get the voltage variation caused by the power fluctuation, Inversing the Jacobian matrix and the system voltage change thus can be given by

$$\begin{bmatrix} \Delta\delta_1 \\ \Delta V_1 \\ \vdots \\ \Delta\delta_i \\ \Delta V_i \\ \vdots \\ \Delta\delta_j \\ \Delta V_j \\ \vdots \end{bmatrix} = \begin{bmatrix} S_{\delta P_{11}} & S_{\delta Q_{11}} & \cdots & S_{\delta P_{1i}} & S_{\delta Q_{1i}} & \cdots & S_{\delta P_{1j}} & S_{\delta Q_{1j}} & \cdots \\ S_{VP_{11}} & S_{VQ_{11}} & \cdots & S_{VP_{1i}} & S_{VQ_{1i}} & \cdots & S_{VP_{1j}} & S_{VQ_{1j}} & \cdots \\ \vdots & \vdots & & \vdots & \vdots & & \vdots & \vdots & \\ S_{\delta P_{i1}} & S_{\delta Q_{i1}} & \cdots & S_{\delta P_{ii}} & S_{\delta Q_{ii}} & \cdots & S_{\delta P_{ij}} & S_{\delta Q_{ij}} & \cdots \\ S_{VP_{i1}} & S_{VQ_{i1}} & \cdots & S_{VP_{ii}} & S_{VQ_{ii}} & \cdots & S_{VP_{ij}} & S_{VQ_{ij}} & \cdots \\ \vdots & \vdots & & \vdots & \vdots & & \vdots & \vdots & \\ S_{\delta P_{j1}} & S_{\delta Q_{j1}} & \cdots & S_{\delta P_{ji}} & S_{\delta Q_{ji}} & \cdots & S_{\delta P_{jj}} & S_{\delta Q_{jj}} & \cdots \\ S_{VP_{j1}} & S_{VQ_{j1}} & \cdots & S_{VP_{ji}} & S_{VQ_{ji}} & \cdots & S_{VP_{jj}} & S_{VQ_{jj}} & \cdots \\ \vdots & \vdots & & \vdots & \vdots & & \vdots & \vdots & \end{bmatrix} \begin{bmatrix} \Delta P_1 \\ \Delta Q_1 \\ \vdots \\ \Delta P_i \\ \Delta Q_i \\ \vdots \\ \Delta P_j \\ \Delta Q_j \\ \vdots \end{bmatrix} \tag{6.7}$$

According to (6.7), it is easy to find the relationship of power change and voltage fluctuation through the terms in the inversed Jacobian matrix. $S_{\delta P}$ and $S_{\delta Q}$ are the sensitivities of bus voltage angle to the active and reactive power, and S_{VP} and S_{VQ} are the sensitivities of bus voltage magnitude to the active and reactive power, respectively.

6.3 Voltage sensitivity based reactive power control on VSC-HVDC to improve system voltage stability

The studied HMIDC system model with offshore wind farm is presented below, as shown in Fig. 6.1. The wind power is integrated into the AC system through VSC-HVDC link. The BUS5 in Fig.6.1 is modeled as a slack bus here in order to supply the reference value of system phase angle (0 degree) when calculate the sensitivity factors.

According to the voltage sensitivity analysis in last subsection, the bus voltage variation due to the power fluctuation can be presented through the sensitivity factors. Assuming the target bus which is supposed to be regulated is bus *i* and the wind power inject into the system through bus *j*. The voltage variations at bus *i* due to the power variation at bus *j* can be obtained from (6.7) and given by

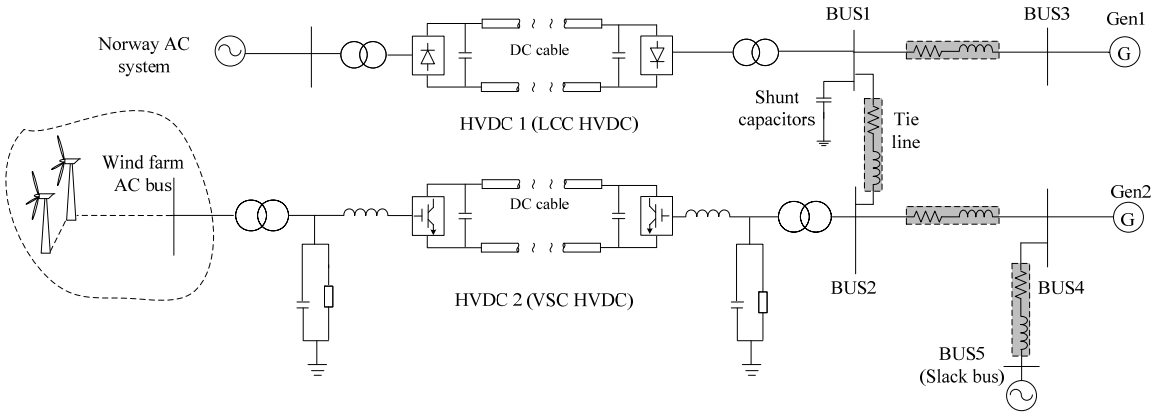

Fig. 6.1. Wind farm connected HMIDC system model

$$\Delta V_i = S_{VP_{ij}} \Delta P_j + S_{VQ_{ij}} \Delta Q_j \tag{6.8}$$

where S_{VPij} and S_{VQij} are the sensitivities of voltage at bus i to the changes of active and reactive power at bus j.

Appling the above equations in the studied HMIDC system in Fig. 6.1, the voltage change at infeed bus of LCC-HVDC link (BUS1) due to the fluctuating wind power injection through the infeed bus of VSC-HVDC link (BUS2) can be obtained as

$$\Delta V_{LCC} = S_{VP_{12}} \Delta P_{VSC} + S_{VQ_{12}} \Delta Q_{VSC} \tag{6.9}$$

As explained in previous chapters, for the LCC-HVDC link, the voltage fluctuation at AC bus takes adverse effect on its stable operation as well as the system voltage stability. Therefore, the voltage change ΔV_{LCC} is expected to be zero during the wind power fluctuating. Then set ΔV_{LCC} equal to zero in (6.9), the expected reactive power change of VSC-HVDC thus can be derived as

$$\Delta Q_{VSC} = -\frac{S_{VP_{12}}}{S_{VQ_{12}}} \Delta P_{VSC} \tag{6.10}$$

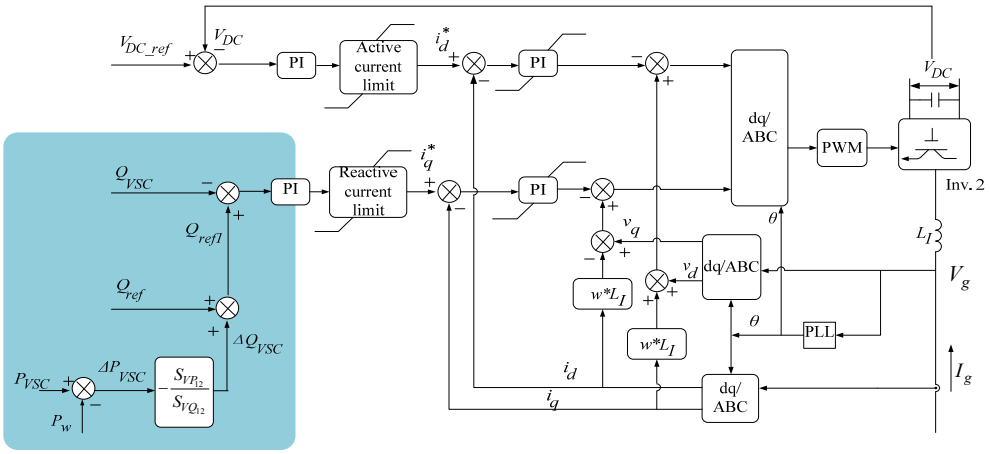

Fig. 6.2. Voltage sensitivity based reactive power control method on VSC

According to (6.10), in order to keep the voltage constant at BUS1, a reactive power increment, ΔQ_{VSC} can be added in the power control loop of the VSC-HVDC link. Fig. 6.2 gives the proposed reactive power control scheme of VSC-HVDC based on the voltage sensitivity.

It can be seen from Fig.6.2 that the voltage sensitivity based reactive power control method is based on the sensitivity factors in (6.10). To calculate these sensitivity factors, the system variables at each bus should be detected firstly. The partial derivatives in (6.6) can be obtained through (6.4) and (6.5) with voltages and phase angles of the buses. For simplicity, the terms in Jacobian matrix can be seen as constant values which calculated according to the system variables under the rated power flow situation. As a consequence, the voltage sensitivity factors in (6.10) would be fixed values.

It is worthy to note that the above simplified method ignores the influence of the changes on system voltages and phase angles to the sensitivity factors. To realize a more accurate voltage regulation on the target bus, the sensitivity factors should be obtained according to the system variables in real-time. The voltages and phase angles of buses can be sampled and delivered to the control system of VSC-HVDC link in each system cycle, so that the sensitivity factors are derived through system status in real-time and the more accurate reactive power increment ΔQ_{VSC} is obtained.

6.4 Combined simulation study based on EMTDC/PSCAD and MATAB

The proposed reactive power control method on VSC- HVDC is verified by the simulation study in EMTDC/PSCAD and MATLAB. The HMIDC system shown in Fig. 6.1 is modeled in PSCAD and the calculation program of sensitivity factors based on (6.6) and (6.7) is compiled in MATLAB. The system parameters applied in the simulation study can be found in Table 6.1.

Note that the influence of wind farm to the onshore AC system concerned in this chapter is the voltage variation caused by the wind power fluctuation. Therefore, the offshore wind farm can be replaced by a variable power source in the studied HMIDC system, which can supply the fluctuated active power according to the wind speed variation. In the simulation study, the wind speed is assumed fluctuating between 8m/s to 11m/s, the wind power output from the wind generator based on the different wind speed can be obtained through the lookup table. Since the power fluctuation caused by the wind speed variation is the main concern in this paper, the influence of tower shadow and wind shear are ignored.

Simulations are investigated under four cases below in which different reactive power control methods are applied on the VSC-HVDC link:

1) Fixed reactive power control
2) Fixed power factor control
3) Voltage sensitivity based reactive power control with constant sensitivity factors
4) Voltage sensitivity based reactive power control with time-variable sensitivity factors.

In order to get the time-varying sensitivity factors in case 4, the interface for connecting MATAB is built in PSCAD. The sample frequency in MATLAB is 50Hz. In each sample cycle, the system state variables are transferred to MATLAB and the calculated sensitivity factors based on those system variables are delivered back from MATLAB to PSCAD through the interface.

To verify the control method under severe wind conditions, the wind speed in the simulation study is assumed fluctuating wildly and frequently. Fig. 6.3 gives the curve of assumed wind speed applied

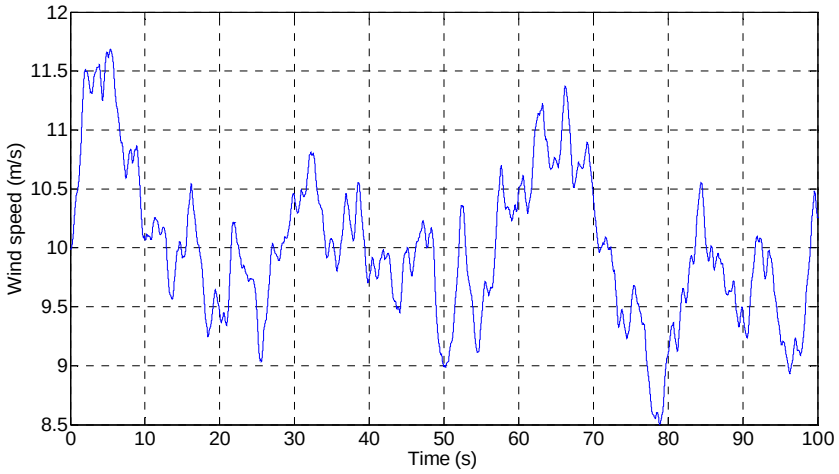

Fig.6.3. Wind speed applied in the simulation study

TABLE 6.1

AC NETWORK PARAMETERS

Parameters	**Values**	
Frequency	50Hz	
Rated (base)voltage	400kV	
Capacity of Gen1 and Gen2	500MVA	
Load at BUS1	900MW, 150MVar	
Load at BUS2	660MW, 0MVar	
Load at BUS3	150MW, 90MVar	
Load at BUS4	180MW, 120MVar	
Transmission line distance	Between BUS1 and BUS3	110km
	Between BUS2 and BUS4	100km
	Between BUS1 and BUS2	70km
	Between BUS4 and BUS5	200km

in the simulation study. The reactive power reference in VSC-HVDC control system is set as 0.1pu in case 1. In case 2, the constant power factor is assumed as 0.97, thus reactive power reference is equal to 0.25 times of the active power delivered. Under case 3 and case 4, the reactive power increments,

ΔQ_{VSC}, derived according to the constant or time-variable voltage sensitivity factors are added to the reactive power reference as shown in Fig. 6.2, respectively.

With the system parameters in Table 6.1, the constant voltage sensitivity factors in case 3 can be calculated through (6.6) and (6.7) under the rated power flow situation, then the ratio of the two sensitivity factors in (6.10) is derived as 0.08, thus the reactive power increment in (6.10) can be obtained as

$$\Delta Q_{VSC} = Q_{VSC} - Q_0 = -0.08(P_{VSC} - P_0) \tag{6.11}$$

where Q_0 and P_0 are the initial reactive and active power output of VSC-HVDC. The initial set point is chosen at Q_0=0.1 pu and P_0=P_w, where P_w is the average of the wind power, 400MW. Then the reactive power adjustment for voltage regulation at LCC-HVDC infeed bus is given by

$$Q_{VSC} = -0.08(P_{VSC} - P_w) + 0.1 \tag{6.12}$$

The different reactive power references under the four cases above are summarized in Table 6.2.

The simulations are carried out for 100s under each case. Fig. 6.4 shows the simulation curves of voltages at BUS1 under the four cases. To compare the voltage performance under proposed control method with fixed and variable sensitivity factors more clearly, the BUS1 voltages in case3 and case4 are redrawn in Fig. 6.5. The maximum and minimum values of the voltages during simulation time

TABLE 6.2

REACTIVE POWER REFERENCES UNDER THE DIFFERENT CASES

Cases	**Discriptions**	**Reactive power reference**
Case 1	Fixed Q control	Q_{ref} = 0.1 pu
Case 2	Fixed PF control	Q_{ref} = 0.25 P_{VSC}
Case 3	Voltage sensitivity based Q control with fixed sensitivity factors	Q_{ref} = 0.1-0.08(P_{VSC}-P_w)
Case 4	Voltage sensitivity based Q control with variable sensitivity factors	$Q_{ref} = -\frac{S_{VP_{12}}}{S_{VQ_{12}}}(P_{VSC} - P_w) + 0.1$

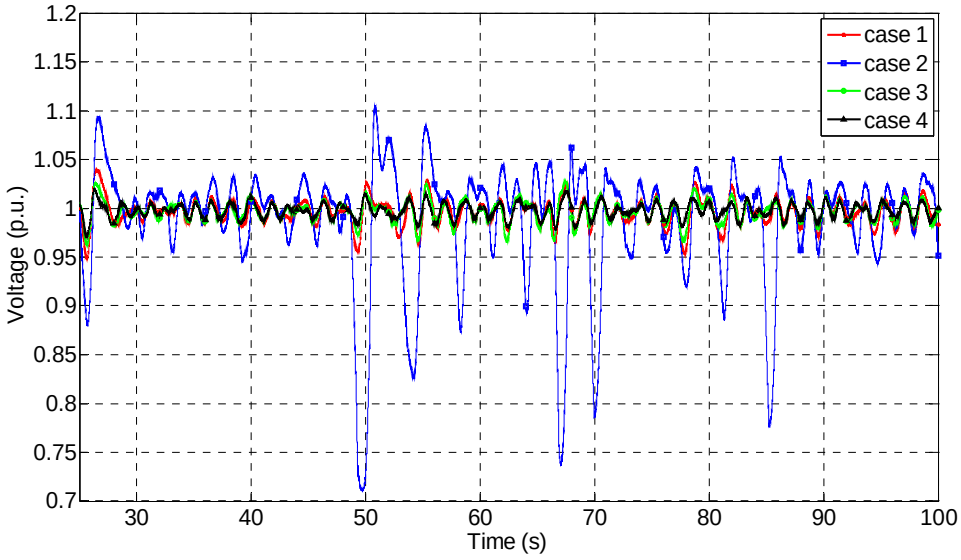

Fig. 6.4. Voltage at BUS 1 under the different control methods

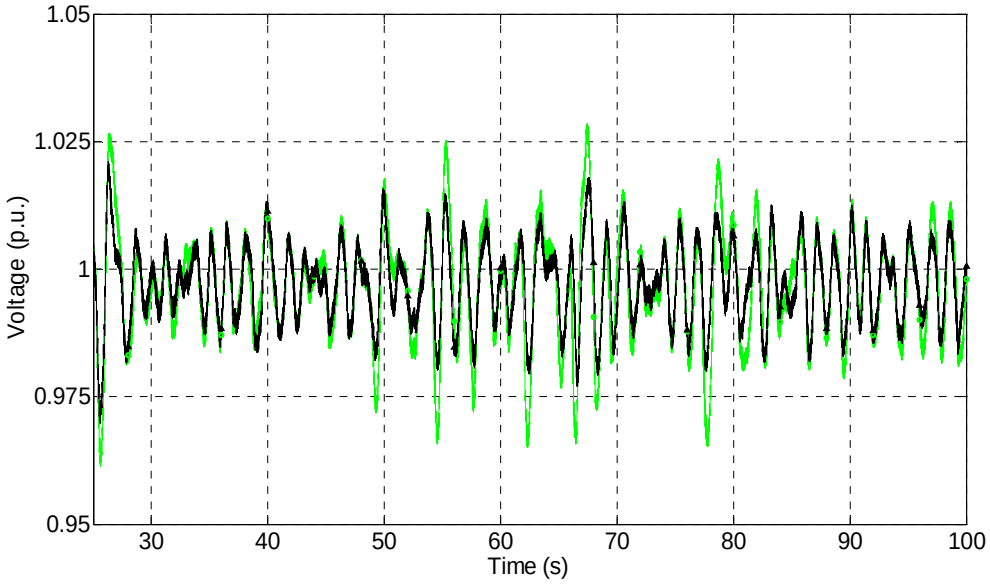

Fig. 6.5. Voltage at BUS 1 under case3 and case4

and the maximum fluctuations of the voltage under each reactive power control mode are summarized in Table. 6.3. It can be found that under the fixed power factor method, the voltage fluctuation of BUS1 achieves 39.41%, which is the highest one in the four control modes. The voltage fluctuation is reduce to about 8.78% under fixed reactive power control mode, whereas it can be further decreased until 6.7% and even 5% through the proposed voltage sensitivity based control method with fixed and time-variable sensitivity factors, respectively.

The wind power fluctuation can be represented by the active power output of VSC-HVDC link and would be the same under the different cases. Fig. 6.6 gives the curve of active power injection from VSC-HVDC to the grid under the wind speed condition in Fig. 6.3. Under the different control methods, Fig. 6.7 presents the reactive power output curves of the VSC-HVDC link, Q_{vsc} in the four cases.

As shown in Fig. 6.7, under the constant reactive power control method, the Q_{vsc} is controlled around the reference value, 0.1 pu. In case 2, the reactive power reference is changed according to the active power fluctuation to achieve a constant power factor, thus the Q_{vsc} vary similarly with the active power in Fig. 6.6. For the reactive power control method based on (6.11), the Q_{vsc} in case 3 is changed according to the fixed sensitivity factors and variable active power output of VSC-HVDC. Correspondingly, the Q_{vsc} in case 4 varying based on the active power of VSC-HVDC and the time-variable sensitivity factors calculated in MATLAB.

TABLE 6.3

THE MAXIMUM VOLTAGE FLUCTUATIONS UNDER DIFFERENT CASES

Cases	**Maximum values**	**Minimum values**	**Largest fluctuation**
Case 1	1.04	0.9522	8.78%
Case 2	1.105	0.7109	39.41%
Case 3	1.029	0.962	6.7%
Case 4	1.02	0.97	5%

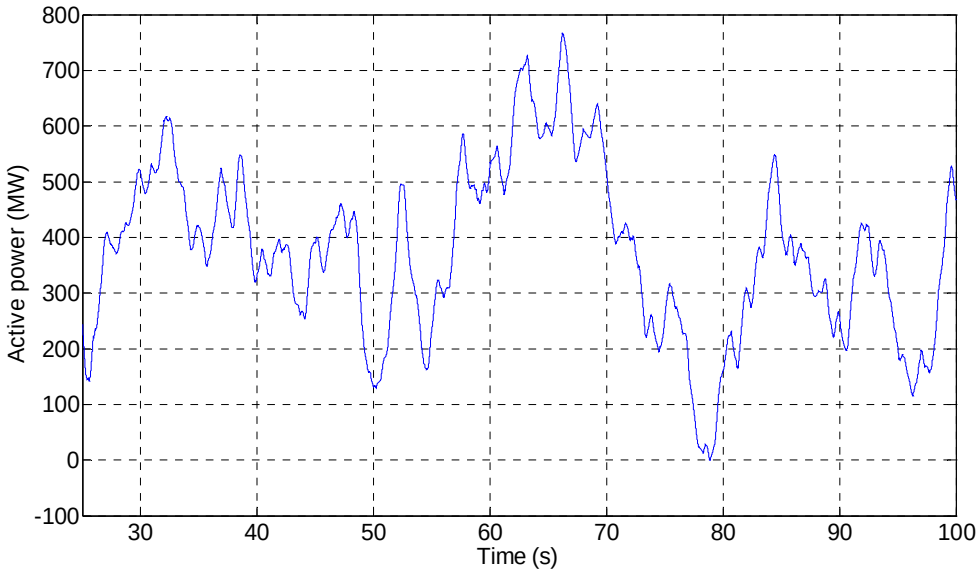

Fig. 6.6. Active power output of VSC-HVDC

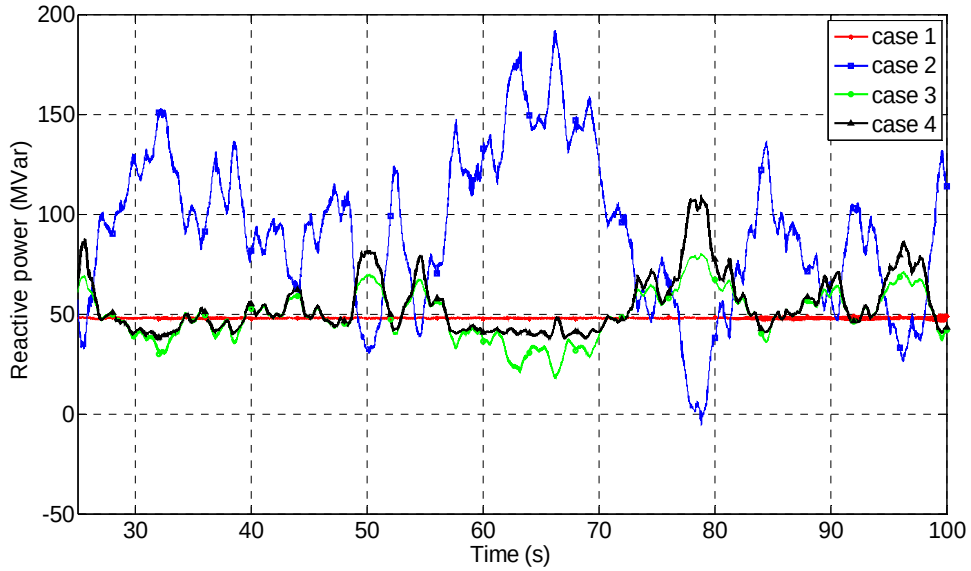

Fig. 6.7. Reactive power output of VSC-HVDC

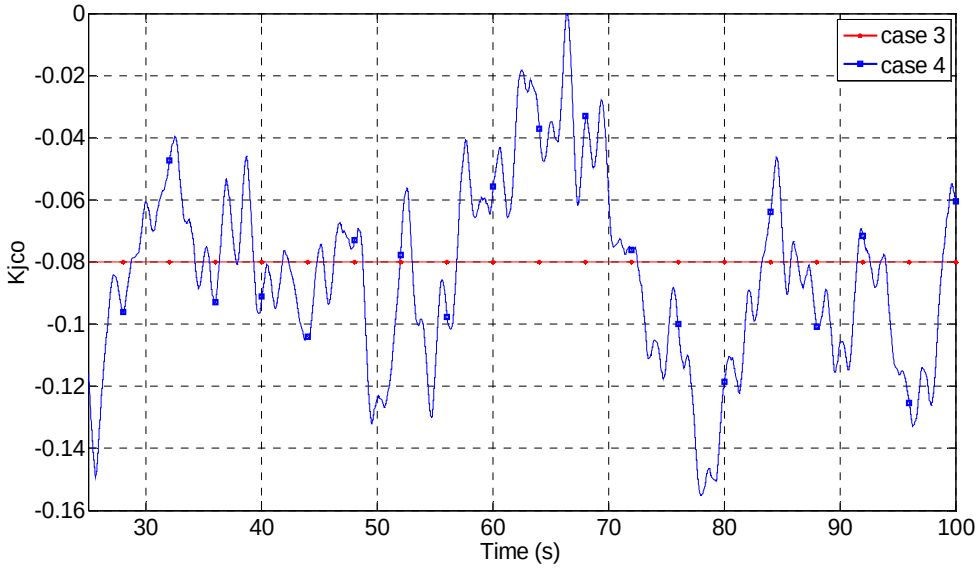

Fig. 6.8. Sensitivity factor in case3 and case4

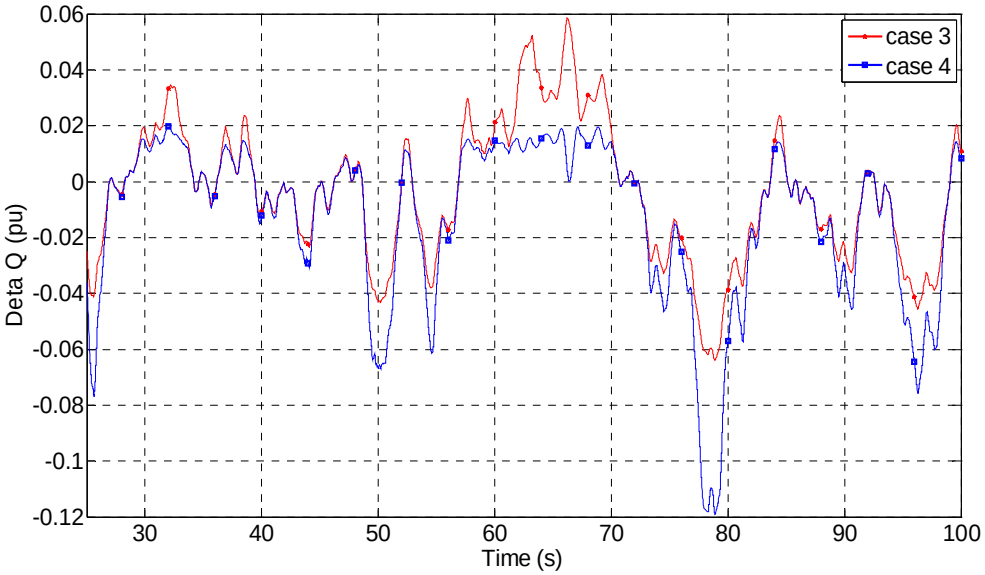

Fig. 6.9. Added reactive power ΔQ_{VSC} under case3 and case4

The fixed and time-variable sensitivity factors during the wind power fluctuation in case 3 and case 4 are shown in Fig. 6.8 as K_{jco}, where

$$K_{jco} = -\frac{S_{VP_{12}}}{S_{VQ_{12}}} \tag{6.13}$$

With the different sensitivity factors, the reactive power increment ΔQ_{VSC} in Fig. 6.2 are different. Fig. 6.9 gives the simulation results of ΔQ_{VSC} in these two cases.

From the simulation results, it can be seen that the voltage sensitivity based reactive power control can reduce the voltage fluctuation caused by wind power variation at target bus effectively. Moreover, comparing the system performances in case 3 and case 4, with different calculation method of sensitivity factors, the extent of voltage fluctuation reduction is different. It is obviously that the control method with time- variable sensitivity factors achieves more accurate voltage regulation on the target bus.

6.5 Summary

In this chapter, a wind farm connected HMIDC system is studied and the reactive power control method aiming to regulating the system voltage at target bus is investigated. The proposed control strategy is based on the voltage sensitivity analysis of the HMIDC system. The required reactive power change for keeping the bus voltage constant is calculated through the sensitivity factors and added in the power control loop of VSC-HVDC link. Consequently the voltage fluctuation caused by the wind power variation at target bus is reduced effectively. The studied system is modeled and simulated in EMTDC/PSCAD together with MATLAB. According to the simulation results, the voltage fluctuation at BUS1 in the system is decreased a lot under the proposed control method compared with the conventional control schemes.

Moreover, two different cases are considered in the proposed control method: with the fixed sensitivity factors obtained through the initial system status and with the time-varying sensitivity factors derived from the system variables in each sample cycle. Simulation results show that the

different reactive power output of VSC-HVDC in these two cases result in different voltage performances. Compare to the situation with fixed sensitivity factors, the voltage of target bus is regulated more accurately and performs smaller fluctuation under the control method with time-varying sensitivity factors.

Bibliography:

[1] T. Sun, Z. Chen, and F. Blaabjerg, "Flicker study on variable speed wind turbines with doubly fed induction generators," IEEE Trans. on Energy Conversion, vol. 20(4), 2005, pp. 896–905.

[2] Y. S. Kim and D. J. Won, "Mitigation of the flicker level of a DFIG using power factor angle control," IEEE Trans. on Power Delivery, vol. 24(4), 2009, pp. 2457–2458.

[3] A. Larsson, "Flicker emission of wind turbines during continuous operation," IEEE Trans. on Energy Conversion, vol. 17(1), 2002, pp. 114–118.

[4] B.R. Andersen, X. Lie, "Hybrid HVDC system for power transmission to island networks," IEEE Trans. on Power Delivery, Vol. 19(4), 2004, pp. 1884-1890.

[5] T.M. Haileselassie, R.E. Torres-Olguin, T.K. Vrana, K. Uhlen, T. Undeland, "Main grid frequency support strategy for VSC-HVDC connected wind farms with variable speed wind turbines," IEEE Trondheim PowerTech, 2011, pp. 1-6.

[6] Standard Interconnection Agreements for Wind Energy and Other Alternative Technologies Federal Energy Regulatory Commission (FERC), Washington, DC, 661-A, Dec. 2005.

[7] B. Kroposki, R. DeBlasio, and M. Simoes, "Benefits of power electronic interfaces for distributed energy systems," IEEE Trans. on Energy Conversion, vol. 25(3), 2010, pp. 901–908.

[8] J. Kang; H. Liang; G. Li, M. Zhou. H. Yang, "Research on grid connection of wind farm based on VSC-HVDC," Power System Technology (POWERCON), 2010 International Conference, pp. 1-6.

Chapter 7

Conclusions

7.1 Summary

The wind power development brings new challenges to today's power systems. And with the increasing application of HVDC links for wind power integration, many different system structures can be anticipated in the future modern power system. Therefore, the main concern of this project is about the study on a new power system structure which is named as HMIDC system in the thesis and the research objective of the project is focus on the HMIDC system stability.

According to the research problems stated in Chapter1, the scope of the project is divided into two parts: 1) the stability analysis of the AC system applying different HVDC links, and 2) the development of the control strategies on VSC-HVDC and offshore wind farm. The research works of this project are presented in the thesis by 5 Chapters (Chapter2-Chapter6) corresponds to the main tasks listed in Chapter 1.

The stability of HMIDC system mainly can be affected by several factors below:

1) The AC system parameters.
2) The HVDC links.
3) The wind power fluctuation caused by the integrated wind farm.
4) Low voltage ride through ability of the connected wind farm

In order to assess the influence to the system by those factors and enhance the system stability, the system performances are analyzed considering the above influences under different fault situations. And the corresponding control improvement has been made for each stability problem caused by the influence factors.

Before the detailed analysis on system stability and control improvement, the HMIDC system model is firstly established based on the western Danish power system. In the studied HMIDC system model, two different HVDC links, i.e. the LCC-HVDC and the VSC-HVDC are connecting to the same AC system which presented by interconnected synchronous generators. The transmission lines in the grid are modeled as 400kV AC lines, as well as the tie line between two infeed buses of the HVDC links.

It is easy to know that in a power system with VSC-HVDC link, the flexible power control on the VSC-HVDC can supply the voltage support to the AC system. On the other hand, the parameters of the AC system, such as transmission line distance and generator capacity also take large influence to the system voltage stability. In order to quantify the effect to the system voltage stability by AC system parameters and VSC-HVDC link, a calculation method of the ESCR of the studied HMIDC system is derived based on the system equivalent circuit under the short-circuit situation, which offers a clear relationship of the system voltage stability and the system parameters including VSC-HVDC link. Through the ESCR, system voltage stability can be assessed quantitatively, as well as the contribution of VSC-HVDC to the system voltage.

Based on the analysis of the system ESCR, it is found that besides the capacity of the VSC-HVDC link, the phase angle of the VSC output current under short circuit situation is an important factor which affects the ESCR value, i.e. the system voltage stability. The flexible control characteristic of the VSC supplies the possibility of changing its current angle by the control strategies. Therefore, a power control method on the VSC-HVDC link to enhance system ESCR value is proposed. Two main parts are developed in the improved control scheme: the adaptive current limiter and the operation mode switch, which are designed for achieving the maximum use of reactive power support ability of the VSC-HVDC link and for riding through the send end disturbances of the VSC-HVDC, respectively. Simulation studies under different cases are investigated to verify the effectiveness of the proposed control strategy.

When considering the offshore wind farm which integrated into the system through VSC-HVDC link, the system voltage stability is also highly dependent on the fault ride through ability of the wind farm. A cooperative control strategy for variable speed SCIG-based offshore wind farm connecting with VSC-HVDC system is proposed and presented to achieve LVRT of the wind farm. The fast

power regulation of each wind turbine is realized though the cooperative control on the VSC-HVDC link and back-to-back converters in the wind farm. Under the proposed control method, the extra energy of the wind farm is transferred to the wind turbine as the kinetic energy of the rotor during the onshore fault period, so as to achieve the ride through of the VSC-HVDC connected wind farm.

The influence to system stability from the wind farm is not only exits under the system fault situation, but also can be found during the steady state operation. And the influence under steady state is caused by the variable nature of the wind power. The fluctuation on wind speed results in the variation of wind power integrated into the system, which consequently affect the power quality and bring the bus voltages variations. To mitigate the effect from wind power fluctuation and keep system voltage constant, in this work, the system voltage sensitivity has been analyzed and on the basis of that a reactive power control method is proposed.

7.2 Thesis Contributions

The main research contents of this work are the stability analysis and control improvement of the HMIDC system. In the opinion of the author the most relevant contributions in this research topic are:

- A Hybrid Multi-Infeed HVDC system model is developed, including the different HVDC links, the AC system presented by interconnected synchronous generators and the comprehensive loads. The studied HMIDC system model is built based on the future Western Danish power system, it can be applied as an integrated model or the basic element of a larger HMIDC system.

- A methodology is given for assessing the voltage stability of the HMIDC system quantitatively through the system ESCR. The calculation of HMIDC system ESCR is derived, which offers a quantitatively way to present the contribution of VSC-HVDC to the HMIDC system voltage stability

- Improved power control method is developed to achieve the maximum use of the VSC-HVDC link for increasing the system ESCR, i.e. the system voltage stability. Considering

the disturbance which may occur at the sending end of VSC-HVDC link, the proposed control method is also designed to realize the ride through of sending end fault of the VSC-HVDC link.

- The integration of an offshore wind farm through the VSC-HVDC system is investigated, and in order to enhance the LVRT ability of the wind farm, a cooperative control approach is proposed on the VSC-HVDC and variable speed SCIG based wind farm. It is confirmed by the simulation that with the proposed control approach, the VSC-HVDC connected offshore wind farm achieves LVRT under the onshore grid fault.

- Application of the voltage sensitivity analysis in the wind farm connected HMIDC system is investigated. Based on the voltage sensitivity, an improved reactive power control method is applied on the VSC-HVDC link to mitigate the system voltage fluctuation caused by the wind power variation. The improved method can be adopted as a local scheme with approximated constant sensitivity factors, or implemented as a wide area control method with time-varying voltage sensitivity factors calculated through the system variables in every sample circle.

7.3 Future Work

After the research work of this project, based on the investigation and the knowledge acquired from the work, several future research directions can be noticed.

- In this project, only two HVDC links are considered and investigated, whereas in many actual power systems, more HVDC links can be applied connecting with the same AC grid. Therefore, the study on a more complex HMIDC system with three or more HVDC links is left for future research.

- Although the different control methods are proposed in the HMIDC system as well as connected offshore wind farm, the combination of those control schemes for achieving the optimum operation of the HMIDC system needs to be researched.

- The load types considered in the studied system are only the steady load and induction motors. More different load types can be applied during the stability analysis of the studied HMIDC system, for example, the constant power load.

- The study on LVRT of the offshore wind farm is based on the variable speed SCIG wind turbine in this work. With the fast development of wind generators, the PMSG based wind turbine has got more and more attention. Hence the research of HMIDC system with PMSG based wind farm is also left for future research.

- In the voltage sensitivity analysis of the HMIDC system, the power regulation of the generators is not addressed in the work. The active and reactive power control ability of the generators can also be applied to support the system voltage stability, so that the controllability can be increased and the voltage sensitivity based control method can be further improved as a wide area control scheme in the system.